REPUBLIQUE ALGERIENNE DEMOCRATIQUE ET POPULAIRE

MINISTERE DE L'ENSEIGNEMENT SUPERIEUR ET DE LA RECHERCHE SCIENTIFIQUE

Université 20 août 1955-Skikda

Faculté des Sciences

Département de Physique

Thèse de Doctorat LMD

Filière: Physique - Spécialité: Physique des Matériaux

Présentée par

M^{elle} Romeissa NETTOUR

Thème :

Elaboration, by spray pyrolysis, and characterization of ZnMO (M=Mn, Co, Fe) thin films

----------oOo----------

Elaboration, par spray pyrolyse, et caractérisation de couches minces ZnMO (M=Mn, Co, Fe)

Soutenue le : 11/12/2025 à 10h00

Devant le Jury composé de:

Mr. Kamel KHOUNFAIS	Prof.	Université de Skikda	Président
Mr. Abdenour KABIR	Prof.	Université de Skikda	Rapporteur
Mr. Ali HAFS	Prof.	Université d'El-Tarf	Examinateur
Mr. Hocine SEFARDJELLA	MC-A	Université de Skikda	Examinateur

Année Universitaire : 2025/2026

Abstract

Transition metals TM (Co, Fe, and Mn) doping induced changes in structural and optical properties of spray deposited ZnO thin films has been studied using X-ray diffraction (XRD), Raman spectroscopy, ATR-FTIR spectroscopy, UV-visible spectroscopy, and photoluminescence spectroscopy (PL) respectively.

As a function of TM molar ratio x, XRD patterns revealed a change of crystalline parameters depending on TM nature. For Co doping, Co_3O_4 and $Zn(OH)_2$ secondary phases appeared for x=0.10. for Mn doping, secondary phases such as MnO_2 and $ZnMnO_3$ appeared for x=0.06 while for Fe doping, no secondary phase was observed. These results were evidenced by Raman spectroscopy and ATR-FTIR spectroscopy. For the three doping elements, the band gap energy of ZnO varied, as a function of TM molar ratio x depending on TM nature. For Co doping, the band gap energy of ZnCoO decreased from 3.45 eV, for x=0.00, to reach a minimal value of 2.67 eV for x=0.08. For Fe doping, the band gap energy of ZnFeO decreased to reach a minimum of 3.21 eV for x=0.04. Beyond this molar ratio, the band gap energy stabilized around 3.27 eV. However, for Mn doping, the band gap energy of ZnMnO increased to reach a maximum of 3.55 eV for x=0.06.

The photoluminescence spectrum of ZnO presented two peaks: an ultraviolet emission peak around 375 nm and a near infrared emission peak around 754 nm. Photoluminescence properties of samples depend on the TM nature and the TM molar ratio x. For Fe doping, the intensity of these two peaks decreased as a function of Fe molar ratio. No other emission peaks were observed. For Co doping, the intensity of these two peaks decreased as a function of Co molar ratio, to completely disappear for x=0.10 leaving their place to a red emission peak attributed to Co based impurities. For Mn doping, the intensity of UV and NIR emission peaks decreased rapidly for x=0.02. for x=0.04 and x=0.06, these two emission peaks disappeared leaving their places for a violet, a blue, and a blue-green emissions attributed respectively to Mn ions, Zn_i et V_{Zn}.

Keywords

ZnO; Doping; Ttransition metals TM; Thin films; Spray pyrolysis; TM molar ratio; XRD; Raman spectroscopy; ATR-FTIR spectroscopy; UV-visible spectroscopy; Photoluminescence spectroscopy

Résumé

Les changements induits dans le ZnO, déposé par spray pyrolyse, par dopage par les métaux de transition MT (Co, Fe et Mn) sur les propriétés structurales et optiques on été étudiés en utilisant la diffraction des rayons X (DRX), la spectroscopie Raman, la spectroscopie RTA-IRTF, la spectroscopie UV-visible, et la spectroscopie de Photoluminescence (PL) respectivement. En fonction du rapport molaire x du MT, les diffractogrammes révélaient le changement des paramètres cristallins du ZnO dépendant sur la nature du MT. Pour le dopage au Co, les deux phases secondaires Co_3O_4 et $Zn(OH)_2$ apparaissent pour x=0.10. Pour le dopage au Mn, des phases secondaire comme MnO_2 et $ZnMnO_3$ sont apparues pour x=0.06 tandis que pour le dopage au Fe, aucune phase secondaire n'a été observée. Ces résultats ont été mis en évidence par la spectroscopie Raman et la spectroscopie RTA-IRTF. Pour les trois éléments de dopage, l'énergie de la band interdite du ZnO varie, en fonction du rapport molaire x du MT, dépendant sur la nature du MT. Pour le dopage au Co, l'énergie de la band interdite du ZnCoO diminue de 3.45 eV, pour x=0.00, jusqu'à atteindre sa valeur minimale de 2.67 eV pour x=0.08. Pour le dopage au fer, l'énergie de la bande interdite du ZnFeO diminue jusqu'à atteindre un minimum de 3.21 eV pour x=0.04. Au delà de ce rapport, l'énergie de la bande interdite se stabilise autour de 3.27 eV. Cependant, pour le dopage au Mn, l'énergie de la bande interdite du ZnMnO augmente jusqu'à atteindre un maximum de 3.55 pour x=0.06. Le spectre de photoluminescence du ZnO pure présente deux pics: un pic d'émission ultraviolette autour de 375 nm et un pic d'émission infrarouge autour de 754 nm. les propriétés de photoluminescence des échantillons dépendent sur la nature du MT et le rapport molaire du MT. Pour le dopage au Fe, l'intensité de ces deux pics d'émission diminue en fonction du rapport molaire du Fe. Aucun autre pic d'émission n'a été observé. Pour le dopage au Co, l'intensité de ces deux pics d'émission diminue, en fonction du rapport molaire du Co, jusqu'à disparaitre complètement, pour x=0.10, laissant la place à un pic d'émission rouge attribué aux impuretés basées sur le Co. Pour le dopage au Mn, l'intensité des pics d'émission UV et NIR diminue rapidement pour x=0.02. Pour x=0.04 et x=0.06, les deux pics d'émission dispersaient laissant la place aux pics d'émission violette, bleu et bleu-verte attribuées respectivement aux ions Mn, Zn_i et V_{Zn}.

Mots clés

ZnO; Dopage; Métaux de transition MT; Couches minces; Spray pyrolyse; Rapport molaire du MT; DRX; Spectroscopie Raman; Spectroscopie ATR-IRTF; Spectroscopie UV-visible; Spectroscopie de photoluminescence

Content

Content

Chapter II

Deposition conditions and characterization techniques

Content

Content

List of figures

Chapter I

List of figures

Chapter II

Chapter III

List of figures

List of Tables

Chapter I

Chapter II

Chapter III

Introduction

The field of materials science is becoming increasingly essential in the development of new materials suitable for various applications in the technological and industrial sectors. The main challenge is to enhance the performance of these materials while minimizing their manufacturing costs. Zinc oxide (ZnO) continues to garner an extensive research interest owing to several of its promising applications. It has been the object of the renewed research for a wide range of applications such as light emitting diodes [1], laser diodes, gas sensor [2], thin film solar cells [3] and spintronics [4]. The interest of ZnO resides especially in its wide direct band gap (3.4 eV), high n-type conduc tivity, high thermal conductivity and its large exciton binding (60 meV) [5]. Nevertheless, during the design, the control of structural defects as well as sur face and interfacial structures is essential for optimizing the device performance [6]. In addition, it is noted that the growth conditions affect the band gap which is a key parameter in the design of optoelectronic devices.

In order to improve its interesting properties, ZnO has been successfully doped with metals such as Al, for use as a transparent electrode in solar cells, with rare earth such as Er, for use in light emitting diodes, and with transition metals such as Co, for a use as a diluted magnetic semiconductor (DMS) also termed diluted magnetic oxide (DMO). A theoretical study predicted that ferromagnetism was stable for wide band gap semiconductors such as ZnO and the Curie temperature can be increased for p-type DMS. Another theoretical study demonstrated that doping ZnO with Ni, Fe, Co, Cr, and V exhibited ferromagnetism ordering while doping it with Ti and Cu exhibited paramagnetic state. In order to enhance its spintronic properties the ZnO is doped with transition metals (Fe, Co, Mn). Synthesis of ZnO thin films has been performed by several techniques, such as spray pyrolysis, sol-gel [7], pulsed laser deposition [8] RF magnetron sputtering [9] and Chemical Vapour Deposition [10]. The spray pyrolysis technique has been selected owing to its large deposition area, low cost process, and viable approach of producing good quality films. Thus, many works have been carried out and

various parameters of the deposition of ZnO films such as, substrate temperature, carrier gas flow rate, solution flow rate, nozzle to substrate distance and film thickness have been optimized.

Depending on the type and concentration of transition metal (TM) the structural, optical, and magnetic properties of materials are found to be greatly affected from the exchange interaction between s and p electrons of host ZnO and d electron of TM ions. Among different TM elements, Mn, Fe and Co get much interest due to their different electronic shell structure and similar ionic size with Zn. Hence, they could be considered as good candidates to modify the structural, optical, physical and chemical properties of ZnO [11]. The restricted, unpaired d-electrons hybridize with the host ZnO's wandering sp-electrons to generate magnetically coupled electrons that participate in exchange interactions, resulting in SDOS between the host charge transporters. Commonly referred to as solid solutions of TM doped semiconductors to be DMS materials sincen-type semiconductors also exhibit magnetic ordering. DMS oxides are useful in numerous optoelectronic devices, including as diodes with optical spin, spin driven random access memory, spin field effect transistors, and light emitting devices (LED), thanks to their functional properties. DMS oxides also have greater magnetic moments and high curie temperatures, which are essential characteristics for the perfect spintronics material [12]

This thesis is divided into three main chapters organized as follows:

- The first chapter will presents general concepts on thin films, the different deposition techniques and deals with the properties and their applications of zinc oxide (ZnO). Previous studies of the main dopants used in this work are also presented.
- In the second chapter, the method used in the present work for the preparation of films is introduced as well as the experimental characterization techniques

used. Thin films have been studied by X-ray diffraction (XRD), UV-Visible spectrophotometry, Raman spectroscopy, ATR-FTIR spectroscopy and PL spectroscopy.

- The last chapter is dedicated to the thorough analysis and interpretation of the experimental results, elucidating the profound impact of Co, Fe, and Mn doping on the structural and optical properties of ZnO thin films. This section meticulously correlates the data obtained from XRD, Raman spectroscopy, UV-Vis spectroscopy, FTIR-ATR spectroscopy, and PL spectroscopy. The analysis reveals how the incorporation of these transition metal dopants disturbs the crystal lattice and chemical bonding, which in turn directly governs the optical behavior. The main results highlight significant modifications in the band gap energy, transmittance, and luminescence characteristics.

References

[1] T. Aoki, Y. Hatanaka and DC. Look, Applied Physics Letters 76 (2000) 22.

[2] O. Lupan and al, Materials Research Bulletin 45 (2010) 1026.

[3] Q. Zhang, CS. Dandeneau, X. Zhou and G.Cao, Advanced materials 21 (2009) 4087.

[4] DP. Norton, YW. Heo, MP. Ivill, K. Ip, SJ. Pearton, MF. Chisholm, Journal home page for Materials 7 (2004) 34.

[5] A Janotti, CG Van de Walle. Reports on progress in physics 72 (2009) 126501.

[6] C. Cao and Q. An, Quim. Nova 39 (2016) 261.

[7] R. Ebrahimifard, MR. Golobostanfard and H. Abdizadeh, Applied Surface Science 290 (2014) 252.

[8] QA. Drmosh, SG. Rao, ZH. Yamani and MA. Gondal, Applied Surface Science 270 (2013) 104.

[9] TY. Ma et al. Applied Surface Science 286 (2013) 131.

[10] X Li et al. Journal of Crystal Growth 287 (2006) 94.

[11] A. Goktas, F. Aslan, A. Tumbul and SH. Gunduz, Ceramics International 43 (2017) 704.

[12] L. Ali, WH. Shah, A. Ali, SM. Eldin, AA. Al-Jaafary, A. Sedky, J. Mazher, N. Imran and M. Sohail, Frontiers in Materials (2023) https://doi.org/10.3389/fmats.2023.1112798.

Chapter I

ZnO thin films : Properties, elaboration techniques and applications

I.1. Thin films

Thin films are film layers with thicknesses ranging from nanometers to a few micrometers that are deposited on substrates (Figure I.1) [1]. These films are engineered to exhibit unique properties tailored for specific application. The design process involves precise control over composition, structure, and thickness to achieve desired electrical, optical, magnetic, or mechanical properties.

Applications of advanced thin films span multiple industries, including electronics, energy, healthcare, and optics. In electronics, they are crucial for the development of semiconductor devices, transistors, and flexible displays. In the energy sector, thin films enhance the efficiency of solar cells and battery technologies. Healthcare benefits from thin films in medical devices and diagnostic tools, while optics relies on them for anti-reflective coatings and optical filters. The ongoing advancements in thin film technology promise to drive further innovations, making them indispensable in the quest for miniaturized, high-performance, and energy-efficient devices across various fields [2].

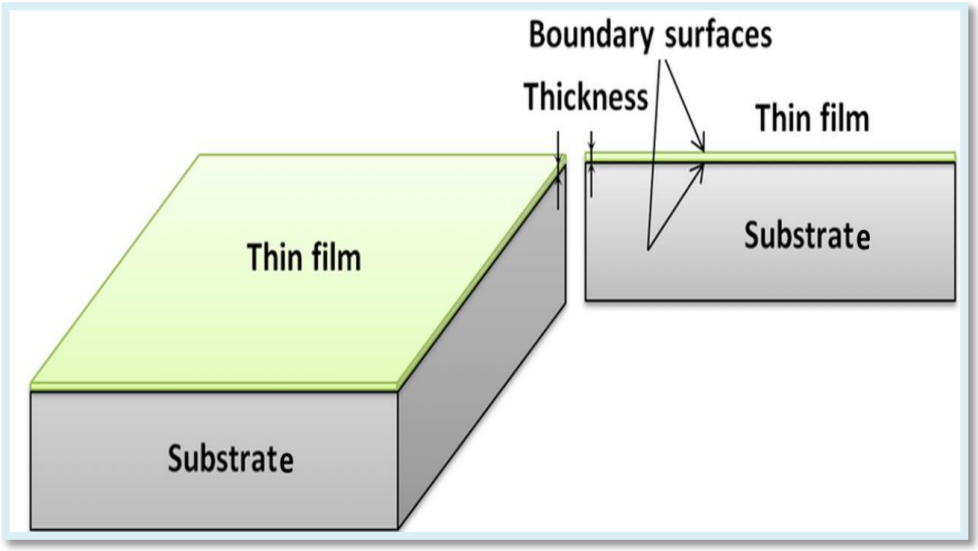

Figure I.1. Schematic of a thin film deposited on a glass substrate [3].

I.1.1. Mechanism of a thin film formation

During the nucleation and growth stage of the film, there is a transition from the plasma (plume) phase to a crystalline (solid) phase on the substrate surface [4].

I.1.1.1. Nucleation

The incident atoms are deposited on the surface of the substrate. These atoms being thermodynamically unstable on the surface, some will be re-evaporated, others ejected by back-sputtering**.** On the other hand those which bind weakly by transferring their kinetic energies to the substrate lattice**.** These will be diffused and trapped by other incident atoms adsorbed to form clusters also called nuclei (Figure I.2). Then, these clusters combine with other clusters to create islands. These islands will grow and coalesce to extend over the entire surface of the substrate [5].

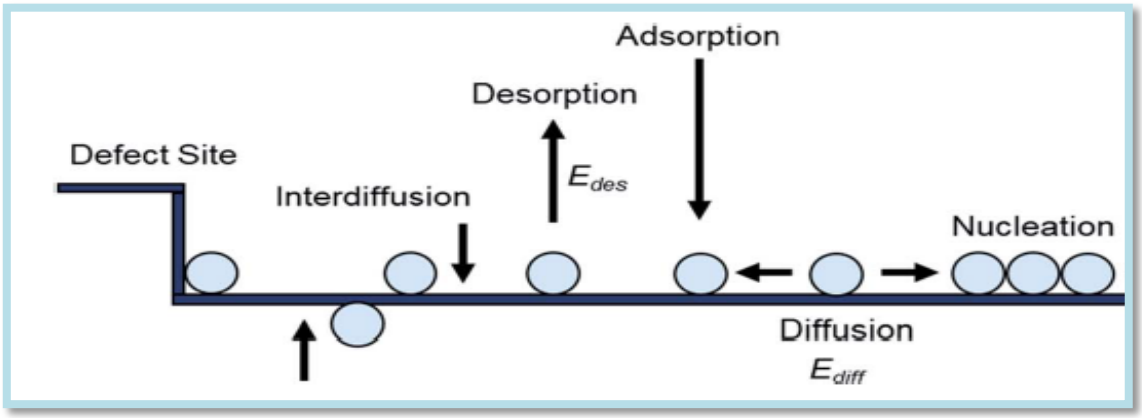

Figure I.2. Schematic of the nucleation and growth process on a substrate [6].

I.1.1.2. Growth of thin films

The study of growth mechanisms is critical for controlling material properties at the atomic level, optimizing fabrication processes, and reducing defects in advanced II-VI semiconductors [7]. Generally, there are three modes of thin film growth, namely island or the

Volmer–Weber mode, layer-by-layer or the Frank–van der Merwe mode and layer plus island or the Stranski–Krastanov mode [4].

a) Volmer–Weber mode (or Island)

An island growth occurs when the cohesion between the atoms of the target material is greater than the adhesion between the target atoms and the substrate. As a result, the adatoms (atoms deposited on the surface of the substrate) are more bound to each other than to the substrate, hence forming clusters. This mode of growth is characterized by three-dimensional (3D) islands (Figure I.3).

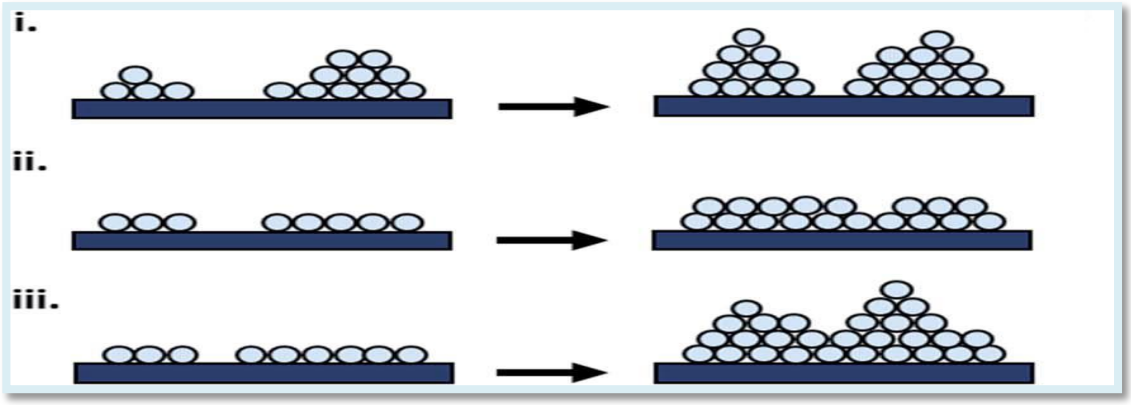

Figure I.3. Schematic of the different thin film growth mechanisms: (i) island, (ii) layer-by-layer, (iii) layer plus island [6].

b) Frank–van der Merwe mode (or Layer-by-layer)

Layer-by-layer growth occurs when the adhesion between the adatoms and the substrate is greater than the cohesion between the adatoms. This mode of growth generally results in 2D growth with the adatoms forming smooth monolayers on the surface of the substrate (Figure I.3).

c) Stranski–Krastanov mode (or Layer plus island)

Layer plus the island growth mode occurs when islands are formed after the formation of one or two monolayers on the surface of the substrate (Figure I.3).

I.1.2. Thin films depositions methods

Thin film deposition methods are classified commonly in two categories. The first one is physical deposition methods, and the second one is chemical deposition methods. It can be summarized as shown in figure I.4.

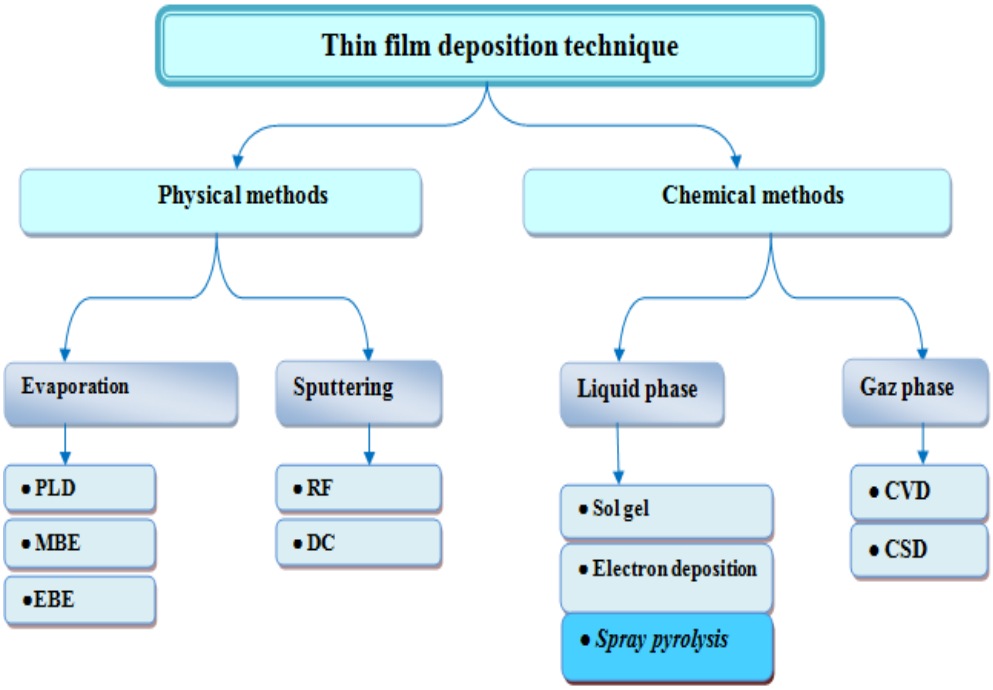

Figure I.4. Summary of thin films deposition techniques.

I.1.2.1. Physical deposition methods

Physical deposition methods are usually referred as to physical vapor deposition methods (PVD) because the process entails the generation of vapor. PVD essentially consists

in removing growth species from a source or target material via evaporation, then this vapor is transported to the substrate surface, and eventually it solidifies in the surface, forming the film. The evaporation is generally carried out under a reduced pressure chamber to avoid impurities in the film formation which are produced due to collisions between vapor particles and residual gas particles in their displacement from the source to the substrate surface. PVD techniques are known to offer a number of advantages, including the deposition of almost any material, high reproducibility of film properties, the use of a large range of substrate materials, the possibility of tailoring the film properties through modification of deposition parameters in single element deposition, and obtaining films with high purity. On the other side, among the main disadvantages are the use of sophisticated and costly monitoring systems for the control of the deposition rate and film thickness, and the mismatch between the composition of the deposited film and the composition of the evaporant in the case of alloys and compounds. The most common PVD processes are vacuum evaporation, molecular beam epitaxy, pilsed laser deposition, and sputttering [8].

I.1.2.1.1. Vacuum evaporation

Vacuum evaporation is a method for depositing thin films of metals, alloys, or compounds by vaporizing solid materials and then depositing them onto specific substrate in a vacuum environment. The substrate temperature varies from room temperature to elevated temperature.

This technique is categorized into two groups based on the heating source: resistive heating and electronic-beam heating. In resistive heating, the source material is placed in a crucible and heated by a filament (Figure I.5). This method is particularly effective for materials with melting points below 1500°C.

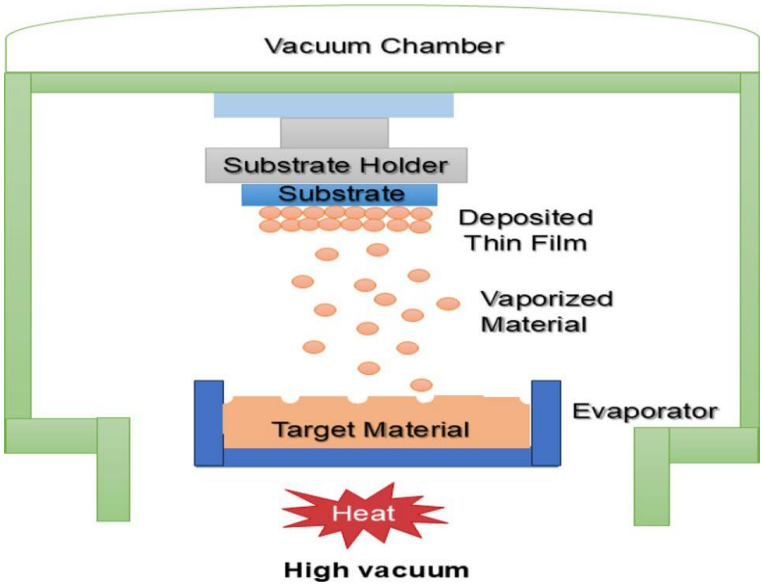

Figure I.5. Schematic of the thermal evaporation method [10].

On the other hand, e-beam evaporation is suitable for high-melting-point materials, such as refractory metals. In this process, electrons are accelerated at high voltage and directed toward the target material, where they bombard the surface, generating heat and causing the source material to evaporate (Figure I.6). Thin films prepared by electron beam evaporation are of good quality and purity. However, resistive heating or Joule heating remains the most used process for the target evaporation [9].

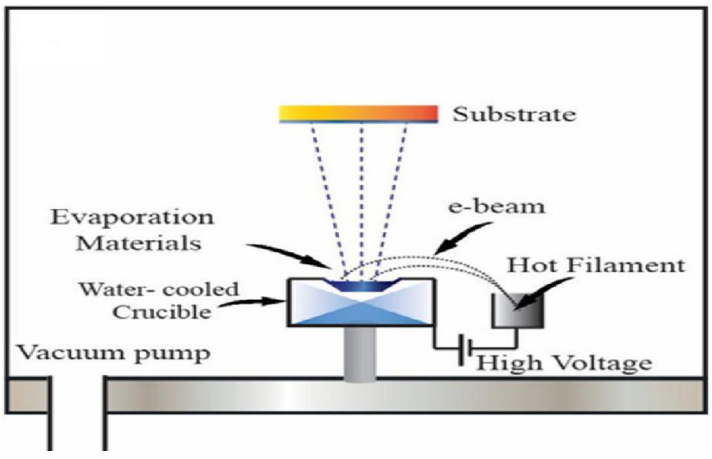

Figure I.6. Schematic of electron beam evaporator [9].

I.1.2.1.2. Molecular Beam Epitaxy

The Molecular beam epitaxy (MBE) is an ultrahigh vacuum technique for growing skinny epitaxial layers of semiconductor crystals. Because it is inherently a slow growth process, extreme dimensional control over both major compositional variations and impurity incorporation can be achieved. The basic principle is to spray atoms or molecules of material onto the target substrate with appropriate reaction temperature and lattice orientation in an ultra-high vacuum environment [11]. Atoms or molecules react on the substrate surface, forming high-quality thin crystal film as shown in Figure I.7.

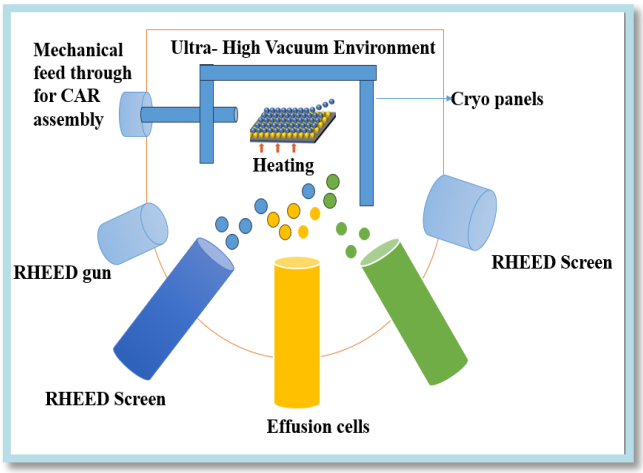

Figure I.7. The sketch map of molecular beam epitaxy technique [9].

I.1.2.1.3. Pulsed Laser Deposition

The Pulsed Laser Deposition technique (PLD) has been extensively studied and optimized for various material systems, demonstrating its versatility and potential in numerous applications. The entire process takes place within a carefully controlled vacuum chamber to ensure the necessary conditions for successful deposition, shown in figure I.8. The process of PLD can be divided into four distinct steps. In the first step, the laser beam is absorbed by the target material, resulting in vaporization and ablation. In the second step, a plasma is formed

consisting of neutral atoms, molecules, ions, and energetic electrons in the presence of a low-pressure oxygen atmosphere. In the third step, the plasma containing the material that has been removed from the target moves toward the substrate. In the fourth step, complex reactions take place between the plasma and the substrate, resulting in the deposition of the separated material onto the surface of the substrate [9].

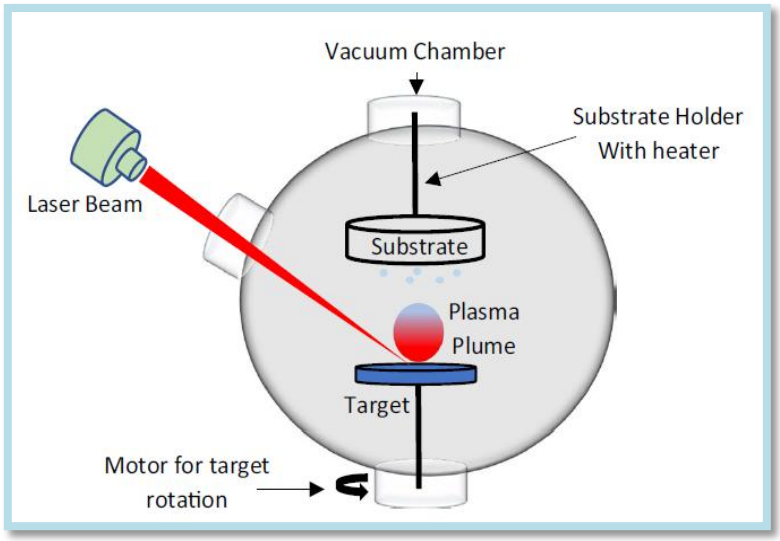

Figure I.8. Schematic of the PLD process [12].

I.1.2.1.4. Sputtering

Sputtering is one of the PVD techniques that involve depositing thin film coatings by bombarding a target material's surface atoms with accelerated ions. The target material to be deposited is placed on the cathode, and the substrate is positioned at the anode (Figure I.9). The working gas inside the deposition chamber is usually argon gas. There are two types of the sputtering. We can cite direct current sputtering (DC) and radio frequency sputtering (RF). Each type is used for thin film deposition with specific characteristics. DC is utilized for depositing metallic materials, while a RF sputtering technique is employed for insulating

target materials. For DC sputtering, a DC voltage is supplied between the cathode (target material) and anode (substrate) to sustain the glow discharge. The gaseous ions resulting from the sustained glow discharges are accelerated towards the target material, and sputtering takes place resulting in deposition of a thin film on the surface of the substrate material [13]. For RF sputtering, the cathode is bombarded by applying a high voltage at a fixed frequency of 13.56 MHz in the vacuum chamber, which leads to high-energy ions that sputter atoms to become a thin film that coats the substrate [14]. For high quality thin films, the DC and RF sputtering techniques are equipped with a magnet that confines the plasma close to the substrates.

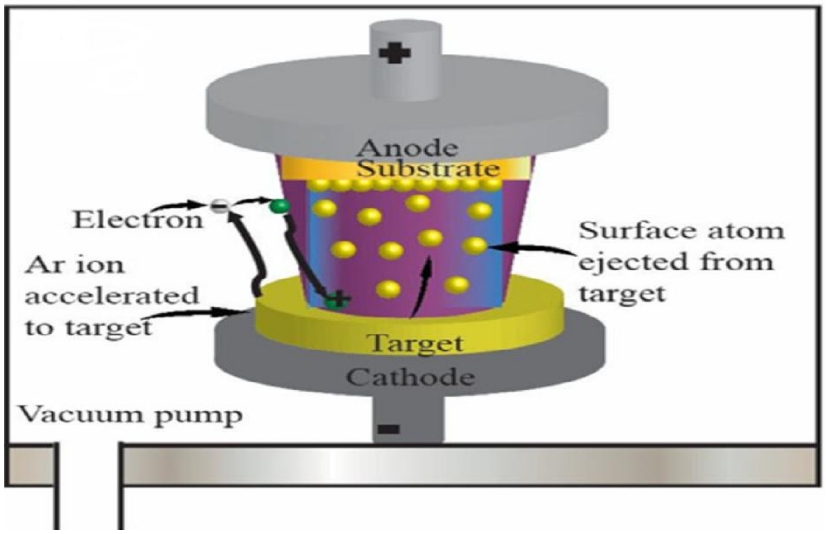

Figure I.9. Schematics of the sputtering method [9].

I.1.2.2. Chemical deposition methods

The chemical methods comprise gas phase and liquid phase deposition methods such as chemical vapor deposition (CVD), chemical bath deposition (CBD), spray pyrolysis, and sol-gel.

I.1.2.2.1. Chemical Vapor Deposition

Chemical Vapor Deposition (CVD) is a widely used technique for depositing thin films through a series of chemical reactions. Unlike Physical Vapor Deposition (PVD), where thin films form via condensation of evaporated atoms or sputtered particles, CVD relies on complex chemical reactions occurring near or on the substrate surface under controlled conditions of temperature, pressure, and reactant flow (Figure I. 10). The quality of CVD films is influenced by process parameters such as temperature, pressure, chemical concentration, gas flow rates, and reactor design [15].

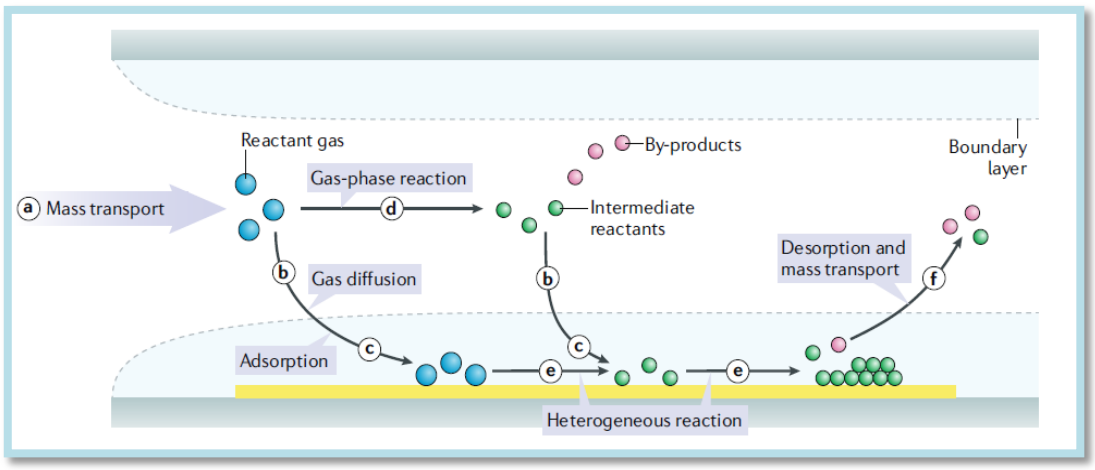

Figure I.10. Schematic of general elementary steps of a typical CVD process [16].

Chemical vapor deposition has numerous other names and adjectives associated with it such as vapor phase epitaxy (VPE) when CVD is used to deposit single crystal films, metalorganic CVD (MOCVD) when the precursor gas is a metalorganic species, plasma-enhanced CVD (PECVD) when a plasma is used to induce or enhance decomposition and reaction, and low pressure CVD (LPCVD) when the pressure is less than ambient [17].

I.1.2.2.2. Chemical Bath Deposition

Chemical Bath Deposition (CBD) is a well established and low temperature chemical method widely used for thin film deposition. The semiconducting thin films synthesized by CBD method have potential to compete with film by other sophisticated techniques. The CBD consists on the precipitation of the material atoms onto the substrate emrsed in a solution containing the material soluble salts (Figure I.11). CBD is found to be beneficial for deposition of ternary and quaternary compound. It provides better orientation of crystallites due to higher reaction time. Various factors affecting CBD such as bath temperature, pH of solution, complexing agent, concentration of cation and anion, deposition time and aging of the stock solution [18].

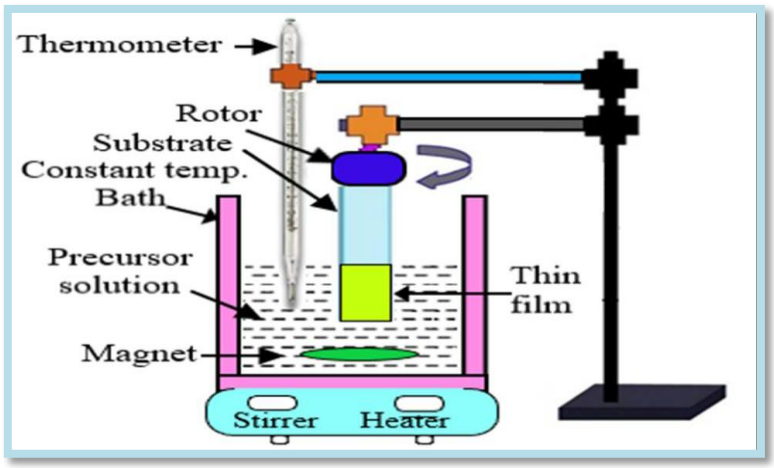

Figure I.11. Schematic of the CBD method [19].

I.1.2.2.3. Sol gel

The sol gel process is a wet chemistry technique in which a solution, or “sol”, undergoes a transition to form a rigid “gel”. It is one of the chemical methods used for the deposition of thin films of transparent and conductive oxides. This method offers inherent advantages, including high product purity and chemical homogeneity, while enabling low-temperature

processing compared to other techniques [20, 21]. The sol gel technique involves two methods for thin films deposition: the spin coating and the dip coating. In the spin coating process, the solution is spread by centrifugation onto a substrate that rotates at speeds of several thousand rounds per minute (Figure I. 12). In the dip coating process, thin films are often produced by dipping and withdrawing a substrate into a beaker as illustrated in figure I.13. The film forms as the solvent evaporates after the substrate is removed. Factors such as the withdrawal speed, the dispersion concentration, the viscosity, and the solvent's boiling point are critical in achieving a uniform coating [23].

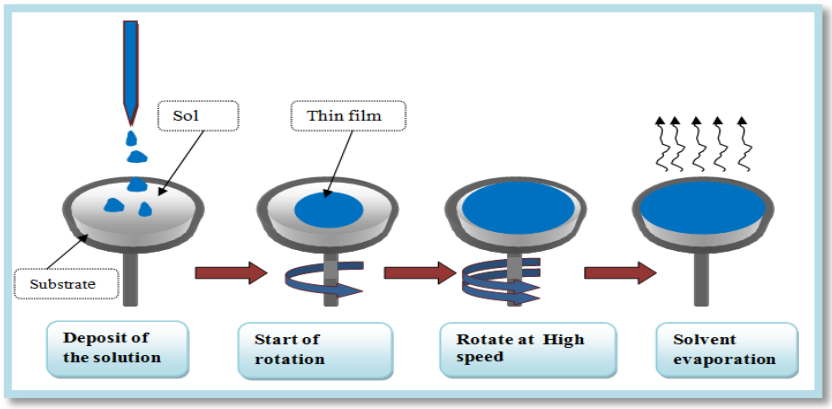

Figure I.12. Deposition of thin layers by spin coating [24].

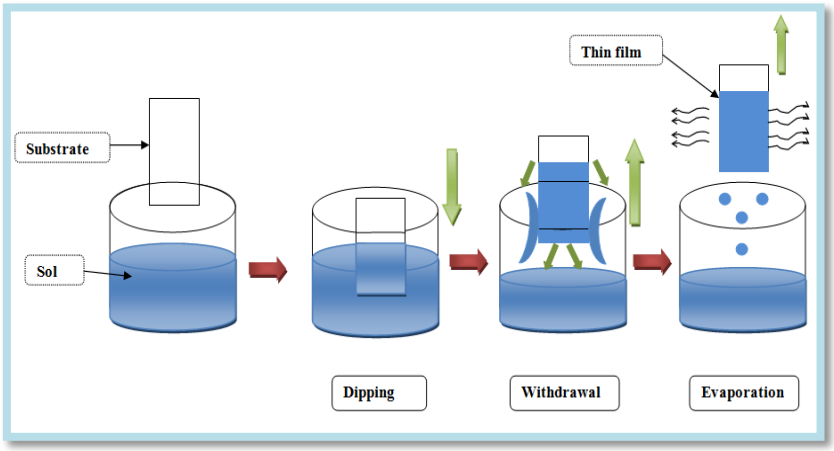

Figure I.13. Schematic representation of the principle of deposition by dip coating [24].

I.1.2.2.4. Spray pyrolysis

The spray pyrolysis technique has lately attracted increasing attention due to some appealing features such as their low production cost, flexibility in the substrate choice, possibility of large area of deployment. This technique was initially proposed by Chamberlin and Skarman [25] in 1966 to prepare CdS thin films on glass substrates. It consistes on the spraying of an aqueous solution containing soluble salts of the constituent atoms of the desired compounds to heated substrates. The liquid droplets vaporize before reaching the substrate or react on it after splashing (Figure I.14). Doped and mixed films can be prepared very easily, simply by adding to the spray solution a soluble salt of the desired dopants or impurity [19].

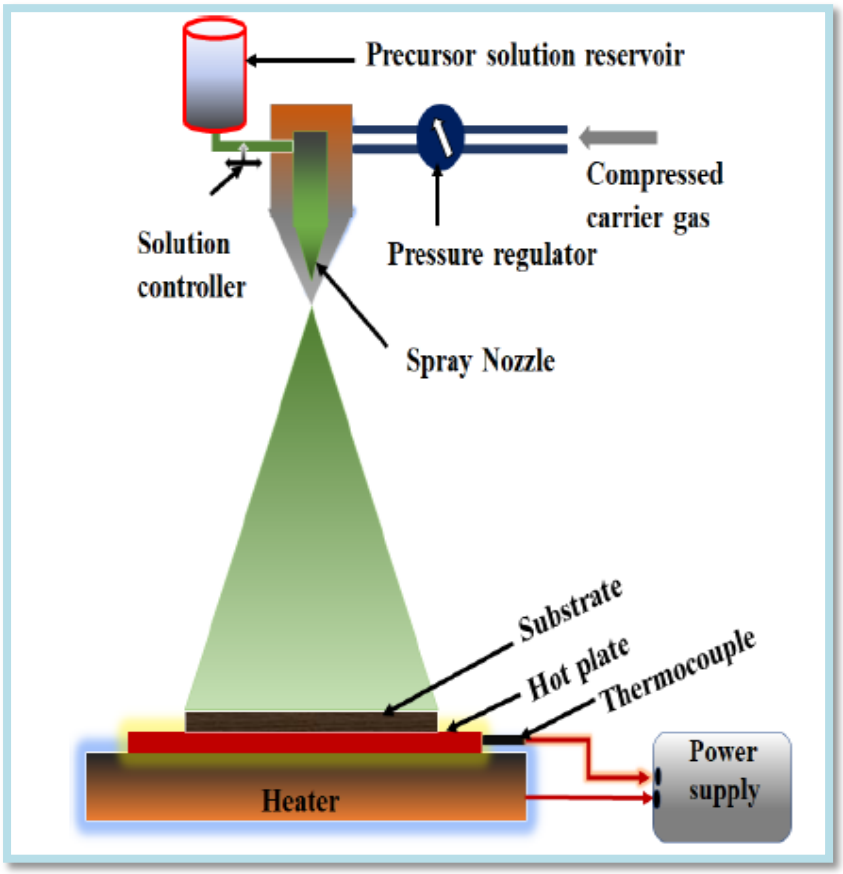

Figure I.14. The schematics of the experimental set up for spray pyrolysis [26].

The process is particularly useful for the deposition of metal oxides, nanocomposites and perovskite thin films. Spray pyrolysis System has been designed for research in laboratories in thin films, especially for solar cell and gas sensor development [27].

In the spray pyrolysis method, thin film formation is based on a thermally stimulated chemical reaction between clusters of liquid or vapor atoms of different chemical species. In this process, the precursor solution is atomized through a nozzle (Figure I.14). The nozzle converts the solution into small droplets, known as aerosols. These aerosols are allowed to incident onto preheated substrates. The pyrolysis decomposition of the aerosols and formation of thin films with desired properties depends on the optimum substrate temperature. The properties of the film depend upon the anion to cation ratio, spray rate, substrate temperature, ambient atmosphere, carrier gas, droplet size and also the cooling rate after deposition. The film thickness depends upon the distance between the spray nozzle and substrate, the substrate temperature, the concentration of the precursor solution and the quantity of the sprayed precursor solution. The film formation depends on the process of droplet landing, reaction and solvent evaporation, which are related to droplet size and momentum. An ideal deposition condition is when the droplet approaches the substrate just as the solvent is completely removed. Lampkin [28] showed that, depending on droplet velocity and flow direction, a droplet will flatten, skip along the surface or hover motionless.

Apart its simplicity, the advantages of the spray paralysis technique are [29]:

- A low cost technique for the preparation of semiconductor thin films.
- Extremely easy way to dope films with any elements in proportion by adding it to the spray solution.
- Production of large area, high quality adherent films of uniform thickness.
- No require to the high quality targets nor require vacuum at any stage which is great advantage if the technique is to be scaled up for industrial applications.

- Easy control of the deposition rate and thickness of the films over a wide range by changing spray parameters

I.1.3. Application of thin films

Thin films have an important impact on technologic development in many fields such as the energy field, the electronic field, the health field and the environmental field. Actually, the need of materials with adjestable properties is crucial to be used in industrial scale. Among these materials with specific properties we focus on transparent and conductive oxides (TOCs). These materials are very useful for transparent optoelectronics [30] because they have unique features of optical properties in the visible light region such as the transparency over ~ 85%, the optical band gap greater than 3 eV, and the controllable electrical conductivity (carrier concentrations of at least 10^{20} cm^{-3} and resistivity of about $10^{-4}\Omega.cm$). Due to their extraordinarily wide controllable conductivity range including that of semiconductors, TCO thin films have a wide range of applications including transparent heaters, heat mirrors, smart windows, and optoelectronic devices in particular the market for transparent electrodes used in touch panels, flat panel display or lamps, and thin film solar cells which is still expending linked to the increase of new emerging solar cells technologies and devices as organic and perovskite ones [30].

The most widely studied TCO semiconductors are impurity-doped ZnO, In_2O_3, SnO_2 and CdO, as well as the ternary compounds Zn_2SnO_4, $ZnSnO_3$, $Zn_2In_2O_5$, $Zn_3In_2O_6$, $In2SnO_4$, $CdSnO_3$, and multi-component oxides consisting of combinations of ZnO, In_2O_3 and SnO_2 [31]. These three oxides were repectively doped with Al, Sn, and Sb and the result was three

known semiconductors AZO, ITO, and ATO of improved electrical conductivity without degrading their optical transmission [32].

Among many TCO materials, and with the huge increase of research in numerization and artificial intelligence (AI), transition metals-doped ZnO has taken its place as one of the most important candidates for next-generation electronic devices due to its high earth abundance, nontoxicity, biocompatibility, and affordability [33].

I.2. Zinc oxide

Zinc oxide is an inorganic compound with of formula ZnO. It commonly appears as a white powder, almost insoluble in water. ZnO is present in the earth crust as a mineral zincite however, most ZnO used commercially is produced synthetically (Figure I.15). The basic physico-chemical properties of Zinc Oxide are tabulated in Table I.1. ZnO has attracted the attention of researchers because of its attractive properties and many applications [34]. In 1960, zinc oxides were discovered to have solid piezoelectric properties, and zinc oxides were first applied as thin electron layers to surface acoustic wave devices [35].

Figure I.15. ZnO presented in natural form (a) and (b) and synthesis powder form (c) [35].

After extensive research in 50s and 70s, studies of zinc oxides as semiconductor materials resurfaced [35]. Since 1990, the number of ZnO periodicals has increased dramatically, and current ZnO reviews have been published in materials science journals [35] for use in devices utilizing nanowires/nanorods such as biosensors, gas sensors and solar cells [36].

.

Table I.1: Physico-chemical properties of ZnO at room temperature [20].

Molecular formula	**ZnO**
Appearance	White solid
Solubility in water (at 30°C)	0.16 mg/100 mL
Molecular mass (g/mol)	81.408
Density g/cm^3	5.606
Melting point (°C)	1975
Refractive index	2.0041
Direct energy band gap (eV)	3.3
Hole mobility ($cm^2V^{-1}s^{-1}$)	200
Electron effective mass (m_0)	0.24
Hole effective mass (m_0)	0.59

I.2.1. Structural properties

According to theoretical and experimental works conducted on its crystallization modes, ZnO can be present in three phases [38] schematized in figure I.16:

- **The "Wurtzite" phase (hexagonal structure):** It is the most widespread phase in nature, observed during deposition under normal pressure and temperature conditions.
- **The "Zinc Blende" phase (cubic structure):** This phase is observed during deposition on substrates with cubic symmetry.
- **The "Rocksalt" phase (NaCl cubic structure):** This metastable structure is obtained under high pressure (around 10 to 15 GPa) applied to the hexagonal wurtzite phase and can persist at atmospheric pressure.

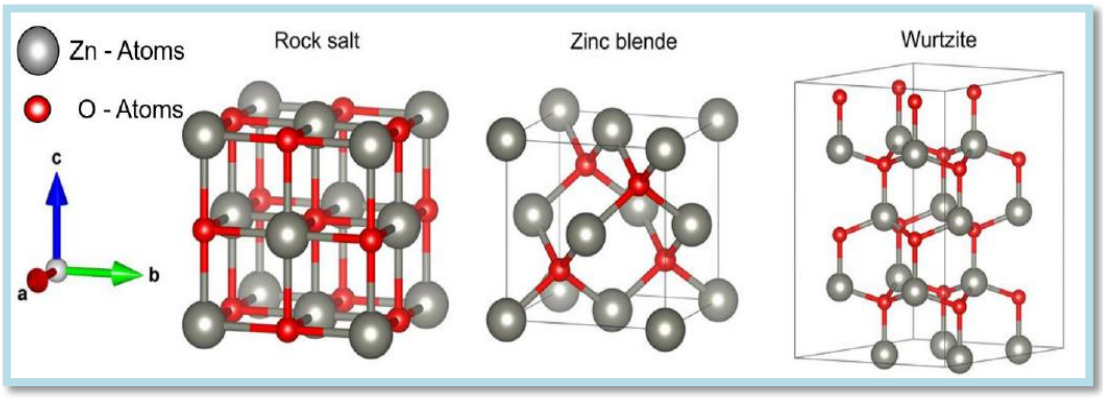

Figure I.16. Crystallization modes of ZnO [38].

A cesium chloride (CsCl) cubic structure was predicted by theoretical calculations at extremely high temperatures; this phase has not yet been experimentally observed [29]. The phase diagram (Figure I.17) estabilished by Decremps et al. [39] revealed that zinc oxide can transit from the wurtzite phase to the rocksalt phase under the effect of pressure and temperature. We focuse on the wurtzite structure since it is the most stable form of ZnO.

In the wurtzite structure, ZnO has a hexagonal unit cell with lattice parameters a=b= 3.296 Å and c=5.206 Å [40]. In this structure, the oxygen anions and zinc cations form a tetrahedral unit and the entire structure lacks central symmetry, so it is composed of two

elements with different ion radii [20]. ZnO can be directly defined as a chain of alternating planes created by tetrahedrally coordinated O^{2-} and Zn^{2+}, where each O (or Zn) atom is surrounded by four Zn (or O) atoms alternately stacked along the c-axis (Figure I.18).

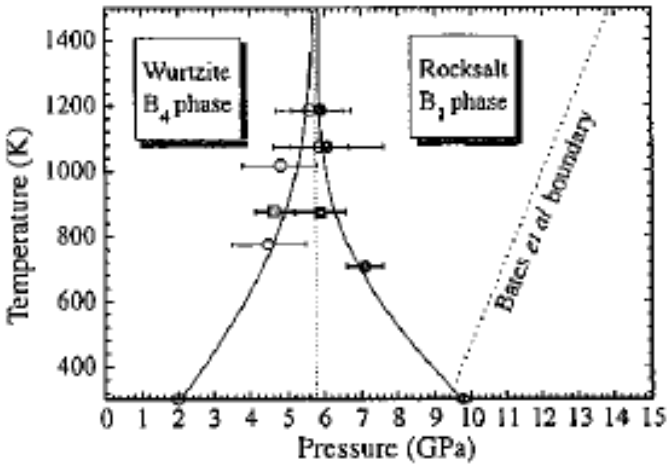

Figure I.17: Phase diagram of ZnO [39].

The polar surface of ZnO is another important property**.** It has a polar (0001) surface terminated with either Zn or O. The Zn-type polarity is represented by the + c (0001) direction. Type O polarity is associated with direction -c (000 -1) [40].

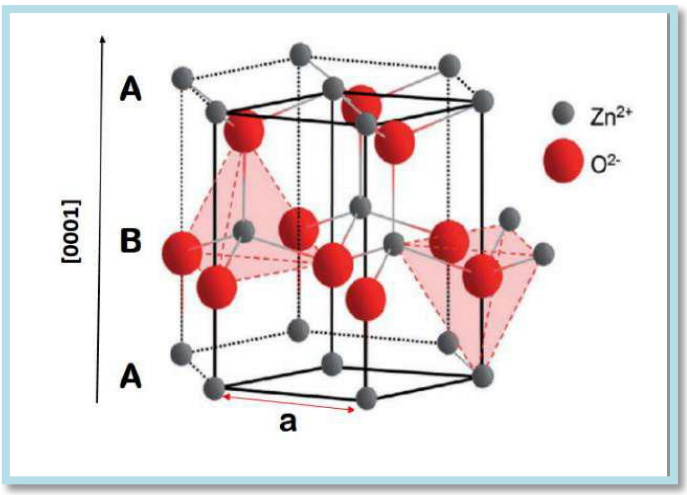

Figure I.18: ZnO wurtzite structure [41].

The hexagonal lattice of the wurtzite ZnO is characterized by three lattice constants that determine the relative positions of the O anion and Zn cation sublattices are a (the side of a rhombus constituting the base), c (the side parallel to the oz axis) and u (the interior coordinate along the axis). The u coordinate is a dimensionless parameter and is defined by the following relationship [20]:

$$u = \frac{1}{4} + \frac{c^2}{3a^2} \quad \text{(I.2)}$$

The particular positions of the four atoms in the wurtzite structure in each cell are (0, 0, 0) and (1/3, 2/3, 1/2) for Zn and (0, 0, u) and (1/ 3, 2/3, u+1/2) for O [20]. The stability of this structure is determined using the following relationship [20]:

$$0.225 \leq \frac{R_a}{R_c} \leq 0.414 \quad \text{(I.4)}$$

where Ra and Rc are the radii of the anion and cation, respectively. The stacking in the wurtzite structure of ZnO is composed of two interpenetrating hc sublattices (Figure I.18), with alternate atomic planes stacking in the sequence ABAB along the [0001] direction [20].

I.2.2. Vibrational properties

Phonons result from the displacement of one or more atoms in the crystal lattice around their equilibrium position, generating series of vibrational waves that propagate through the lattice. These vibrations can be thought of as a collective excitation of the lattice, where the atoms or molecules oscillate in a coordinated manner. In solids, there are two types

of phonons: acoustic phonons, which correspond to sound waves in the crystal lattice, and optical phonons, which are easily excited by light waves in ionic crystals such as NaCl and ZnO. These optical phonons arise from a dipolar electric moment created by the approaching and distancing of positive and negative ions in adjacent lattice sites, producing longitudinal optical (LO) and transverse optical (TO) phonon (Figure I.19). In ZnO, there are four atoms in the primitive unit cell, resulting in twelve vibrational modes (phonons) [42]. These include three acoustic modes: one longitudinal (LA) and two transverse (TA). The remaining nine are optical modes: three longitudinal optical (LO) and six transverse optical (TO).

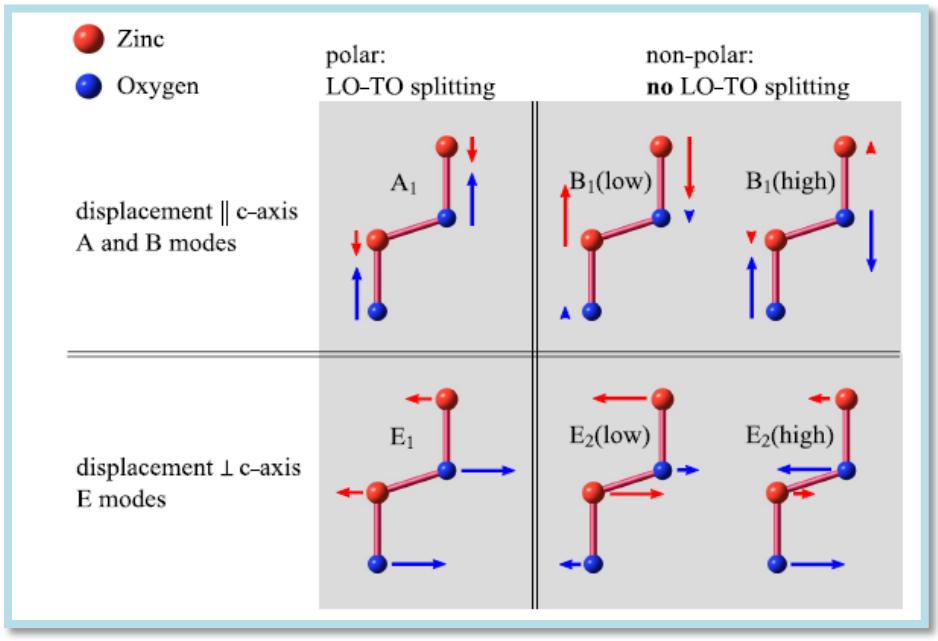

Figure 1.19: Vibrational modes of ZnO [42].

In the wurtzite ZnO case, the number of atoms per unit cell is *s*=4 and there are a total of 12 phonons modes, namely, one longitudinal-acoustic (LA), two transverse-acoustic (TA), three longitudinal-optical (LO), and six transverse-optical (TO) branches. Infrared reflection and Raman spectroscopies have been commonly employed to derive zone-center and some zone-boundary phonon modes in ZnO. Because the space group C_{6v} describes the crystalline

structure of the wurtzite ZnO compound with 2 f.u. in the primitive cell, the optical phonons at the Γ point of the Brillouin zone belong to the following irreducible representation of the lattice optical phonons:

$$\Gamma_{Opt} = 1A_1 + 2B_1 + 1E_1 + 2E_2 \quad \text{(I.5)}$$

A_1 and E_1 branches are both Raman and infrared active, the two nonpolar E_2 branches are Raman active only, and the B_1 branches are inactive (silent modes). The A_1 and E_1 modes are each split into LO and TO components with different frequencies due to the macroscopic electric fields associated with the LO phonons. Because the electrostatic forces dominate the anisotropy in the short-range forces, the TO-LO splitting is larger than the A_1-E_1 splitting. For the lattice vibrations with A_1 and E_1 symmetries, the atoms move parallel and perpendicular to the c axis, respectively. The low-frequency E_2 mode is associated with the vibration of the heavy Zn sublattice, while the high-frequency E_2 mode involves only the oxygen atoms. In the case of highly oriented ZnO films, if the incident light is exactly normal to the surface, only A_1 (5LO) and E_2 modes are observed, and the other modes are forbidden according to the Raman selection rules [43].

I.2.3. Optical properties

ZnO is a transparent material in the visible region, a consequence of its wide bandgap (Eg = 3.37 eV). It also exhibits strong absorption and scattering of ultraviolet (UV) radiation, with the fundamental absorption edge occurring at wavelengths below 360 nm. The refractive index of ZnO in thin film form ranges between 1.90 and 2.30, while for bulk ZnO, it is approximately 2.8. In general, both the refractive index and the absorption coefficient of ZnO vary depending on the fabrication conditions. Under the influence of a high-energy light beam (E > 3.37 eV) or electron bombardment, zinc oxide emits photons. This phenomenon

corresponds to luminescence. The visible luminescence arises from defects associated with deep-level emissions (virtual states between the conduction band and valence band), such as zinc interstitials, oxygen vacancies, and impurities introduced by doping. ZnO also exhibits a reflection region corresponding to reduced transmission for wavelengths $\lambda > 1500$ nm (Figure I.20). This transition, associated with a maximum absorption peak, is referred to the plasma wavelength (λ_p), where the light frequency matches the collective oscillation frequency of electrons in the material. When $\lambda < \lambda_p$, the wave function is oscillatory, allowing radiation to propagate and giving the material a transparent appearance. Conversely, when $\lambda > \lambda_p$, incident light is reflected by the material, imparting a metallic appearance. This phenomenon is described by the classical Drude free-electron theory. An example transmission, reflection, and absorption spectrum for a zinc oxide material is shown in figure I.20.

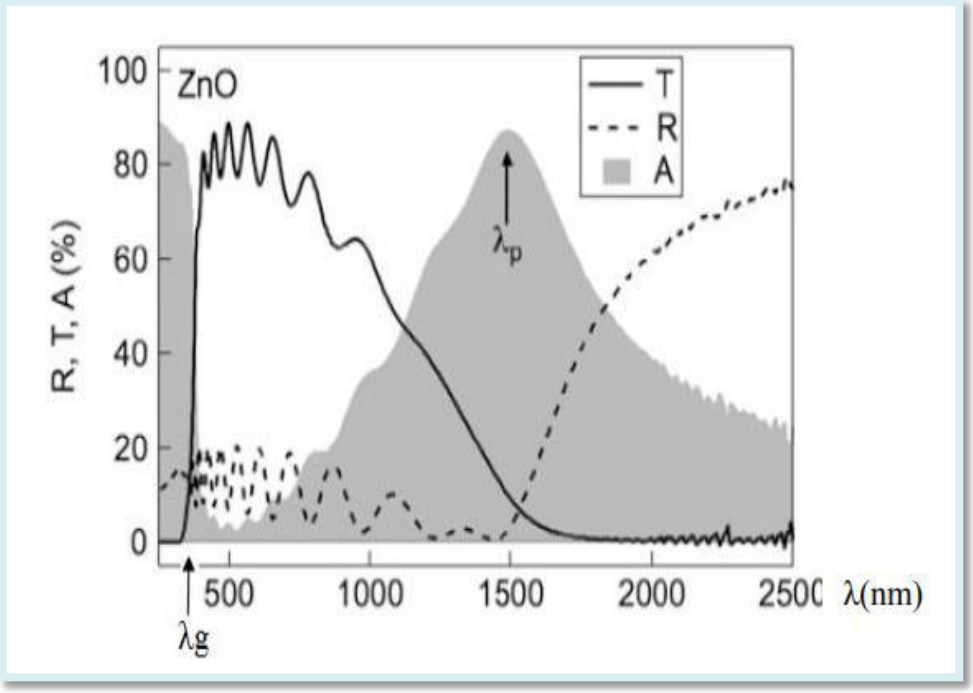

Figure I.20: Transmission, reflection, and absorption spectra for ZnO [44].

The optical properties of ZnO are already being exploited in the industry with applications in photo-catalysis and in UV solar filters. The discovery of multifunctional properties in ZnO boosted the existing interest in this material. For any potential material for optoelectronics, it is crucial to investigate the origin of luminescent centres which are due to intrinsic or extrinsic defects inside the semiconductor. The optical properties can be tailored and controlled by modifying the distribution of these defects inside the grains. The emission from these defects can be studied by photoluminescence spectroscopy. The most prominent emissions, i.e. near band emissions, are attributed to donor and acceptor energy levels where as; deep level defects are responsible for visible emissions [45].

I.2.4. Electrical properties

ZnO is an intrinsically n-type semiconductor due to the deviation from stoichiometry and the presence of intrinsic defects such as oxygen vacancies (V_O), zinc interstitials (Zn_i), and zinc vacancy (V_{Zn}). Doping of ZnO provides a method for controlling its structure, and consequently optical, electrical, and magnetic properties, which leads to a range of changes, including band gap value, transparency, room-temperature ferromagnetism, piezoelectricity and magneto-optical properties.

The n-type doping of ZnO with a donor state, achieved by replacing atoms with one or more electrons in the outer shell compared to the substituted element (Zn or O) in ZnO. Consequently, the substitution of group-III elements on Zn sites and group-VII elements on O sites, produces highly conductive n-type ZnO. These group VII elements, F, Cl, Br, and I are also donor dopants by substituting oxygen atoms. It has been reported that fluorine F doping can increase the conductivity of ZnO by chemical spray techniques [23]. The p-type doping of ZnO with an acceptor level is provided by substitution by group-I elements on Zn sites and group-V on O sites. Although, ZnO can be easily n-type doped, efforts to obtain reliable p-

type doping are still a problem due to the low solubility, much higher ionization and formation energy of p-type dopants [45].

I.2.5. Electronic properties

The electronic properties of ZnO have been the subject of several studies, including those of its band structure [46]. The electronic structures of oxygen and zinc are as follows:

O : $1S^2\ 2S^2\ 2P^4$

Zn : $1S^2\ 2S^2\ 2P^6\ 3S^2\ 3P^6\ 4S^2\ 3d^{10}$

The 2P states of oxygen form the valence band and the 4S states of zinc form the conduction band of the ZnO semiconductor. Therefore, to form an ionic bond, the zinc atom must give up two electrons from the 4S orbital to an oxygen atom, which subsequently has a plain 2P orbital with six electrons. The formation reaction of ZnO is given by [47]:

$$Zn^{+2} + \frac{1}{2}O_2 + 2e^- \rightarrow ZnO \qquad \text{(I.6)}$$

The theoretical study represented in figure I.21 illustrates the appearance of the band structure, revealing that ZnO is in the reciprocal space at the Brillouin zone. In this structure, there are six Γ bands resulting from the 2P states of oxygen, and the lowest of the conduction bands have a strong contribution from the 4S states of zinc. This figure indicates that ZnO is a direct-gap semiconductor because the minimum of the conduction band and the maximum of the valence band are located on the same axis Γ (in the center of the Brillouin zone: point Γ where k = 0).

As for its conduction properties, stoichiometric ZnO is insulating but becomes n-type degenerate because of the presence of systematic defects, such as oxygen vacancies and zinc atoms in the interstitial position (native defects). At room temperature, bulk ZnO has a gap of 3.37 eV, allows vertical transitions between the valence band and the conduction band (the gap corresponds to the energy required to move an electron from the BV to BC), and has radiative transitions. This value varied with temperature. When foreign atoms are introduced (doping), the nature and rate of doping vary according to the width of the forbidden band.

On the other hand, the passage of electrons from the valence band to the conduction band creates an electron-hole pair linked by a Colombian interaction within the crystalline structure (called an exciton). The binding energy of the exciton is 60 meV, which is the largest in the II-VI family. At room temperature, the binding energy is greater than the energy of thermal agitation (23 meV), which means that the exciton created will not be thermally annihilated [47].

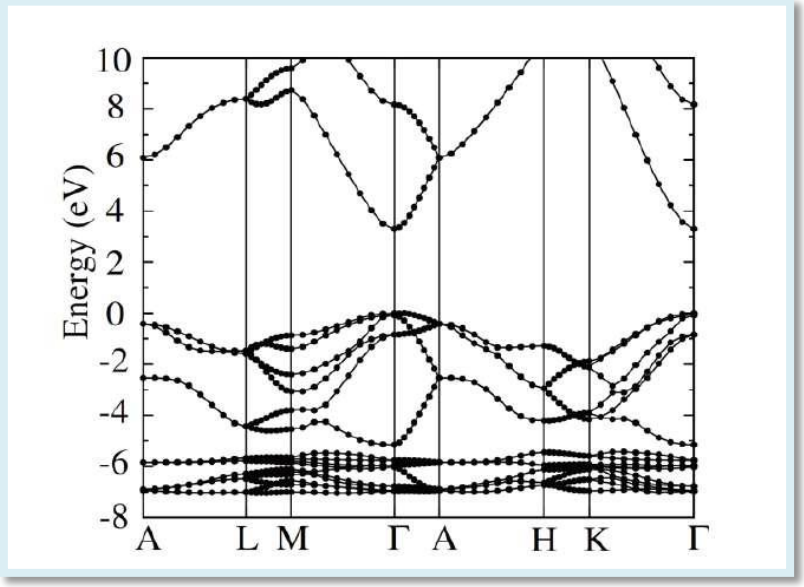

Figure I.21: Band structures of wurtzite ZnO [47].

I.3. Intrinsic Defects in ZnO

The understanding of both intrinsic and extrinsic defects in any semiconductor is crucial to utilize their properties in different semiconductor devices [48]. There are two types of intrinsic defects that occur in ZnO: the deep defects abd the shallow defects (Figure I.22). The shallow defects located a few tens of meV from VB and CB. These last defects are doping defects, will create the bound excitons. They will eventually induce discrete energy levels in the ZnO wurtzite gap, influencing significantly the optoelectronic properties of the material. The deep defects, whose energy levels are located a few hundred meV or a few eV from the valence band (VB) and conduction bands (CB), these defects are intrinsic in the ZnO film, such as zinc interstitials, zinc vacancies, oxygen interstitials, oxygen vacancies, and zinc antsites.

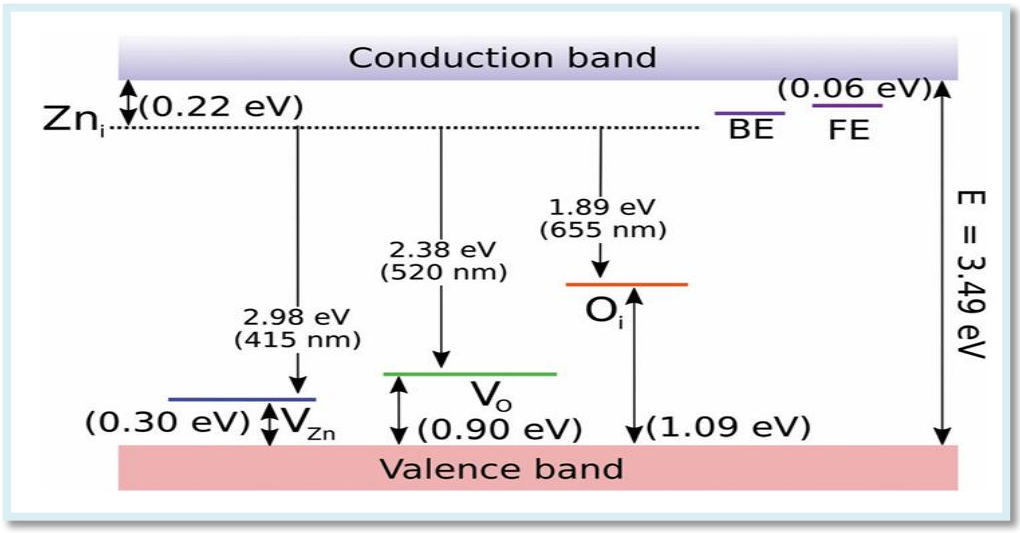

Figure I.22. Implantation in the forbidden band of deep and shallow defects [49].

I.3.1. Zinc interstitials

Zinc interstitials (Zn_i) consists of two different interstitial sites primarily in wurtzite ZnO, i.e. octahedral and tetrahedral sites. Octahedral sites are occupied by Zn_i due to their

stability where as tetrahedral sites are reported to be unfavourable [49] where as they are reported to be unstable by Sokol et al. [50]. In the tetrahedral site, the Zn-O bond length along the c-axis is approximatelly $0.833d_0$ and the octahedral have three Zn and O atoms with a distance of about $1.07d_o$ (d_o is the Zn-O bond length along the axis).

Therefore, it can be expected that octahedral sites are more preferable due to fewer geometric constraints. In n-type ZnO, the formation energy of Zn_i is considered to be high while its concentration is considered to be low according to Kim et al. [51]. They recommended that in the presence of a high concentration of oxygen vacancies, Zn_i can be stabilized. But in the case of p-type ZnO, formation energy is very low and hence, holes in p-type ZnO can be compensated by Zn_i [51].

I.3.2. Zinc vacancies

When zinc is missing or removed from its native position to an interstitial site, it produces zinc vacancies (V_{zn}). Erhart et al. [52] has reported V_{zn} to be dominant defect in ZnO. These V_{zn} initiate partially occupied states in the band gap and is made up of four oxygen atoms with dangling bonds. Zinc vacancy exists in three states, V_{Zn}, $V_{\bar{Z}n}^{1}$ and $V_{\bar{Z}n}^{2}$ as these dangling bonds of oxygen combine by forming a doubly charged state which lies close to the valence band induce three partially occupied states.

Even in zinc-rich conditions, the formation energy of V_{zn} is very high. It is up to 6.39 eV whereas it is 3.7 eV in oxygen-rich conditions. Concerning formation energy, under O-rich conditions for zinc vacancy is lowest as V_{zn} is related zinc deficiency. Kohan et al. [53] mentioned that due to acceptor defects and by exhibiting n-type conductivity green luminescence in photoluminescence spectra originates from V_{zn} levels.

I.3.3. Oxygen interstitials

When an extra oxygen atom in a lattice is positioned at the interstitial position, it is referred to as oxygen interstitial (O_i). The formation energy of O_i is up to 6.83 eV with a migration barrier of about 0.9 eV. Erhat et al. [54] have reported few configurations in O_i such as octahedral and molecule of O_2, like configuration dumbbell or split config uration. The formation energy of O_i in octahedral configuration was found to be higher than that of Zn vacancy [54]. Under n-type conditions, the formation energy of split configuration is low after a comparison with octahedral configuration.

I.2.4. Oxygen vacancies

Oxygen vacancies V_O, refers to an O atom that is missing from its lattice site. Even under Zn-rich conditions, the formation energy of V_O^+ is 0.81 eV which is very low compared to other defects, which suggests that the formation of V_O, is easier and concentration under equilibrium conditions will be more. Electronically, V_O has four bonds and two electrons and exists in three different states, V_O, V_O^+, V_O^{+2}, where V_O^{2+} is the least stable amongst V_O and V_O^+. However, these oxygen vacancies are deep donors. There has been discussions about the origin of green luminescence on the basis of a few experimental results of electron param-agnetic resonance by Vanheusden et al. [55]. V_O have been attributed to green luminescence by Leiter et al. [56] and Hofmann et al. [57].

The calculations done by Janotti et al. [58] on the formation energy of neutral V_O, which suggest that it has low formation energy and the migration barrier in n-type ZnO is 2.04 eV. For p-type ZnO, oxygen vacancies act as a potential source of compensation [58].

I.3.5. Zinc antisite

Zinc antisites refer to a Zn atoms placed at the wrong lattice or in place of O atoms. They are shallow donors and possess at high formation energy 4.98 eV. Kohan et al. [53] have also concluded that the formation energy in these defects is higher as compared to other defects. Even under Zn-rich conditions, they remain unstable due their high formation energy. Zn antisites are regarded as a complex of V_O, and Zn_i, having very deep and shallow levels. The position of Zn antisites in the relaxed geometry is displaced by more than 1Å the O site. In n-type ZnO, the formation energy of these complexes is more than Zn_i [51].

I.4. Doping of ZnO

The last decade has witnessed an enormous growth of ZnO related research, largely because of the possibilities of new or improved types of electronic and photonic devices. One of the effective methods for manipulating the physical properties of semiconductors is doping the impurity ions. It has been proved that the physical and chemical properties are greatly influenced by doping of the foreign metals in ZnO lattice. The doping of ZnO is a research topic of considerable interest in its own right. It can be in the form of impurities or native defects in the lattice [59].

The best doping candidate should have high solubility, be relatively stable within the crystal lattice, and have sufficiently low ionization energy. There are several studies and results in the literature showing that it is possible to dope the ZnO matrix with generally metallic elements according to the desired physical properties ; for example for optoelectronic properties, we can cite Aluminum (Al), magnesium (Mg) and indium (In) [60, 61], and for magnetic properties Cobalt (Co), Copper (Cu) and manganese (Mn) [62-64]. Doping in ZnO can be classified into two types, cationic and anionic doping. The cationic doping is the

process of doping a cation such as, Al, Sn, Ga, In, Cd, Cu, Fe, Co, Mn, and Ni. However, anionic doping is the doping of anions e.g. As, N, and S. For example, incorporation of Mn resulted in a decreased crystallite size, bandgap and transparency. Red-shift of absorption edge is observed clearly with Manganese doping [65].

I.4.1. Noble metals doped ZnO

Noble metal-doped zinc oxide nanostructures represent a cutting-edge class of hybrid materials that synergistically combine the semiconductor properties of ZnO with the unique characteristics of copper, silver, and gold [66]. These engineered materials exhibit remarkable enhancements in optical, electronic, and catalytic properties compared to pure ZnO, making them highly attractive for diverse technological applications.The incorporation of noble metals into the ZnO lattice induces profound modifications at the atomic level. Copper doping creates intermediate energy states within the bandgap, significantly improving visible light absorption [66, 67].

Silver introduces strong surface plasmon resonance effects, while gold combines both localized states and plasmonic behavior, extending light absorption into the near-infrared region. These electronic modifications enable precise bandgap engineering from 3.37 eV down to 3.0 eV, tailoring the materials for specific applications. The materials also show tremendous potential in sensing technologies. Copper-doped nanowires detect volatile organic compounds at parts-per-billion levels, silver-doped structures enable nanomolar biomolecule detection, and gold-doped photodetectors achieve responsivities exceeding 20 A/W. Their multifunctional capabilities extend to spintronic devices, where they exhibit room-temperature ferromagnetic behavior and spin-polarized transport properties [68].

I.4.1.1. Al-doped ZnO

Impurity-doped ZnO-based binary compounds, such as Al-doped ZnO are emerging as an alternative potential candidate to ITO since they are inexpensive, nontoxic and much abundant materials in Earth's crust. Al-doped ZnO films are stable in reducing ambient hydrogen plasma and atmosphere and are used in the deposition of hydrogenated silicon thin films. It has been recognized that a small amount of Al doping in a ZnO matrix (Figure I.23) is known to enhance the charge carrier density and thereby reduce the resistivity of the material [69]. The Al^{3+} ions are incorporated in Zn^{2+} tetrahedral sites of the ZnO matrix, donating charge carriers and forming a degenerate semiconductor with reduced resistivity. Optically, this blueshifts the absorption edge of the film in accordance with the Burstein–Moss effect [69-71].

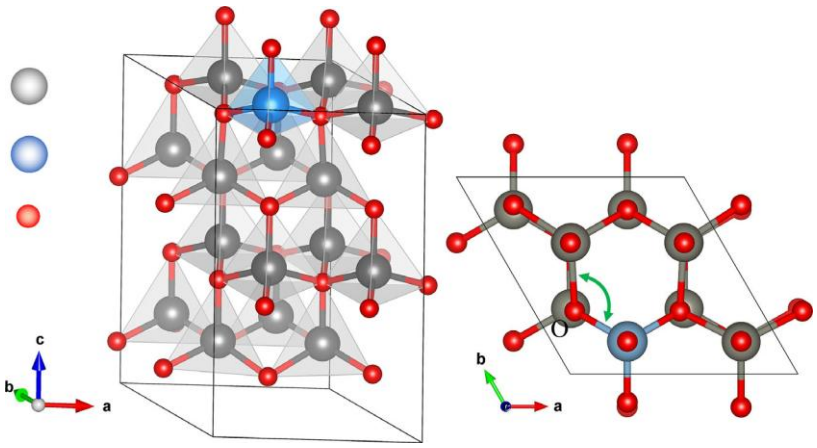

Figure I.23. Wurtzite crystal structure of Aluminum-doped Zinc oxide [72].

AZO films are also wide band gap semiconductors, which show good optical transmittance in the visible and near-infrared regions. It was shown that the surface roughness decreases as the Al doping concentration increases. The surface would become smoother due to the enhanced

nucleation sites. Due to these unique properties, AZO films have been used as transparent conducting electrodes in solar cells [73].

I.4.1.2. Cu-doped ZnO

Copper (Cu) has proven particularly intriguing due to its unique electronic configuration and ionic radius, which closely matches that of Zn^{+2} (0.074 nm for Zn^{2+} and 0.073 nm for Cu^{2+}) [74] allowing Cu^{2+} to readily enter the substitutional sites of the ZnO lattice (Figure I.24), consequently altering its emission and absorption spectra towards the visible range.

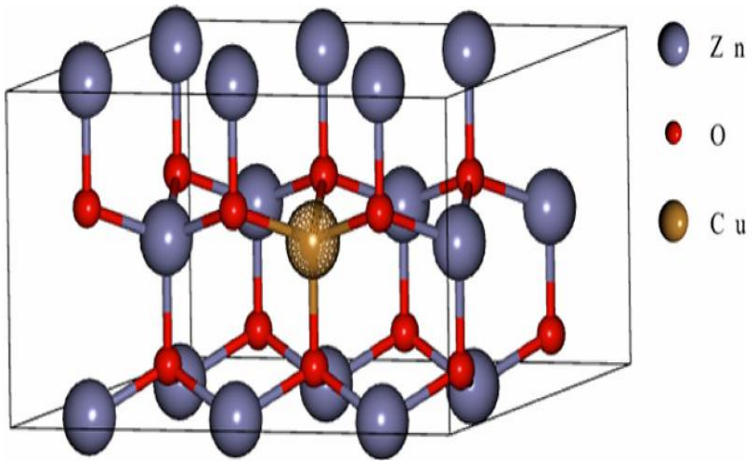

Figure I.24. Wurtzite crystal structure of Copper -doped zinc oxide [75].

Copper is considered an effective dopant material for ZnO due to the following reasons: (1) it possesses conspicuous luminescent activators that create localized trapping levels in the band gap, thus lowering the e^{-}-h^{+} pair recombination rate, (2) Physico-chemical properties of Cu are comparable to Zn, microstructure character istics (particle size and form),

(3) it is feasible to modify the wavelength of absorbance towards the longer side by doping Cu into ZnO, thereby decreasing its optical band gap [76]. Cu is thought to be the most effective of them for enhancing ZnO's photocatalytic performance. Cu doping in ZnO causes major changes in its electrical, optical, and magnetic characteristics. The visible spectrum absorbs light due to the lattice defects caused when Cu is added to ZnO, improving photocatalytic activity. The synthesis of Cu-doped ZnO microstructures was reported by Pawar et al. [73].

I.4.1.3. Ag-doped ZnO

The silver ion (Ag^{+}) has a larger ionic radius than the Zn^{2+} ion. Thus, substituting Ag^{+} in the host ZnO increases the unit cell volume (Figure I.25). This results in shifting the XRD pattern towards a lower 2θ value. However, the solubility of Ag in the ZnO matrix is difficult due to its larger ionic radii. Thus, it forms separate crystals, or aggregates, as heterojunctions. Zyoud et al. [77] reported a small amount of Ag inclusion in the host ZnO based on the XRD peak shift. However, the dominance of heterojunctions (independent crystal formation) was confirmed. The Ag crystals form local contact with ZnO, facilitating the interface's in situ charge transfer process. This charge transfer was confirmed based on the Ag^{+} ion and Ag^{0} 3d XPS peak shift compared to the single Ag. The Ag $3d_{5/2}$ and $3d_{3/2}$ peak shift towards lower binding energy were attributed to the change in electron density due to transfer. Besides, Wang et al. [78] also reported the dominance of independent Ag crystal formation instead of its inclusion in the host lattice. Here, the XPS Ag 3d peaks also shifted towards lower binding energy than their bulk counterparts. The shift also confirmed the presence of Ag/ZnO charge transfers [79]. The benefits of Ag doping are multifaceted. It not only improves the electrical properties but also enhances ZnO's luminescence, pivotal for optoelectronic devices. Ag is a

standout dopant, potentially inducing shallow acceptor levels in ZnO and demonstrating amphoteric doping behavior, which enhances luminescence efficiency and photocatalytic activity in ZnO nanostructures [80].

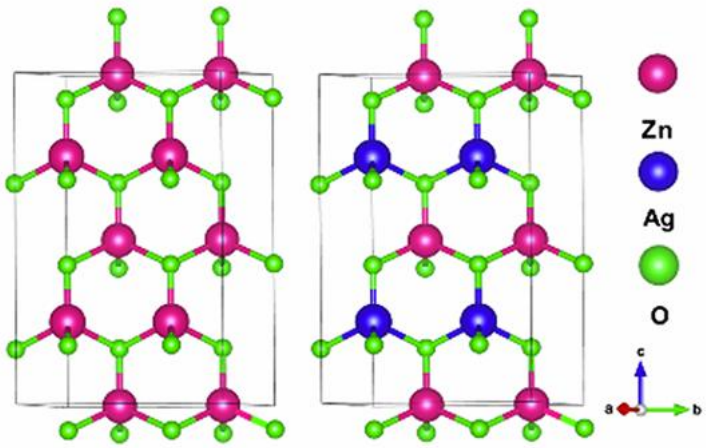

Figure I.25: Wurtzite crystal structure of Silver -doped zinc oxide [81].

I.4.2. Transition metals doping of ZnO

Transition metal doping in the crystal structure of ZnO is a widely recognized approach to making zinc oxide active under visible light. Doping ZnO with transition metals can alter its shape, crystallite structure, and particle size. Doping enhances the photodegradation efficiency of ZnO by generating defects, specifically oxygen vacancies and trapped states within the photocatalyst. These defects and trapped states capture photogenerated electrons that effectively limit the e^--h^+ pairs recombination rate [82]. After transition metal doping, ZnO's optical absorption edge expands into the visual spectrum. The potential cause for this phenomenon is the electron interaction at the band edge of ZnO with the localized d-elec trons of the TM ion in the sp-d orbitals, where they exchange spin states

[83]. Thus, photo-catalysis can be stimulated using visible light on modified ZnO [84]. Transition metal doping can reduce the effective bandgap of ZnO, playing a vital role in the optical, electric, and magnetic properties.

The magnetic ions doped ZnO can have both magnetic (spin) and semiconducting (free charge carriers) properties, so such materials are generally called dilute magnetic semiconductors (DMSs) or semi-magnetic semiconductors. The DMS materials are promising candidates for spintronic applications such as spin field transistor, quantum computer and non-volatile magnetic devices [85].

I.4.2.1. Mn-doped ZnO

The manganese ion (Mn^{2+}, 0.66 Å) has a slightly greater tetrahedral ionic radius than Zn^{2+} (0.60 Å), and this ionic radius results in an XRD pattern peak shift towards a lower angle due to the lattice enlargement. In addition, doping with Mn^{2+} ions creates different intrinsic defects (especially Zn_i and O_v) that act as charge carrier traps. The trap centre occurring increases their relaxation time for redox reactions. Several reports show that the solubility of Mn is lower due to the stronger metal–oxygen bond for Mn–O than that of Zn–O. However, the magnetic (antiferromagnetic and ferromagnetic) properties of Mn–ZnO are much better than those of Cu–ZnO due to the presence of five unpaired electrons in d-orbitals. Sharma et al. [86] conducted detailed XPS and PL analyses to confirm the inclusion of Mn in the ZnO lattice without affecting the würtzite structure of the host ZnO. XPS analysis showed that the oxygen vacancy concentration could be controlled by calci nating the materials in vacuum and air. When the sample was calcinated under vacuum, the oxygen vacancy peak increased, and in air, it decreased. The increase in vacuum confirmed the creation of defects, and the

decrease in air showed the filling of oxygen defects by oxygen from the air. PL analysis showed a deep-level emissions peak in the visible region. The intensity increase for the green band with the dopant amount indicated an increase in oxygen vacancy concentration. In the same analysis, intense near-band-edge (NBE) shifeed towards a longer wavelength (red shift), signifying the incorporation of Mn in the ZnO host lattice. Besides, all doped materials with different Mn dopant concentrations showed ferromagnetic ordering proper ties. The ferromagnetic property was mainly due to the oxygen vacancies created during doping, which increased as the doping concentration increased. A slight low-angle XRD pattern shift was also confirmed for Mn-doped ZnO compared to ZnO. This shift resulted from slight unit cell expansion due to the greater ionic radii of Mn.

Ali et al. [84] also conducted a detailed theoretical and experi mental study on Mn-doped ZnO. The study confirmed the ferromagnetism properties of Mn–ZnO material to be due to zinc vacancy (V_{Zn}). The presence of defects in the doped mate rial was analyzed using XPS. The analysis used different concentrations of argon and oxygen atmospheres (20 Ar/80 O_2 and 80 Ar/20 O_2 atmospheres). The shifting of Zn $2p_{3/2}$ and Zn $2p_{1/2}$ peaks towards higher binding energy for doped materials in the presence of a lower argon atmosphere confirmed the domination of V_{Zn}. In addition, the PL analysis showed a peak at 410 nm, mainly due to the electron transition from V_{Zn} levels to the ZnO host CB. Another peak at 570 nm was associated with the V_O defect [83].

I.4.2.2. Co-doped ZnO

Cobalt ion (Co^{2+}, 0.58 Å) has comparable ionic radii with Zn^{2+} (0.60 Å) in tetrahedral coordination. Thus, incorpo rating Co^{2+} ions in the ZnOlattice also results in an XRD pattern with a higher angle shift. Besides, the solubility of Co^{2+} ions in the ZnO lattice is much better than that of other metal ions. Thus, Co doping with greater solubility creates new Co^{2+} 3d

levels, or mid-edges. The doping also extends the visible light absorption capacity due to the s–d and p–d interactions. Once the Co^{2+} 3d states are created, different charge transitions occur. The transfer includes VB–CB, donor-type transition ($Co^{2+/3+}$, dopant to host CB), acceptor-type transition ($Co2^{+/+}$, dopant to host VB), and dopant d–d transition (Figure I.26).

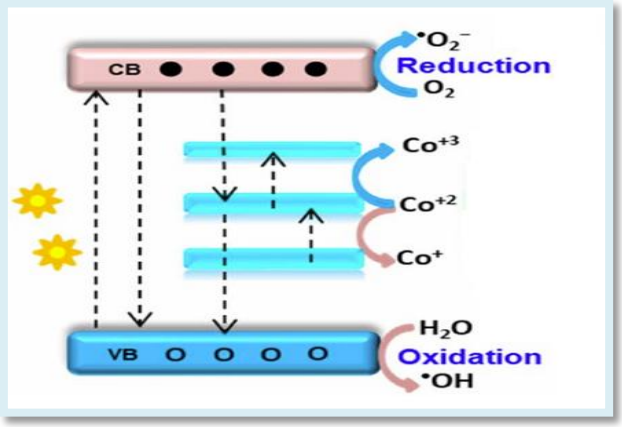

Figure I.26. Scheme showing probable charge transfer within cobalt doped ZnO : valence to conduction band, cobalt (III) level to host conduction band, cobalt (III) to host valence band, and dopant d d transition [87].

This extrinsic inclusion of Co^{2+} ions in the ZnO lattice is due to the s–d or p–d exchange interaction between the host band electron and 3d localized dopant electrons, creating a new energy level. The study also reported that a host lattice strain was created with an increased Co amount, resulting in cluster formation, morphological change, and enhanced defect density. Chen et al. [87] obtained three absorption bands in the visible region attributed to Co^{2+} d–d electronic transitions, indicating the proper substitution of Zn by Co^{2+} ions without affecting the host ZnO structure. The band gap analysis using the Kubelka–Munk function confirmed the presence of two regions for UV and visible light absorption.

The VB maxima, CB minima, Fermi tail, Fermi level, cut-off tail, and band gap were determined by ultraviolet photoelec tron spectroscopy. This confirmed the dominance of VB

maxima by the O-2p orbital and the increase of CB minima by Co atoms. The study also confirmed the formation of a mid state band gap to enhance visible light absorption.

Chehhat et al. [88] used the sol–gel method to synthesize Co ZnO with a porous structure. The PL analysis showed a band edge shift towards a higher wavelength than single ZnO. This shift indicated the presence of s–d and p–d exchange interac tions due to the Co interchange by Zn. The PL analysis by Kaphle et al. [89] showed an intensity reduction with increased Co concentration. This intensity reduction indicated a reduction in electron–hole recombination due to the dopant acting as an electron sink. The PL spectra of ZnO showed a broad, small peak in the visible region due to intrinsic defect-related green emission. The intensity of the broad emission peak increased with Co concentration, indicating the formation of more defects. Chanda et al. [90] also reported an increase in defect related emission peak intensity with an increase in Co amount, indicating an increase in defects. The PL analysis by Kaphle et al. [88] also showed an increase in NBE emissions and a decrease in visible emissions. Besides, the calcination temperature affects both the formation of defects and crystal linity. An increase in temperature leads to an increase in EHR and crystallinity and a decrease in defect formation. However, high-temperature calcination in an oxygen-rich environment results in an oxidation process that increases oxygen content.

Doping with Co also tunes ZnO's magnetic properties due to cobalt's highest magnetic moments and positive magnetic exchange coupling constant. Kazmi et al. [91] confirmed the ferromagnetic properties of Co–ZnO 1D nanowires. The ferro magnetic properties were confirmed based on the density functional theory analysis. The Co 3d spin-polarised electrons and host O-2p electron exchange integration caused the magnetic property. The intrinsic defects and substitution occurred without secondary Co-metal or Co_3O_4 phase forma tion. Salameh et al. [92] confirmed the formation of defects (oxygen vacancies) by XPS. The

analysis showed a unique peak at 531.0 eV, indicating the presence of electrons in the oxygen vacancies. The intensity of this peak increased as the Co concentration increased [92].

I.4.2.3. Fe-doped ZnO

Iron (Fe) is regarded as the most influential metal dopant because of its exceptional chemical stability and ionic radii. The Fe^{2+} and Fe^{3+} have ionic radii of 0.78 and 0.64 Å, respectively, mirroring the ionic radius of Zn^{2+} (0.74 Å). Therefore, no significant changes to the lattice structure of the parent semi conductor are observed upon iron (Fe) incorporation into the ZnO lattice. The effectiveness of the catalyst is significantly enhanced at the modest doping concentration of Fe ions, which effectively separates the photogenerated holes and electrons [93].

Rajan et al. [93] studied the detailed local structural analysis of Fe^{2+}/Fe^{3+}–ZnO materials. Here, dopant solubility of up to 10% was reported. The UV-vis analysis shows a mid-absorption band in the visible region. The band is mainly due to the doped Fe^{3+} high-spin crystal field transitions from the 6A1g ground state. The Tauc plots also showed redshift for Fe–ZnO due to the sp–d exchange interac tion. The peak edge position in the X-ray photoelectron spec troscopy (EXAFS) analysis is associated with Fe_2O_3 (Fe^{3+}) states. The edge shows the inclusion of Fe^{3+} in the ZnO lattice. Besides, the XPS analysis showed the existence of the Fe^{2+} states in the lower dopant concentration, and they oxidized to the Fe^{3+} state with increasing concentration. Srinivasulu et al. [94] prepared, iron-doped zinc oxide (FZO) thin films have been on glass substrates by using chemical spray pyrolysis technique at different substrate temperatures (300–450 °C) for a constant Fe-doping concentration of 2 at.%. The obtained results indicated that an increase of substrate temperature (Ts) up to 400

°C led to an increase in the crystallinity, optical transmittance and ferromagnetic nature of the films. However, at higher substrate temperature (450 °C), the crystalline quality and phase purity of FZO thin film was degraded. The transmittance haze factor was evaluated from the total and diffused transmittance measurements and observed that a decrease in the haze with substrate temperature up to 400 °C indicated a lower scattering of the light in the films. The bandgap energy of FZO films was decreased from 3.44 eV to 3.20 eV with increase of substrate temperature up to 400 °C.

Gonullu et al. [95] have Fe-doped ZnO films (1, 2, and 3 %) onto glass substrates by ultrasonic spray pyrolysis. The films were thermally treated at 500 °C for 2 h. Their findings revealed that both Fe doping and thermal treatment changed film properties. Films presented hexagonal wurtzite structures without any secondary phases for all films. The preferential orientation (002) changed to dominant growth directions (100) and (002) according to the doping concentration and thermal treatment. The grain size of the ZnO nanogranules decreased after Fe doping and also thermal treatment. The optical transparency was found maximum of 77 % in the visible region. 3 % Fe doping and thermal treatment caused the reduction in the optical band gap values to 3.18 eV. Fourier transform infrared spectroscopy analysis presented the Z-O stretching, C-H vibration, and O-H stretching bonds. Shifting in the peak position indicated the Fe^{+2} ion substitution. Photoluminescence analyses revealed the reduced emission intensity with the effect of thermal treatment. Photocatalytic performance tests showed improved degradation efficiency after the films were thermally treated. Especially among Fe-doped films, thermally treated 1 % Fe-doped ZnO film showed a significant increment after as-deposited ones. Consequently, it has been uncovered that thermal treatment and Fe doping significantly influence the investigated film properties.

Taha et al. [96] investigated motivated the development of single-phase Fe/ZnO nanostructures by a direct sol–gel method. The structural, morphology, optical properties, and magnetic properties of the samples were studied using X-ray diffraction (XRD), transmission electron microscopy, X-ray photoelectron spectroscopy, UV–Vis spectroscopy, and vibrating sample magnetometer. Rietveld refinement of XRD data demonstrated single-phase nanocrystalline of Fe-doped ZnO without any secondary phases and there is an expansion in lattice unit volume with increasing Fe concentration.

The optical properties determined by UV–Vis spectroscopy showed decreasing in energy gap with dopant Fe. The magnetic measurements revealed that Fe-doped ZnO exhibits weak ferromagnetism at room temperature, with the value of magnetization increasing with Fe concentration. This room temperature ferromagnetism is caused by oxygen vacancy supported by bound magnetic polarons and probably grain boundaries. The dielectric measurements were carried out at 300 K and showed a decrease of both dielectric constant ($\varepsilon 1$) and AC conductivity (σAC) with increasing the Fe content.

I.5. Applications of Zinc oxide

ZnO continues to garner an extensive research interest owing to several of its promising applications. It has been the object of the renewed research for a wide range of applications such as light emitting diodes, laser diodes, gas sensor, thin film solar cells and spintronics [97]. These applications with high quality and reliable performance are related to preparation mode and post-treatment process of the sample in order to improve the chemical, electrical, optical, and morphological properties [97].

I.5.1. Solar cells

Solar cells or photovoltaic cells convert solar energy into electricity. Large area p–n junction is the basic requirement of the most commonly known solar cells (Figure I.27). In p–n junction, the electron deficient p-type layered semiconductor attracts the electron from the electron rich n-type semiconductor layer therefore minimizing electron-hole pair recombination [98].

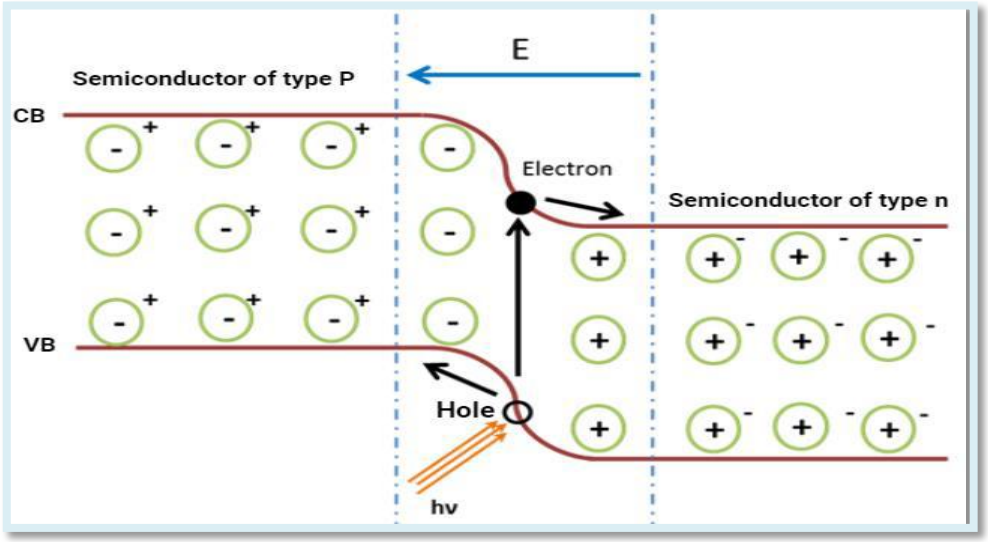

Figure I.27. Principle of operation of a photovoltaic cell with a pn heterojunction [99].

The desired properties of the charge transport materials for solar cells application are ideal energy levels that correspond to the high absorption efficiency of the solar spectrum, high carrier mobility, good conductivity, and efficient extraction of the excited carriers. Zinc oxide (ZnO) has been considered as one of the potential materials in solar cell applications, owing to its relatively high conductivity, electron mobility, stability against photo-corrosion and availability at low-cost [100].

I.5.2. Gas sensor

Gas sensors have many important applications like environmental pollution control, fire detection, as an alcohol breath analyser, industrial process controller or for detection of harmful gas leaks in mines and other industries. Semiconducting oxide-based gas sensors are easy to fabricate, have low cost and their surfaces have good sensitivity to the adsorbed gases. For good sensitivity, the film surface should have high grain density with a porous surface. ZnO being physically and chemically stable can be a good choice for thin film gas sensors (Figure I.28). Doping ZnO with suitable elements in appropriate amounts increases the surface density of grains and porosity thereby improving the sensing selectivity and response time of the film. The sensitivity further improves at high temperature.

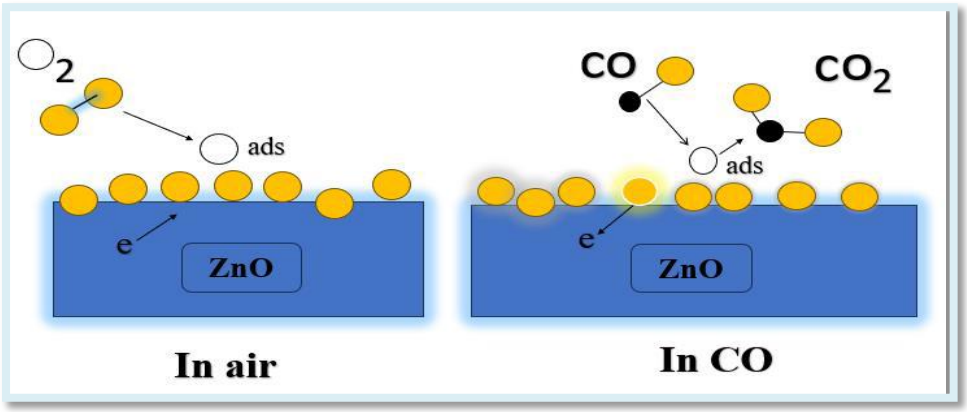

Figure I.28. CO sensing mechanism of ZnO Gas sensor [101].

The conductivity of ZnO thin film surfaces will increase or decrease depending upon the nature of reaction (oxidation or reduction) of the adsorbed oxygen on the surface of the ZnO thin film and the gas under test [101]. ZnO nanostructures have excellent gas sensing characteristics because to their oxygen-deficient surface, which quickly oxidises in the environment at high temperatures to attain ZnO surface stoichiometry. The chemisorption and

dissociation of oxygen on defect sites make ZnO very sensitive to metal oxide semiconductor (MOS) gaseous target chemicals [101].

I.5.3. Light emitting diodes

In the past decade, light-emitting diodes (LEDs) based on wideband gap semiconductor have attracted considerable attention due to its potential optoelectronic applications in illumination, mobile appliances, automotive and displays. The wide bandgap and large exciton-binding energy at room temperature of ZnO make it a very promising candidate for fabrication of blue and UV LED, which requires that the junction devices provide high electron and hole concentration in the active region. ZnO is widely available and cheap, so it has an advantage over GaN from the cost point of view which also make the fabrication of ZnO-based optical devices an attractive prospect. The commercial success of GaN-based optoelectronic and electronic devices trig the interest in ZnO-based devices. In contrast, the lack of stable and reproducible p type ZnO become a limiting factor in realising ZnO based LED. n-type ZnO thin film which is grown on other p type materials like Si, GaN, zinc telluride, copper(I) oxide and GaAs was a suggested alternative approach. Various ZnO based heterojunction and homojunction light emitters in the UV and visible ranges (red, blue, green or white) have been reported [102].

I.5.4. Diluted magnetic semiconductors

The diluted magnetic semiconductor systems are defined as being semiconductor matrices substituted with a fraction of magnetic impurities, which retain not only the

semiconductor properties owing to the electron charge but also receive magnetism via the electron spin. Spintronics is the field of electron technics, which focuses its attention on creating functional devices based on control of ferromagnetic ordering by electric field. In this regard, two criteria should be taken into account by DMS materials for successful applications in spintronic technologies. On the one hand, a ferromagnetic behavior with a Curie temperature (Tc) above room temperature (RT) must be produced; and on the other hand, a relatively high magnetization must be generated by substituting the host semiconductor with magnetic impurities. Interest to ZnO as a promising material for DMS arises as a result of several theoretical predictions that it could be ferromagnetic with high (Tc) at doping by transitional 3d-metals. Besides that ZnO is optically transparent therefore a transparent ferromagnetic could be created [103]. Spintronics is a new emerging field based on a combination of three conventional information carriers: an electron charge, an electron spin and a photon, as shown schematically in figure I.29. These carriers represent three major fields in information technology (IT); data processing with electron transport, data storage with an assembly of spins and data transfer via optical connections [103].

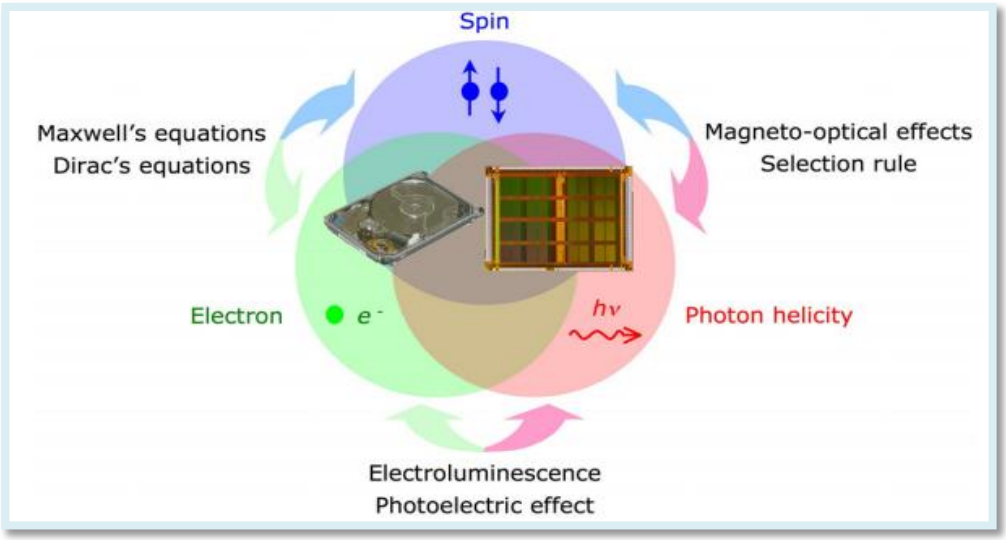

Figure I.29. Concept of spintronic device applications [103].

I.6. Aim of the thesis

According to it unic characteristics, as it was presented, TM-doped ZnO became one of the most used material as a DMS. Many research aimining to only improve its spinotronic properties gave promising results for the unic application as a DMS or DMO (for Deluted Magnetic Oxides). However, even doped with transition metals, optoelectronic properties or ZnO and the impact of TM doping on them remain of a great interest. This material is still demanded for other applications such as solar cell, gas sensor and LED.

In the experimental work, we have used the spray pyrolysis technique for the preparation of our samples aiming to:

Study of the effect of doping ZnO thin films by Mn, Co, and Fe on its structural and optical and luminescence properties.

.

Chapter II

Deposition conditions and characterization techniques

II.1. Deposition conditions

II.1.1. Deposition technique

In this work, thin films of ZnTMO (TM=Co, Fe, and Mn) were deposited using the spray pyrolysis technique. The films were prepared at the Laboratory of Research on Physico-Chemistry of Surfaces and Interfaces (LRPCSI) of the University of Skikda. The apparatus used is a simple manual perfume sprayer in which the precursor solution is added. The precursor solution is sprayed from a distance of 20 cm from the substrate, with its nozzle oriented perpendicularly to the heated borosilicate glass substrate. The desired temperature of 450°C is controlled using a thermocouple connected to a digital thermometer.

II.1.2. Precursor solution

For the three prepared sample series, 0.1 M Zn-rich solution is prepared by dissolving the appropriate weight of zinc (II) chloride ($ZnCl_2$) in distilled water. For the doping elements, 0.1 M of Co-rich solution, 0.1 M of Fe-rich solution, and 0.1 M of Mn-rich solution were prepared by dissolving the appropriate weight of respectively cobalt (II) chloride ($CoCl_2$), iron (II) chloride ($FeCl_2$), and manganese (II) chloride ($MnCl_2$) in distilled water.

For the deposition of ZnTMO thin films, the sprayed precursor solutions are prepared by mixing a volume of Zn-rich solution V_{Zn} with a volume of the TM-rich solution V_{TM}. The TM molar ratio X=0.00, 0.02, 0.04, 0.06, 0.08, and 0.10 (for TM=Co and Fe) and X=0.00, 0.02, 0.04, and 0.06 (for TM=Mn) was calculated using the following relation:

$$X = \frac{V_{TM}}{V_{Zn}+V_{TM}} \qquad \text{(II.1)}$$

The deposition parameters were identical for the three samples series. The number of sprays is 160 sprays and the spray rate is 140 mm^3 per spray. The spray frequency is one

spray per 30 seconds. The resulting thin films were uniform and exhibited the typical white-transparent color associated with ZnO.

II.2. Characterization techniques

When manufacturing or using fabricated thin-film materials and devices, it is important to illustrate the different properties or characteristics of the synthesized films and novel materials according to the characterization process. The latter includes the crystalline structure, morphological surface, compositional properties, optical properties, etc. This section describes the various techniques used to characterize the as deposited MT-doped ZnO thin films.

II.2.1. X-Ray diffraction

X-ray diffraction (XRD) technique is a powerful, non-destructive characterization tool with minimal sample preparation. XRD provides the first information about the materials phases, crystalline structure, average crystallite size, micro and macro strain, orientation parameter, texture coefficient, degree of crystallinity, crystal defects etc. XRD analysis provides information about the bulk, polycrystalline thin films, and multilayer structures, which is very important in various scientific and material engineering fields [104]. Bragg's law is considered as the primary principle behind X-ray diffraction (Eq. II.2). When monochromatic X-rays affect upon the atoms in a crystal lattice, each atom acts like source of scattering. As shown in the schematic in figure II.1, the crystal lattice functions as group of parallel reflecting planes. The intensity of the reflected rays reaches the maximum at particular angles (constructive interference) when the path difference between two reflected

waves from two different planes in an integral multiple of the X-rays' wavelength λ. This is known as Bragg's law that is presented by the following relation [105]:

$$2d_{hkl}\ sin\,\theta = n\lambda \qquad \text{(II.2)}$$

With d representing the inter-reticular distance of the crystal lattice, λ is the wavelength of the incident beam,n is an integer that represents the order of the reflection and θ represents the angle of incidence of the X-rays with respect to the surface of the sample.

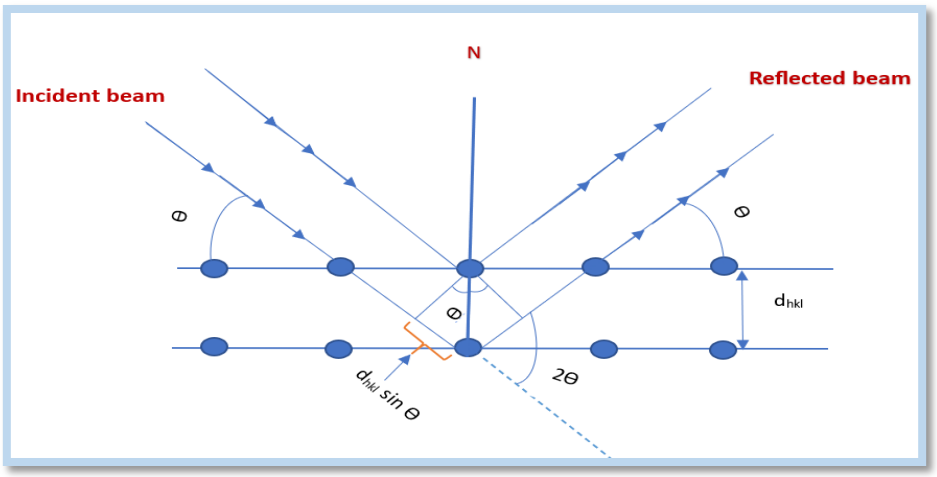

Figure II.1. Schematic description of Bragg's Diffraction Law [105].

In the same compound, several plane families can be present. It is for this reason that a fairly wide angular sweep is performed. The variation of the angle makes it possible to determine the angles for which n is an integer in the Bragg equation. The angle being thus known and the wavelength being predetermined and constant, it is then possible to determine the reticular distance *d*. The determination of the relative intensity of the diffraction peaks involves the division of the absolute intensity of a given peak by the absolute intensity of the most prominent peak, followed by the conversion of this ratio into a percentage value. Absolute intensity values are generally not used because they vary with instrumental and

experimental settings. The number of detected atoms that correspond to this peak plane and the density of the atoms electron cloud are directly related to the area beneath the peaks. The diffraction pattern is specific and unique to a single phase, even if phases have the same chemical composition. The position of the peaks, as well as their relative intensities, is used for comparisons in databases thus leading to the identification of the phase(s) present [106].

II.2.1.1 Determination of lattice parameters

The physical and chemical properties of minerals are influenced by the arrangement of atoms in the crystal structure. Lattice parameters can significantly affect the properties of minerals. These parameters are also known as unit cell parameters because they express the shape and size of unit cells and crystals. In the case of ZnO (hexagonal lattice), the relationship between interplanar spacings of the (hkl) planes and crystallographic parameters is as follows:

$$d_{hkl} = \frac{a}{\sqrt{\frac{4}{3}(h^2+k^2+hk)+l^2\frac{a^2}{c^2}}} \quad \text{(II.3)}$$

Comparing the obtained values for the parameters a and c with the theoretical values (a_0 = 3.249 Å and c_0 = 5.206 Å in JCPDS No. 5-664 datasheet) provides information about the state of stress in the considered powder [107].

II.2.1.2 Determination of crystallite size

Crystallite size is particularly significant for microstructural and physical features of any crystalline materials, since small crystallites are characterized by large surface areas, and vice versa. In crystalline solids, microstrain corresponds to the intrinsic stress of crystal planes, which might emerge as either compressive or tensile forces. As a consequence of microstrain, crystallite deformation occurs, giving conception to changes in the properties of

substances, notably in suitability. A constant variation in microstrain has emerged from the estimated data produced by applying the formula:

$$\delta = \frac{1}{(D_c)^2} \quad \text{(II.4)}$$

Imperfection in crystalline materials is displayed because of several flaws such as point dislocation, line dislocation, and area dislocation, frequently known as dislocation. Dislocation density analyzes the number of dislocation lines per given surface area and is directly linked to the crystal size. However, the amount of line dislocation is computed using as follows:

$$\varepsilon = \frac{\beta}{4 \tan \theta} \quad \text{(II.5)}$$

Precise crystallite size estimation is essential for various applications. Several methods have been employed for this purpose such as Scherrer's method, Monshi-Scherrer method and Williamson–Hall method.

II.2.1.2.1 Scherrer's method

We could calculate the average crystal size and overlook the influence of the strain by using the Scherrer method with the following:

$$D_c = \frac{k\lambda}{\beta \cos \theta} \quad \text{(II.6)}$$

Here, D_c indicates the crystallite size, K is the shape constant, wavelength (λ) of the Cu-radiation was 1.54056 Å for $CuK_{\alpha 1}$ radiation, β is the full width of the reflection at half of the maximum intensity, and the diffraction angle is θ [108].

II.2.1.2.2 Monshi–Scherrer method

The Scherrer equation reveals higher nanocrystalline size when d-spacing as well as 2θ values drop. Modifying the equation may eliminate shortcomings or $\Sigma(\pm\Delta \ln \beta)^2$ to offer a more accurate evaluation of crystal size from all or a part of unique peaks, enhancing the stability of βcosθ. The Monshi–Scherrer method is shown in described by Eq. II.7, with the dimension of the crystallite being indicated by $D_{M\text{-}S}$.

$$ln\beta = ln\frac{1}{cos\,\theta} + ln\frac{K\lambda}{D_{M-S}} \quad \text{(II.7)}$$

This model was examined by plotting lnβ and ln 1/cosθ on the Y-axis, and X-axis. The straight-line equation (y = mx + c) and equation (II.7) were compared with each other to find out the slope, which gives a checkpoint for verifying the correctness of the findings [108].

II.2.1.2.3 Williamson–Hall method

The modified Scherrer's Equation addresses crystallite size impact through XRD reflection, neglecting inherent strain in nanocrystals. However, intrinsic strain is crucial due to grain boundaries, point defects, dislocations, and stacking in nanocrystals. Consequently, the Williamson-Hall approach analyzes strain from XRD peak widening, following estimating intrinsic strain from crystallite size values [108]. This approach is more accurate for calculating crystallite size with several reflected peaks. Eventually, the overall broadening may be described as:

$$\beta_{Total} = \beta_{Size} + \beta_{Strain} \quad \text{(II.8)}$$

where β_{size} is the broadening due to its size and β_{strain} is connected to the strain broadening effect.The Uniform Stress Deformation Model (USDM) was validated by incorporating the

anisotropic character into lattice strain analysis. This modified model focuses on the lattice deformation stress for crystal plane directions with low microstrains uniformly, addressing the issue of sample uniformity and the potential anisotropic nature of actual crystals. Hooke's law (Eq. II.9) relates stress (σ) and strain (ε), with higher accuracy for low-stress values.

$$\sigma = Y_{hkl}\varepsilon \tag{II.9}$$

where Y_{hkl} is Young's modulus or modulus of elasticity, the mathematical expression is just an approximation that is reliable for a minimal strain. Furthermore, raising the strain produces a variation of particles from being linear in nature, respectively. By rearranging and replacing eq. II.9 with eq. II.10, we have eq. II.11.

$$\beta_{hkl}\, cos\, \theta = \frac{K_B\lambda}{D_{hkl}} + 4\varepsilon \sin\theta \tag{II.10}$$

$$\beta_{hkl}\, cos\, \theta = \frac{K_B\lambda}{D_{hkl}} + 4\sigma \frac{sin\, \theta}{Y_{hkl}} \tag{II.11}$$

II.2.1.3 Preferred orientation

The crystallographic orientation in the nanostructured thin films is not always random and shows some preferred crystallographic orientations. Thus, a strong tendency for the crystallites to be oriented along a particular crystallographic direction is known as preferred orientation. Nanostructured thin films, grown on different substrates, tend to follow the crystallographic orientation of the substrate and thus, may get oriented. The intensities of the XRD peak in the preferred crystallographic orientation should be high as compared to other XRD peaks. In the partially preferred oriented thin film samples, some other XRD peaks may also be appear with relatively higher intensities. The texture coefficient (c) is used to calculate

the preferred orientation parameter by the method proposed by Harris et al. [109]. Later many other researchers are also used the texture coefficient value to find out the orientation parameter for thin films sample. Texture coefficient TC (c) for the thin films can be determined as follows:

$$\boldsymbol{TC(\gamma)} = \frac{\frac{\boldsymbol{I_{hkl}}}{\boldsymbol{I_{0hkl}}}}{\frac{\mathbf{1}}{\boldsymbol{N}}\sum_{\mathbf{1}}^{\boldsymbol{N}}\frac{\boldsymbol{I_{hkl}}}{\boldsymbol{I_{0hkl}}}} \quad \text{(II.11)}$$

where I_{hkl} is the intensity measured from XRD pattern and I_{ohkl} is standard intensity taken from ICDD data card for a particular (hkl) planes, and *N* is the number of diffraction peaks [104].

II.2.1.4. Used equipment

In our work, we used a Rigaku-SmartLab type diffractmeter with θ-2θ geometry by the facility of IBTIKAR platform (Figure II.2). The X-rays were generated using a Cu$K_{\alpha 1}$ radiation source which emitted X-rays with a wavelength of 1.54056 Å. The samples were analyzed under grazing incidence. The system feature a high-flux 9 kW rotating anode X-Ray coupled with a 2D detector. The system incorporates a five axis goniometer with an in-plane diffraction arm. In our experiments, the scanning range of the detector is chosen from 20 to 60° (Bragg angle).

Figure II.2. Rigaku-SmartLab type diffractmeter.

After recording diffractograms, they were confronted to the ZnO JCPDS data sheet (Figure II.3) from the International Centre for Diffraction Data (ICDD) in order to identify the nature of our deposited films by comparing the XRD peaks positions (or Diffraction angles).

PDF # 361451, Wavelength = 1.540598 (A)

36-1451 Quality: *
CAS Number: 1314-13-2
Molecular Weight: 81.38
Volume[CD] 47.62
Dx: 5.675 Dm:
Sys: Hexagonal
Lattice: Primitive
S.G.: P63mc (186)
Cell Parameters:
a 3.249 b c 5.206
SS/FOM: F27=131(.0071, 29)
I/Icor:
Rad: CuKa1
Lambda: 1.5405981
Filter: Graph
d-sp: diffractometer
Mineral Name:
Zincite, syn
Also called:
chinese white
zinc white

Zn O
Zinc Oxide
Ref: McMurdie, H et al., Powder Diffraction, 1, 76 (1986)

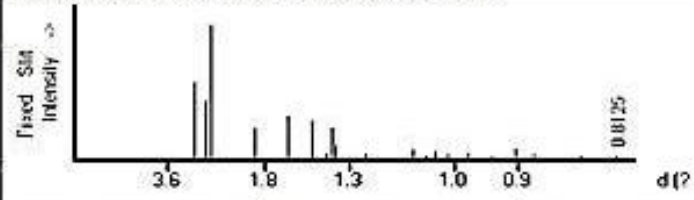

d(A)	Int-f	h	k	l	d(A)	Int-f	h	k	l	d(A)	Int-f	h	k	l
2.8143	57	1	0	0	1.3017	2	0	0	4	.95560	1	2	0	4
2.6033	44	0	0	2	1.2380	4	2	0	2	.93812	3	3	0	0
2.4759	100	1	0	1	1.1816	1	1	0	4	.90694	8	2	1	3
1.9111	23	1	0	2	1.0931	7	2	0	3	.88255	4	3	0	2
1.6247	32	1	1	0	1.0638	3	2	1	0	.86768	1	0	0	6
1.4771	29	1	0	3	1.0422	6	2	1	1	.83703	3	2	0	5
1.4071	4	2	0	0	1.0159	4	1	1	4	.82928	1	1	0	6
1.3781	23	1	1	2	.98464	2	2	1	2	.82369	2	2	1	4
1.3582	11	2	0	1	.97663	5	1	0	5	.81246	3	2	2	0

Figure II.3. JCPDS data sheet of ZnO.

II.2.2. Raman Spectroscopy

Raman spectroscopy is a non-destructive analytical method based on light–matter interactions [110], is a fundamental aspect of materials research. Originally developed by C. V. Raman in 1928, this remarkable technique is developed from the essential principle of Raman effect, which describes the inelastic scattering of light. For monochromatic light, usually from a laser source, interacts with a sample, most of the photons are elastically scattered and maintain their energy and wavelength [111]. Raman spectroscopy provides a wide range of information. It can be used to characterize short-, medium- and long-range structural order, as well as a compound bond type and crystal structure. Its performance is particularly remarkable.

II.2.2.1. Principle

The principle of Raman spectroscopy is the illumination of a material with monochromatic light (laser) in the visible spectral range followed by the interaction of the incident photons with the molecular vibrations or crystal phonons which induces a slight shift in the wavelength of the scattered photons. Scattering can occur with a change in vibrational, rotational or electronic energy of a molecule. If the scattering is elastic and the incident photons have the same energy as the scattered photons, the process is called Rayleigh scattering and this is the dominant scattering interaction. If the scattering is inelastic (the scattered photons have a different energy to the incident photons) the process is called Raman scattering and the scattered photons exhibit a shift in energy called the Raman shift [112], In Raman scattering, an incident photon with energy E_0 interacts with a molecule, leading to the temporary absorption of the photon and the simultaneous emission of a new photon. If the

emitted photon has lower energy, the molecule absorbs the energy difference and transitions to a higher vibrational state, known as Stokes scattering. On the other hand, assume that the molecule is already in a vibrational state of excitement, by going through the same process it will be interesting to find that anti-Stokes scattering, in which the molecule returns to a lower energy state, can occur when it transfers energy to the scattered photon, increasing its frequency.

In other words, monochromatic laser light with frequency ν_o interacts more or less with the oscillating dipoles. And the magnitude of these interactions is related to the degree of polarizability associated with those oscillations. Such oscillating dipoles cause the interacting photons to be scattered with three different frequencies:

- A molecule with or without Raman-active modes (vibrations) will interact with a photon of frequency ν_o. The excited molecule returns back to the same basic vibrational state and scatters light with the same frequency ν_o as the excitation source (Figure II.4). This type of interaction is elastic Rayleigh scattering.
- A photon with frequency νo interacts with a Raman-active molecule which at the time of interaction is in the basic vibrational state. Part of the photon's energy is transferred to the Raman-active vibration with frequency νm and the resulting frequency of scattered light is reduced to $\nu_o - \Delta\nu$ (Figure II.4). This Raman frequency is called Stokes frequency, or just "Stokes"
- A photon with frequency νo interacts with a Raman-active molecule, which, at the time of interaction, is already in the excited vibrational state. Excessive energy of the excited Raman-active mode is transferred to photon energy, the molecule returns to the basic vibrational state and the resulting frequency of scattered light goes up to $\nu_o - \Delta\nu$ (Figure II.4). This Raman frequency is called "Anti-Stokes" [112].

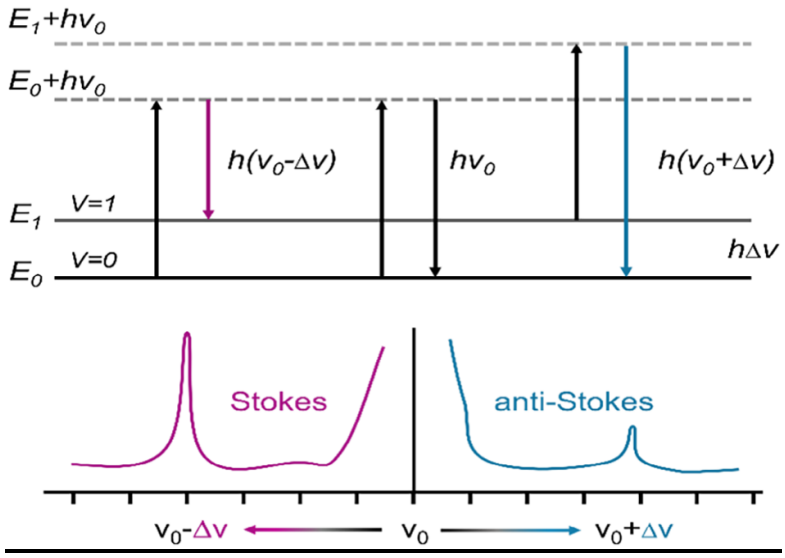

Figure II.4. A schematic representation of Rayleigh and Raman scattering processes [113].

A typical Raman spectrum of bulk ZnO is presented in figure II.5. The difference between the scattered and incident light can be used to identify the sample in terms of the characteristic vibrational modes. Raman peaks of ZnO and the corresponding vibration modes are listed in Table II.1

Table II.1. ZnO optical vibration modes and their corresponding Raman shift [112].

Optical phonon modes	**Raman shift (cm^{-1})**
E2(low)	99
A1(TO)	378
E1(TO)	410
E2(high)	438
A1(LO)	574
E1(LO)	590
E2(high)-E2(low)	330

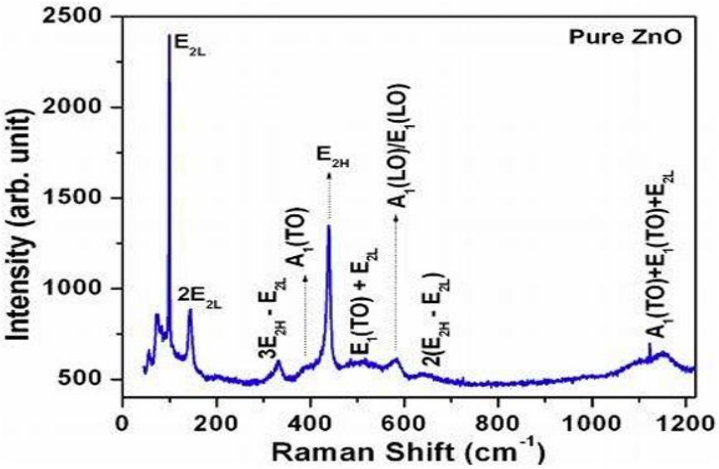

Figure II.5. Micro Raman spectra of pure ZnO nanoparticles for 0.05 M zinc precursor [112].

II.2.2.2. Used equipment

Raman measurements were performed, IPCMS (for: Institut de la Physique et de la Chimie des Materiaux de Strasbourg) in Strasbourg-France, using a Raman spectroscopy measurements were performed in a Horiba microRaman Microscope system (Figure II.6) employing the 632 nm excitation line. Raman spectra of the deposited samples were recorded in the wavenumber range 200–900 cm^{-1}.

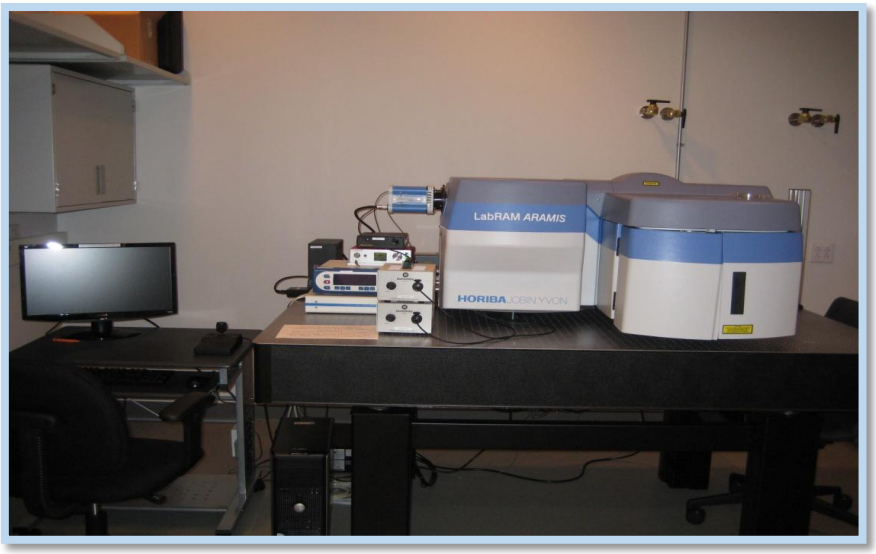

Figure II.6. Image of Horiba microRaman Microscope.

II.2.3. Fourier Transform Infrared Spectrometry

Fourier Transform Infrared Spectroscopy (FTIR) using attenuated total reflection (ATR) is an analytical technique used to identify organic (and in some cases inorganic) materials. This technique measures the absorption of infrared radiation by the sample material versus frequency. The infrared absorption bands identify molecular components and structures. When a material is irradiated with infrared radiation, absorbed IR radiation usually excites molecules into a higher vibrational state. The wavelength of light absorbed by a particular molecule is a function of the energy difference between the at-rest and excited vibrational states. The frequencies that are absorbed by the sample are characteristic of its molecular structure [114].

II.2.3.1. Principle

The principles of IR spectroscopy are like the principles spectroscopic techniques as VIS/UV spectroscopy. The transitions of valence electrons are not induced by the energy of infrared light because it is insufficient but these radiations can be excited to vibrational and rotational motions in molecules [115].

The infrared beam is directed towards the Michelson interferometer, which modulates each beam wavelength at a different frequency (Figure II.7). In the latter, a separator separates the incident light beam in half. These two parts will reflect on mirrors, one fixed and the other mobile. When the two beams recombine, destructive or constructive interference appears depending on the position of the moving mirror.

The modulated beam is then reflected from the two mirrors to the sample, where absorptions occur. The beam then arrives on the detector to be transformed into an electrical

signal [115]. The measured interferogram signal cannot be interpreted directly. A means of "decoding" the individual frequencies is required. This can be accomplished via a well-known mathematical technique called the Fourier transformation. This transformation is performed by the computer which then presents the user with the desired spectral information for analysis [115].

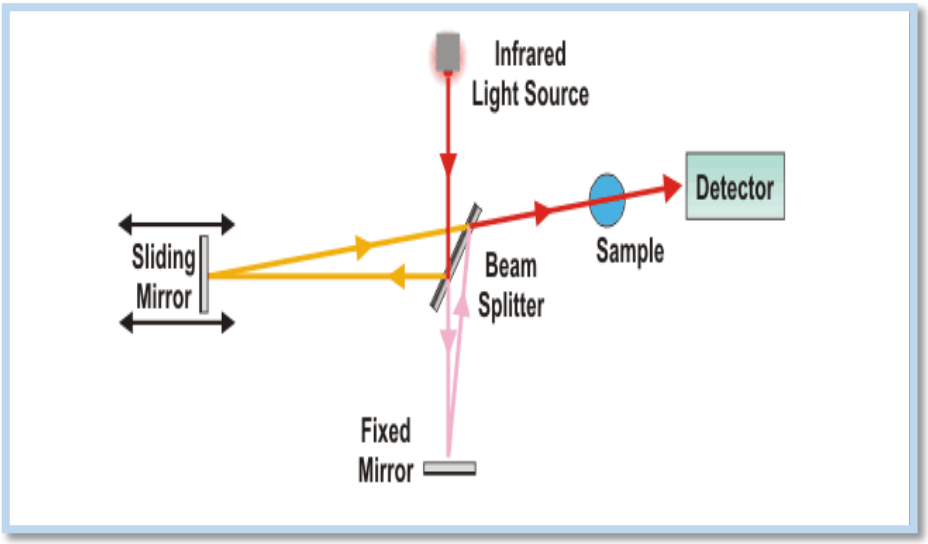

Figure II.7. Principle of infrared spectroscopy [115].

The information drawn from a FTIR spectrum are of two types:

- Qualitative information: The frequencies in which the sample absorbs are characteristics of the chemical groups presented in the analyzed material.
- Quantitative information: The intensity of absorption at the characteristic frequency is related to the concentration of the chemical group responsible for absorption by measuring the area of the characteristic signal, it is possible to estimate the chemical group concentration [115].

II.2.3.2. Used equipment

The FTIR spectra were recorded, in department of chemistry in Yildiz Technical University (Istanbul, Turkey), using a Perkin Elmer spectrometer in the range of 1300- 560 cm^{-1} with a resolution of 2 cm^{-1}. An image of this apparatus is presented in figure II.8.

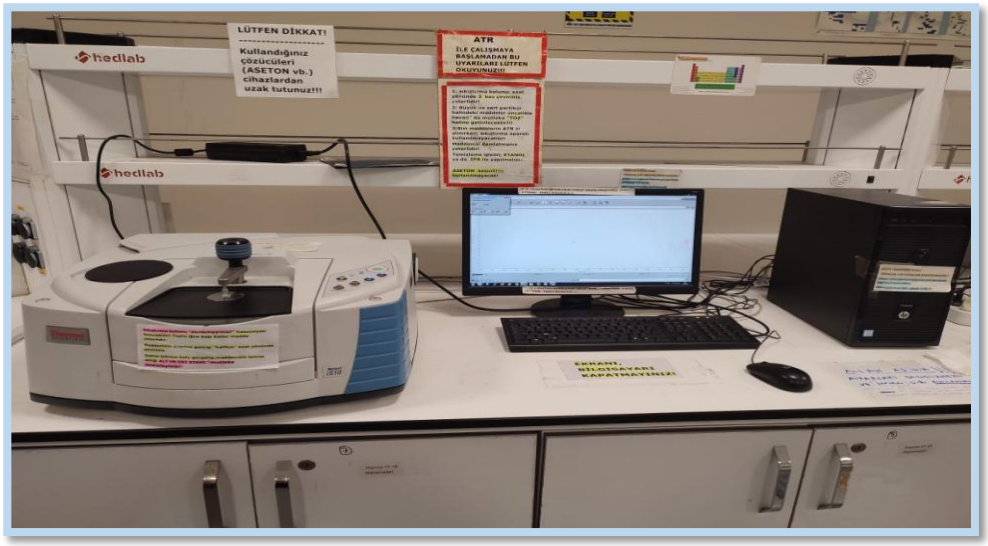

Figure II.8. Image of the used FTIR Spectrophotometer.

II.2.4. UV- visible spectroscopy

UV-visible spectroscopy is a non-destructive optical analysis technique that enables the measurement of the optical transmittance of a material, to measure the absorption, and to determine the band gap energy (Eg) of a thin film. It involves photons with wavelengths in the ultraviolet (200-400 nm), visible (400-800 nm), and near-infrared (800-1400 nm) ranges, which is based on the transition of electrons, atoms, or molecules from the ground state to the excited state via the excitation of electromagnetic waves [116].

II.2.4.1. Principle

UV-visible spectroscopy is based on the interaction between light and matter. It involves techniques such as single-beam and double-beam spectrophotometries and finds applications in the quantitative and qualitative analysis of compounds, monitoring reaction kinetics, and material characterization [116].

In particular, double-beam UV-visible spectrophotometers (Figure II.9) are simultaneous instruments that are typically faster, enable more precise analysis, and are more effective.

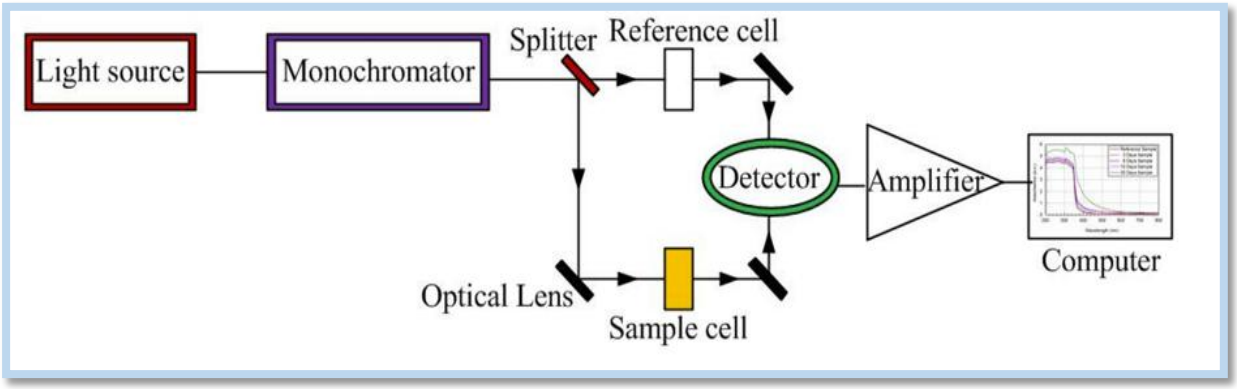

Figure II.9. Schematic diagram for the experimental setup of a double-beam UV-Vis spectrophotometer [118].

The operation of a double-beam spectrometer begins with the emission of light from the light source, which passes through the monochromator where the desired wavelength is selected. The monochromatic light is then split into two beams by the beam splitter. One beam passes through the sample, and the other passes through the reference. Both the sample and reference beams are directed towards their respective detectors. The sample beam passes through the sample in the cuvette, where part of the light is absorbed based on the sample's properties and concentration. The reference beam passes through the reference holder. The

detectors measure the intensities of both the sample and reference beams. The readout device processes the electrical signals from the detectors, comparing the intensities of the sample and reference beams. This comparison compensates for any fluctuations in the light source intensity and other environmental factors, providing accurate and stable measurements of absorbance or transmittance [117].

II.2.4.2. Optical constants determination

II.2.4.2.1 Absorption coefficient

The electronic transitions between the conduction band CB and the valence band VB in the materials begin at the absorption edge because it corresponds to the least energy variation between the highest maximum of the VB and the lowest minimum of the CB. The optical absorption of the materials and their coefficient of absorption, α, are directly related. Determining the absorption properties of glasses and thin films is essential, particularly when it comes to the optical material properties that are being explored for potential applications. Some of the energy of light that strikes thin films is reflected, some is absorbed, and the remainder is transmitted [117].

From the transmittance T of a d thickness film, one can calculate the absorption coefficient α of the material which constitutes it, using the Bouguer Lambert-Beer relation or often simply called; the law of Beer given by:

$$T = e^{-\alpha d} \tag{II.12}$$

If one expresses the transmittance T, in (%), the absorption coefficient will be given by :

$$\alpha = \frac{1}{d} ln\left(\frac{100}{T(\%)}\right) \tag{II.13}$$

Swanepoel model [119] is without a doubt the most well-known method to calculate the optical parameters such as dielectric constant and refractive index. The films thickness can be determined using the envelope method which explore the multiple reflections of light (interference fringes) occur between the lower surface in contact with the substrate and the free surface of the film.

II.2.4.2.2 Band gap energy

Several methods can be used to determine the energy gap of a semiconductor, depending on whether it is in the form of a thin film. The absorption spectrum of a sample is usually recorded in transmission mode. The optical band gap E_g for direct allowed transitions is determined by applying the Tauc model in the high-absorption region [120] given by:

$$(\alpha h\nu)^2 = A(h\nu - E_g) \quad \text{(II.14)}$$

where h is Planck's constant, ν is the frequency of the incident photons, α is the absorption coefficient and A is a constant which depends on the electron-hole mobility. By extrapolating the curve to the energy axis (Figure II.10), the optical band gap E_g can be derived from the square curve of the product of the absorption coefficient and the photon energy ($\alpha h\upsilon$) as a function of the photon energy.

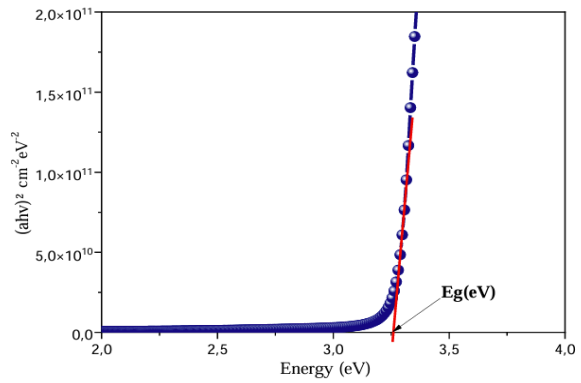

Figure II.10. Tauc plot for the determination of E_g..

When we extend the linear part of $(\alpha hv)^2$ up to the x-axis (i.e. $(\alpha hv)^2 = 0$), we obtain the value of E_g.

II.2.4.3. Used equipment

The transmittance spectra of the deposits films were recorded in the Laboratory on the Physico-Chemistry of Surfaces and Interfaces (LRPCSI) of the University of Skikda, using a Shimatzu 1700 double-beam UV-visible spectrophotometer (Figure II.11) in the wavelength range 300-900 nm.

Figure II.11. Image of a Shimatzu 1700 double-beam UV-Vis spectrophotometer.

II.2.5. Photoluminescence spectroscopy

Photoluminescence characterization is a nondestructive, a nonintrusive, a versatile and a sensitive technique to the presence of defects or impurities in materials. There have been many kinds of luminescence measurements. This method uses as an excitation source light, typically laser or monochromatic beam. The photoluminescence phenomena is a result of

incident-photon absorption that generates electron-hole pairs and produces emission of a photon of a different wavelength. The generated electron and hole tend to return to their ground state by giving up the excess energy through recombination. Before recombination, the generated carriers (electrons and holes) experience various processes such as diffusion, drift, scattering, exciton formation, and so on (Figure II.12). If the generated carriers give up their energy in the form of light, the recombination is called radiative recombination (Figure II.12). Otherwise, if the generated carriers lose the excess energy in the form of heat, the process is called nonradiative recombination. Luminescence measurement investigates radiative recombination in materials. This emitted light is detected as photoluminescence, and the spectral dependence of its intensity provides information about the properties of the material [121].

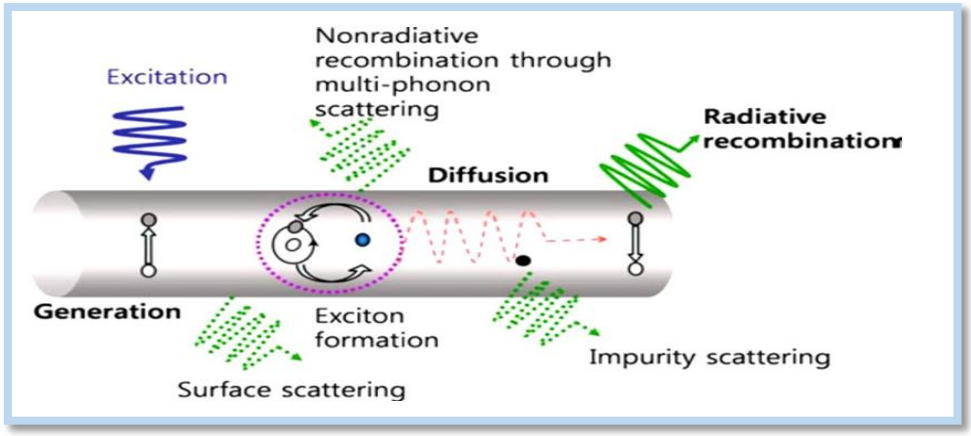

Figure II.12. Optical processes in a semiconductor nanostructure [121].

II.2.5.1. Principle

The laser source launched a laser beam toward the optical mirror that directed the beam to the sample (Figure II.13). When the laser beam hit the sample, some electrons were excited to higher energy levels. Then, these electrons returned to their ground energy level

emitting radiation, which was detected by the PL spectrometer at specific wavelengths that reflected the energy difference between the energy levels. The PL spectrometer was used to separate the emitted light into its component wavelengths, and then to record the emission spectra intensity of the sample as a function of wavelength [121].

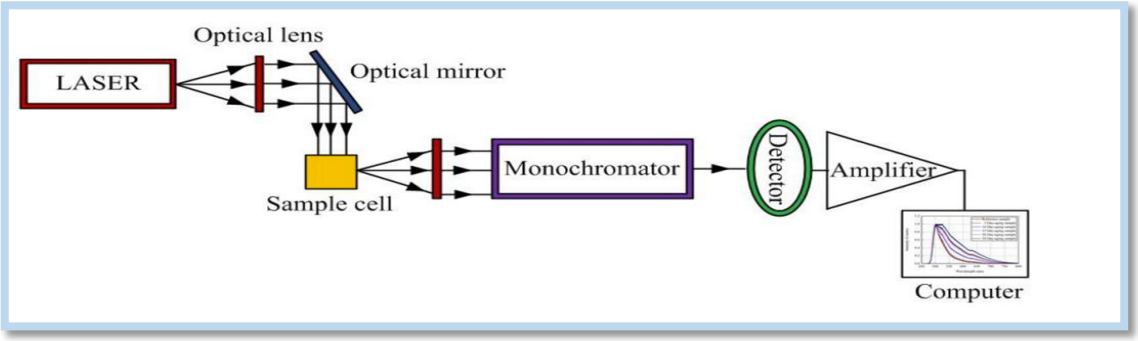

Figure II.13. Schematic representation of photoluminescence principle [121].

II.2.5.2. Used equipment

PL spectra of samples were recorded, in IPCMS (Institut de la Physique et de la Chimie des Materiaux de Strasbourg), at room temperature using a frequency-tripled Nd-YAG laser photometer under an excitation wavelength λ=335 nm and the emission spectra was recorded at the wave length range of 300- 900 nm.

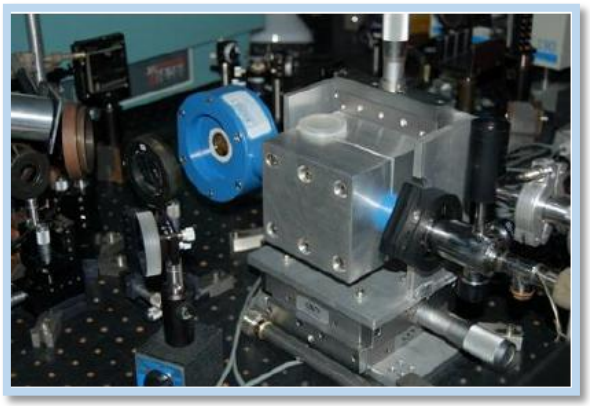

Figure II.14. Photoluminescence measurement setup.

Chapter III

Experimental results and discussion

III.1. Characterization results of ZnCoO thin films

In this part, experimental results of the characterization of ZnCoO thin films by X-rays diffraction, Raman spectroscopy, ATR-FTIR spectroscopy, UV-visible spectroscopy, and photoluminescence spectroscopy will be presented and discussed as a function of Co molar ratio x (Eq. II.1).

The whole of results was published in **Micro and nanostructures.** This journal is listed in category "A" according to the DGRSDT scientific journals ranking. This paper can be cited as:

R. Nettour, A. Kabir, A. Erdoğmuş, Ö. D. Kutlu, G. Schmerber
Structural, optical and luminescence characterization of Co-doped ZnO thin films
Micro and nanostructures
207 (2025) 208271

III.1.1. X-rays diffraction

X-rays diffraction patterns of films deposited by spraying mixtures, corresponding to Co molar ratios varied from x=0.00 to x=0.10, onto heated glass substrates are presented in Figure III.1-a. Except for the pattern corresponding to x=0.10, we can see the presence of five diffraction peaks in the remaining patterns. According to the JCPDS# 36-1451 data sheet, these peaks, located around 31.83°, 34.56°, 36.36°, 47.68° and 56.67° are attributed respectively to (100), (002), (101), (102), and (110) orientations of the hexagonal wurtzite structure of ZnO. We can see that all samples have the same preferential orientation along to (002) planes.

For Co molar ratio x=0.10, we can see the disappearance of (100) and (110) corresponding peaks and the appearance of weak peaks corresponding to $Zn(OH)_2$ and Co_3O_4 phases

according to the data sheets JCPDS#41-1359 and JCPDS#43-1003 respectively. The Co_3O_4 secondary phase was also obtained by other researchers like Ivill et al. [122] and Sundararaj et al. [123]. They found that the increase of the Co ratio reduced gradually the crystalline quality of ZnO before the appearance of the Co_3O_4 secondary phase.

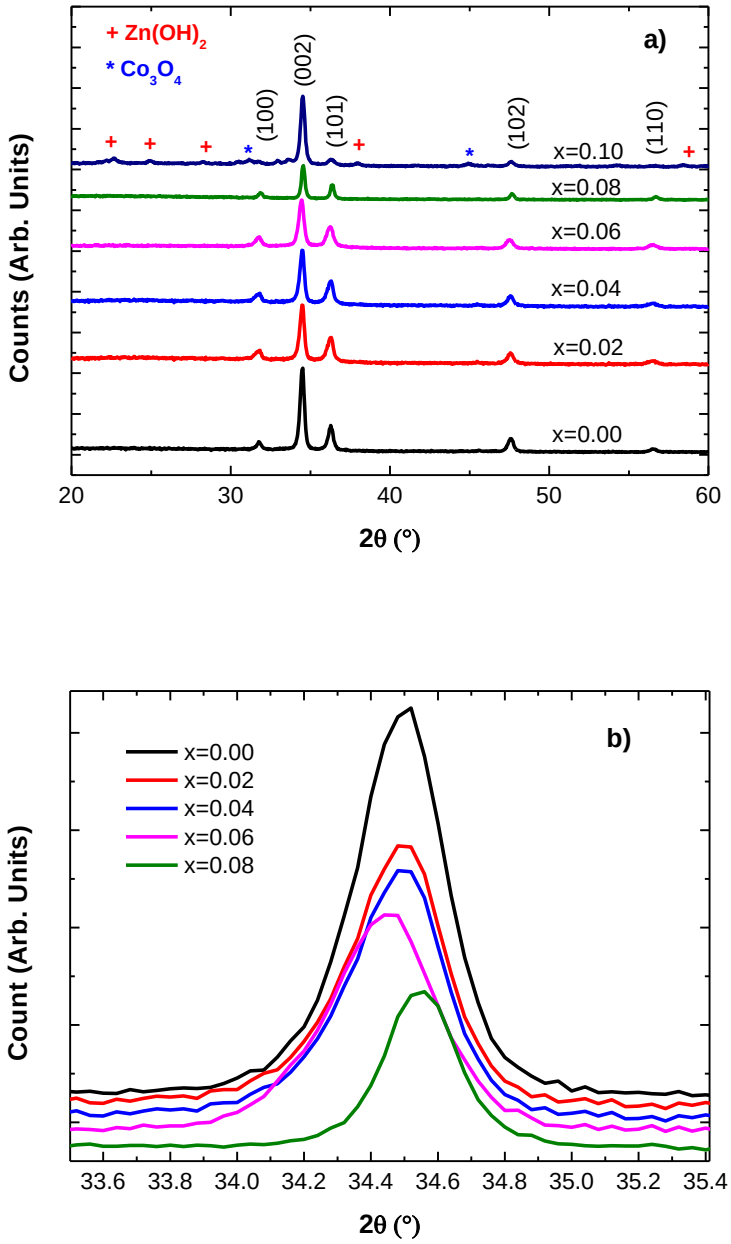

Figure III.1: a) XRD patterns of ZnO films as a function of Co molar ratio. b) Zoom of the (002) diffraction peak.

The decrease of the (002) peak intensity, with the increase of Co molar ratio from x=0.00 to x=0.08, observed in Figure 1-b is in good agreement with their results. The decrease of XRD peaks, for Co molar ratios from x=0.02 to x=0.08, and the simultaneous appearance of Co_3O_4 and $Zn(OH)_2$ secondary phases, for Co molar ratio x=0.10, indicates that the progressive inclusion of Co also slowed down the reaction of the formation of ZnO phase.

The shift of the (002) diffraction peak (Figure 1-b) confirms the substitution of Co ions into the ZnO host lattice. The substitution of Co ions into ZnO host may induce lattice distortion regarding the difference between the ionic radius of Zn^{2+} (0.06 nm) and Co^{2+} (0.058 nm) [124, 125]. In figure III.2, is traced the variation of the lattice parameters a and c, determined using eq. II.3, as a function of Co molar ratio x. We can see that the lattice parameters values a=3.251 Å and c=5.204 Å of the sample elaborated without Co inclusion (i.e. x=0.00) are quite different from those of the bulk ZnO a_0=3.249 Å and c_0=5.206 Å. This difference may be due to residual stress induced by the substrate temperature and/or the substrate nature [126].

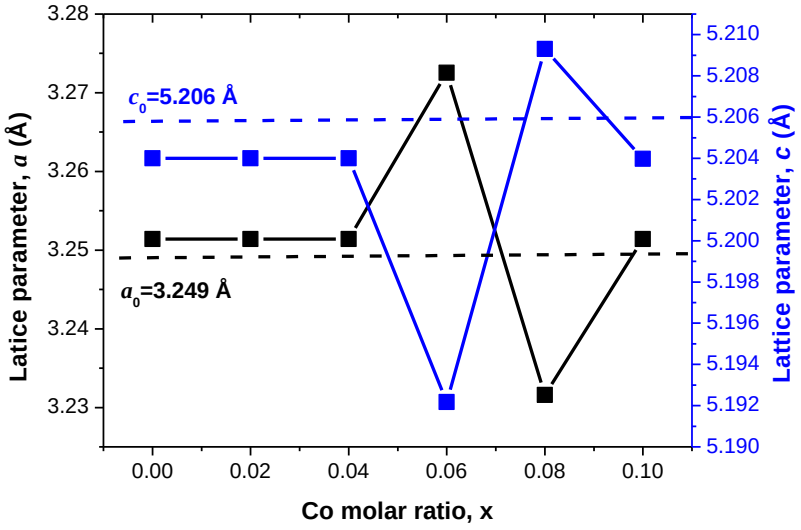

Figure III.2: Variation of lattice parameters as a function Co molar ratio.

One can see, in figure III.2, that Co inclusion in ZnO films with Co molar ratios x=0.02 and x=0.04 has no effect on lattice parameters and consequently, no effect on the directional strain. The Co inclusion takes effect from x=0.06 where both parameters a and c vary alternatively, as a function of Co molar ratio, between 3.273 and 3.232 Å for a parameter and between 5.192 and 5.209 Å for c parameter. This significant difference between these values and those of the sample corresponding to x=0.00 suggests, according to Yildiz et al. [127], that substitution is not the only mechanism for Co inclusion in ZnO despite the convergence between ionic radii of Zn^{2+} and Co^{2+}. Co ions may also occupy interstitial sites in hexagonal ZnO. According to Arefi-Rad and Kafachan [128], the change of the sign of the directional strain ($\Delta a/a_0$ and $\Delta c/c_0$) for x=0.06 and x=0.08 may be due to asymmetric distortions along particular crystallographic directions caused by the inclusion of the Co ions in the ZnO host lattice. For x=0.10, both parameters a and c reach values of the sample deposited without Co inclusion (i.e. x=0.00) indicating stress relaxation. The stress relaxation phenomenon arose simultaneously with the appearance of $Zn(OH)_2$ and Co_3O_4 secondary phases.

For more accuracy in measuring the crystallite size regarding the faced difficulty of the attribution of the XRD peak broadening to the crystallite size or to the microstrain, we have used, in addition to Debye Scherrer method (Eq. II.6) which determine the crystallite size D from the dominant XRD peak, two other methods for crystallite size calculation: the Monshi-Scherrer (M-S) method (Eq. II.7) and the Williamson-Hall (W-H) method (Eq. II.9). These two methods are based on determining the crystallite size D from the diffraction angle $\theta_{(hkl)}$ and the FWHM $\beta_{(hkl)}$ of all XDR peaks. For the Monshi-Scherrer method [129], the crystallite size D_{M-S} is determined from a linear fit of the variation of $\ln\beta_{(hkl)}$ as a function of $-\ln\cos\theta_{(hkl)}$ (Figure III.3).

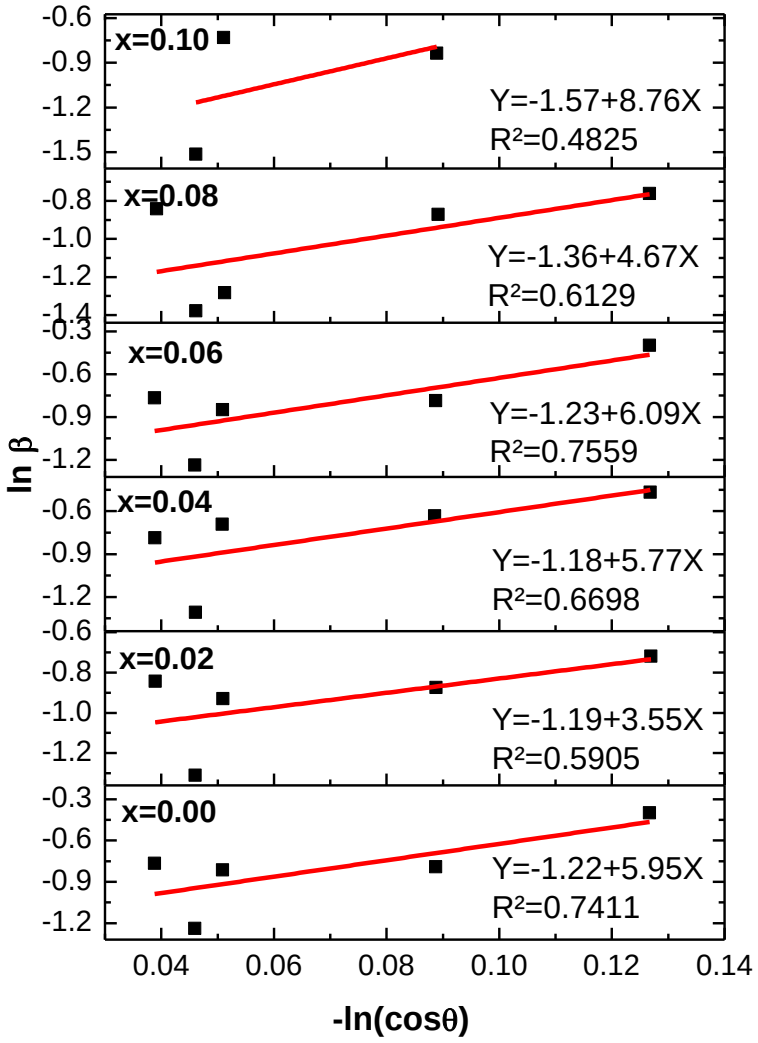

Figure III.3: Monshi-Scherrer plots for all samples (Red lines are the linear fit).

For the Williamson-Hall method [130], the crystallite size D_{W-H} is determined from a linear fit of the variation of $\beta_{(hkl)}\cos\theta_{(hkl)}$ as a function of $4\sin\theta_{(hkl)}$ (Figure III.5). Resulting crystallite sizes D_{D-S}, D_{M-S}, and D_{W-H} calculated for all Co molar ratios are regrouped in table III.1. We can see, in table III.1, that the obtained crystallite sizes using D-S, M-S, and W-H methods show the same trend. They decreased, for x=0.02 and x=0.04 and start increasing from x=0.06 to reach their highest values for x=0.10. We can see also that values of D_{D-S} and

D_{M-S} are close and less than that of D_{W-H} which is in good agreement with results in [128, 131, 132].

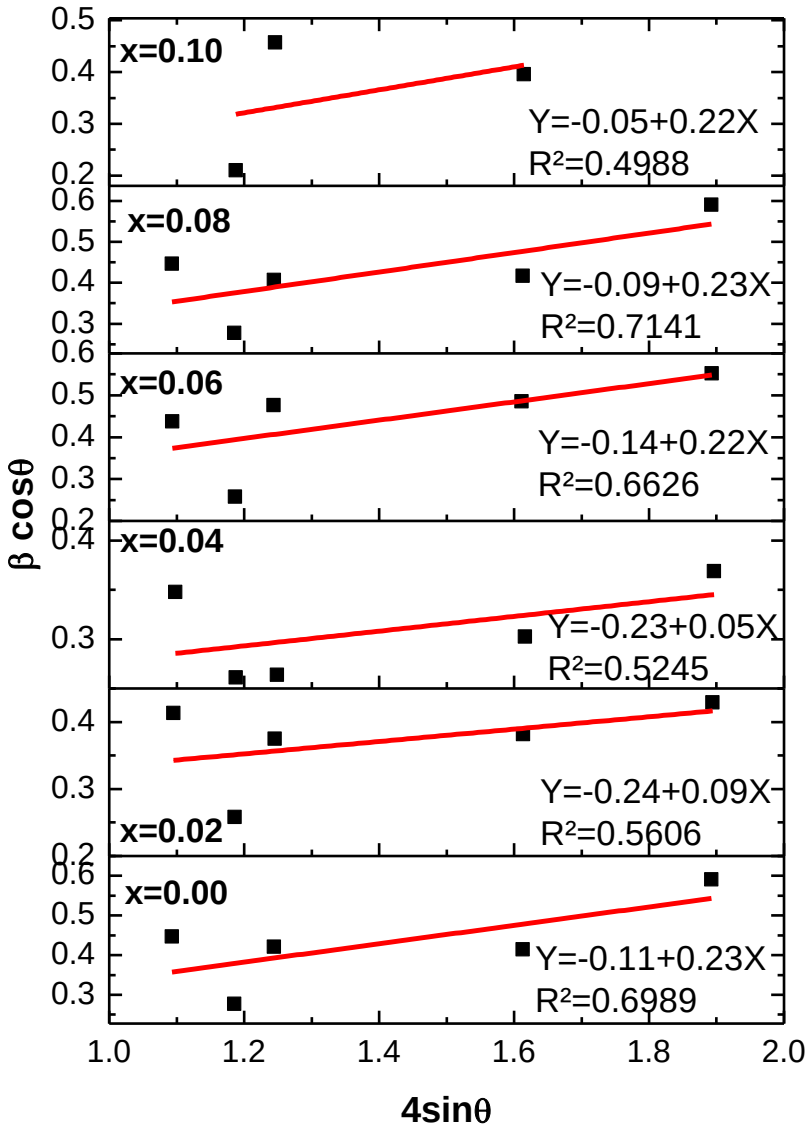

Figure III.4: Williamson-Hall plots for all samples (Red lines are the linear fit).

According to [128], D_{W-H} values of Mn-doped SnS nanoparticules are comparable to the crystallite size measured using TEM and this indicates that the W-H method is more

accurate compared with the other two methods due to the fact that it does not neglect the effect of microstarin.

Table III.1: Crystallite size of the elaborated samples calculated using the Debye-Scherrer method $D_{D\text{-}S}$, the Monshi-Scherrer method $D_{M\text{-}S}$, and the Williamson-Hall method $D_{W\text{-}H}$.

Co molar ratio	$D_{D\text{-}S}$ [nm]	$D_{M\text{-}S}$ [nm]	$D_{W\text{-}H}$ [nm]
0.00	20.2	26.9	72.2
0.02	28.7	26	33.1
0.04	28.7	25.9	39.7
0.06	31.0	27.3	56.7
0.08	33.0	30.9	88.3
0.10	37.2	38.2	158.9

In figure III.5, the variation of the crystallite size $D_{W\text{-}H}$ is traced with the (002) peak intensity $I_{(002)}$ as a function of Co molar ratio. For x=0.00, the $D_{W\text{-}H}$ value (72.2 nm) is in good agreement with those in [133]. One can see, in figure III.5, a rapid decrease of $D_{W\text{-}H}$ for x=0.02 (33.1 nm) accompanied by a rapid decrease of $I_{(002)}$. If we consider a correlation between an XRD peak intensity and the crystallite number, the rapid decrease of $I_{(002)}$, for x=0.02, indicates that Co inclusion in ZnO influences the crystallites number and the crystallite size differently and this is confirmed by the other experimental points. We can also see in figure III.5 that, from x=0.04, $I_{(002)}$ continue decreasing while $D_{W\text{-}H}$ starts growing from 39.7 nm to reach 88.3 nm for x=0.08. For x=0.10, the increase of $D_{W\text{-}H}$ (158.9 nm) is accompanied by an increase of $I_{(002)}$ which reached a value less than that for x=0.00 (Figure III.5). This increase coincides with the formation of $Zn(OH)_2$ and Co_3O_4 secondary phases. The increase of $I_{(002)}$ and $D_{(002)}$, even for x=0.10, is accompanied with a pronounced decrease of (101) and (102) peaks intensity and a complete disappearance of (100) and (110) peaks (Figure 1). This may be related to stress induced by the inclusion of Co ions in ZnO. This

grain growth phenomenon was also found by Schoeppner et al. [134] in Au-doped ZnO. They attribute the grain growth induced by stress to grain rotation, grain boundary sliding, and diffusion according to previous studies on other materials [135-138].

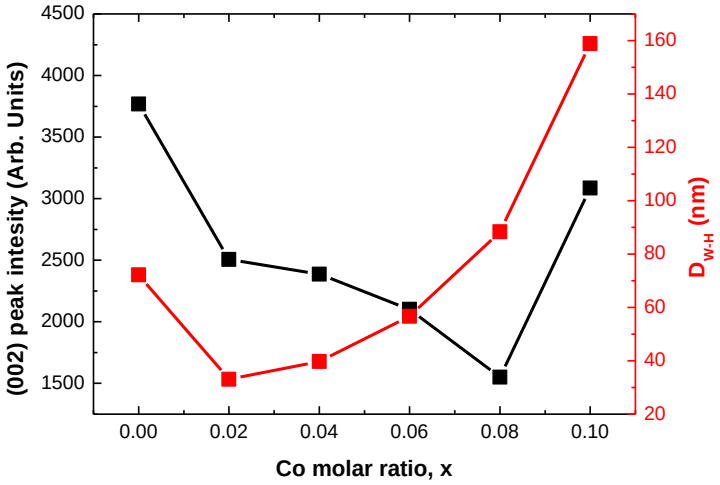

Figure III.5: Variation of the W-H crystallite size and the (002) peak intensity as a function of Co molar ratio.

III.1.2. Raman spectroscopy

Raman spectra of the elaborated samples, recorded in the wavenumber range 200-900 cm^{-1}, are presented in figure III.6. According to the group theory, the zone center of optical phonons, in Wurtzite ZnO, is described by $\Gamma = A_1 + E_1 + 2E_2 + 2B_1$ where A_1 and E_1 are polar modes which can be divided to transverse optical component (A_{1T} and E_{1T}) and longitudinal optical component (A_{1L} and E_{1L}), E_2 consists of two modes corresponding to high (E_{2H}) and low (E_{2L}) phonons frequencies and B_1 is a silent mode [139].

We can see, in figure III.6, that Raman spectra shape varies as a function of Co molar ratio. For x=0.00, the presence of four broad peaks can be seen. The first peak, located around

380 cm^{-1}, corresponds to A_{1T} vibration mode of ZnO [140], the second peak, around 450 cm^{-1} corresponds to E_{2H} vibration mode of ZnO [140] and the third peak, located around 580 cm^{-1}, corresponds E_{1L} vibration mode of ZnO [141]. The peak, located around 780 cm^{-1}, may be related to low packing morphology as observed in porous ZnO films [142].

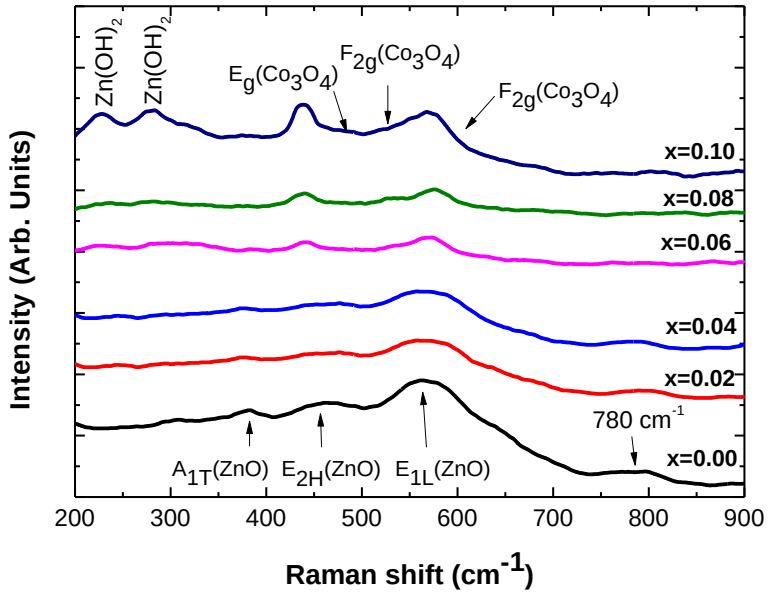

Figure III.6: Raman spectra of ZnO films as a function of Co molar ratio.

When x=0.06, the peak around 780 cm^{-1} disappears simultaneously with the narrowing of the E_{2H} corresponding peak indicating an enhancement of the crystalline structure regarding the increase of the crystallites size (Figure III.5). The invariance of Raman spectra, for x<0.06, compared with that of x=0.00 indicates that there is no effect of Co inclusion on the ZnO crystalline structure in good agreement with results in figures 2 and 3. For x=0.10, we can see the appearance of two peaks around 228 and 278 cm^{-1}. These peaks are attributed to $Zn(OH)_2$ phase [143] in excellent agreement with results in Figure 1-a. The asymmetric of the peak around 580 cm^{-1} may be due to the presence of E_g (488 cm^{-1}) and F_{2g} (522 and 618 cm^{-1}) of Co_3O_4 [144] in addition of the E_{1L} vibration mode of ZnO.

III.1.3. ATR-FTIR spectroscopy

Figure III.7 shows ATR-FTIR spectra of the elaborated samples with different Co molar ratios. These absorption spectra were recorded in ambient air in the wavenumber range between 1300 and 550 cm^{-1}. All spectra have the same shape with quite difference in some regions. They exhibit two asymmetric peaks that may contain, according to literature, a peak around 1150 cm^{-1} attributed to C-O-H [145], a peak around 1060 cm^{-1} attributed to Zn-O-Zn [146], a peak around 890 cm^{-1} attributed to -OH [147], a peak around 875 cm^{-1} attributed to O-C-O [148], a peak around 760 cm^{-1} attributed to Zn-O-H [54], a peak around 700 cm^{-1} attributed to Zn-O-Zn [141] and a peak around 680 cm^{-1} attributed Co-O [149].

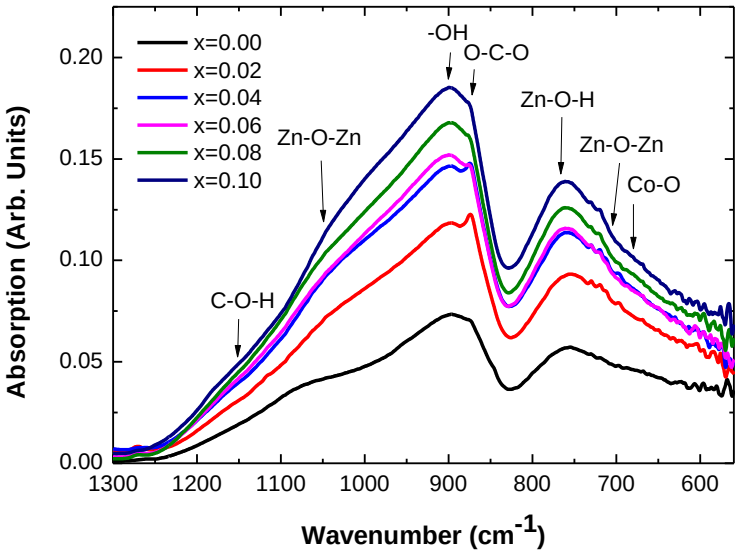

Figure III.7: ATR-FTIR spectra of ZnO films as a function of Co molar ratio.

As can be seen, in figure III.7, the intensity of these two asymmetric absorption peaks increases as a function of Co molar ratio. To study the effect of Co inclusion on these bonds, we have made a deconvolution of each spectrum into 7 Gaussians basing on the above cited

bonds positions. An example of a deconvolution of an ATR-FTIR spectrum into 7 Gaussians is shown, in figure III.8, with a correlation coefficient R^2=0.99918.

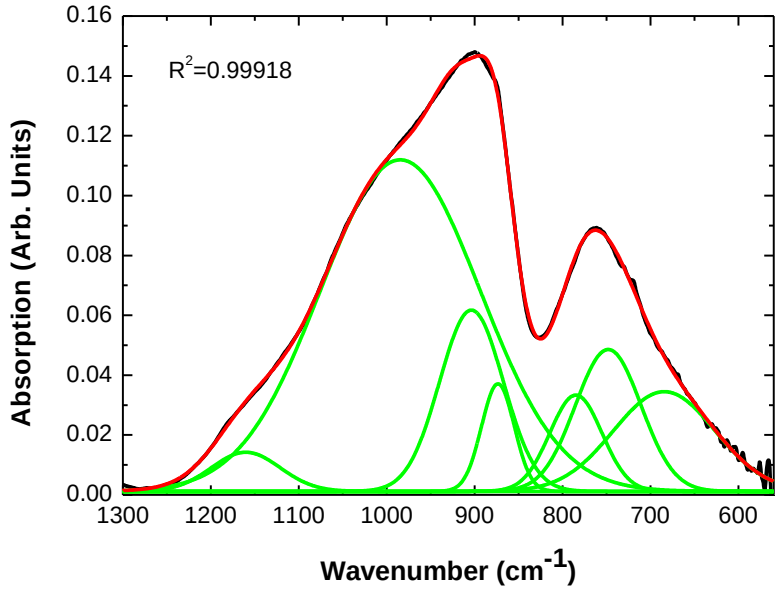

Figure III.8: Example of a deconvolution of a ATR-FTIR spectrum.

In figure III.9-a, is presented Gaussian peaks areas of Zn-O-Zn (1060 cm^{-1}), Zn-O-Zn (700 cm^{-1}), Zn-O-H and Co-O bonds as a function of Co molar ratio. Basing on the fact of the correlation between the absorption peak area and the corresponding bond density, one can evidence the degradation of deposited ZnO after Co inclusion from the decrease of both Zn-O-Zn bonds density as a function of Co molar ratio which is in good agreement with XRD results. This decrease is accompanied by an increase of both Zn-O-H and Co-O bonds density. The increase of Zn-O-H bond density as a function of Co molar ratio x<0.10 may be due to the adsorption of water molecules on ZnO surface. For x=0.10, the significant increase of Zn-O-H bond density may be explained by the formation of $Zn(OH)_2$ secondary phase revealed by Raman spectroscopy and XRD. We can see also the correlation between Co-O bond density and Co molar ratios x<0.10 indicating a good insertion of Co in ZnO matrix. For

x=0.10, the rapid increase of Co-O bond density could be related to the formation of Co_3O_4 secondary phase which correlates with results of XRD.

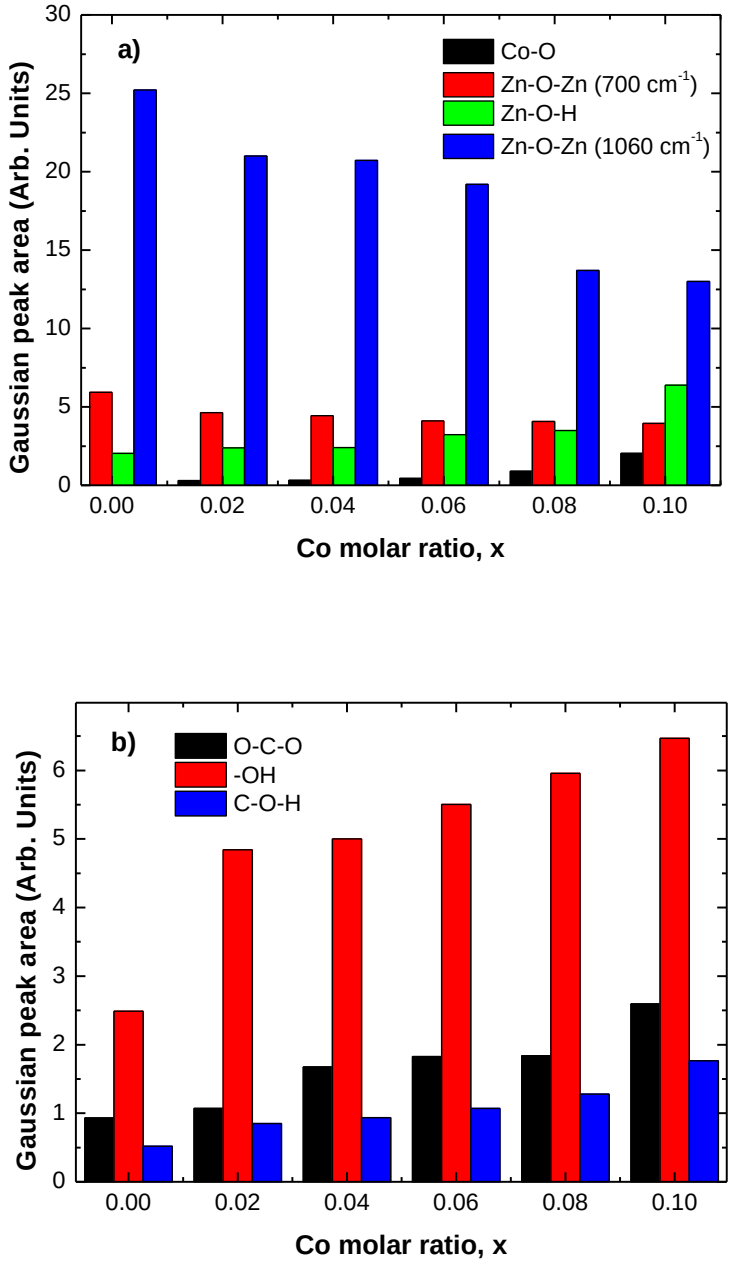

Figure III.9: Variation, as a function of Co molar ratio, of ATR-FTIR Gaussian area corresponding to a) Co-O, Zn-O-Zn (700 cm^{-1}), Zn-O-H and Zn-O-Zn (1060 cm^{-1}) and b) O-C-O, -OH and C-O-H.

In figure III.9-b, is presented the variation of Gaussian peak area of O-C-O, -OH and C-O-H bonds as a function of Co molar ratio. We can see that all bonds density increases as a function of Co molar ratio reflecting the increase of CO_2 and H_2O adsorption on ZnO surface. This indicates that Co inclusion influences also the surface adsorption of ZnO.

III.1.4. UV-visible spectroscopy

Figure III.10 presents UV-Visible spectra, recorded in the wavelength range 300-900 nm, of the deposited films with Co molar ratios from x=0.00 to x=0.10,. One can see that the shape of these spectra varies with the variation of Co molar ratio. For x=0.02 and x=0.04, the shape of UV-Visible spectra looks the same as that for x=0.00. The only difference is the decrease of the transmittance. For x=0.06 and x=0.08, in addition to the decrease of the optical transmittance, one can see weak absorption bands between 550 and 700 nm corresponding to the substitution of Zn ions by Co ions in hexagonal ZnO [150].

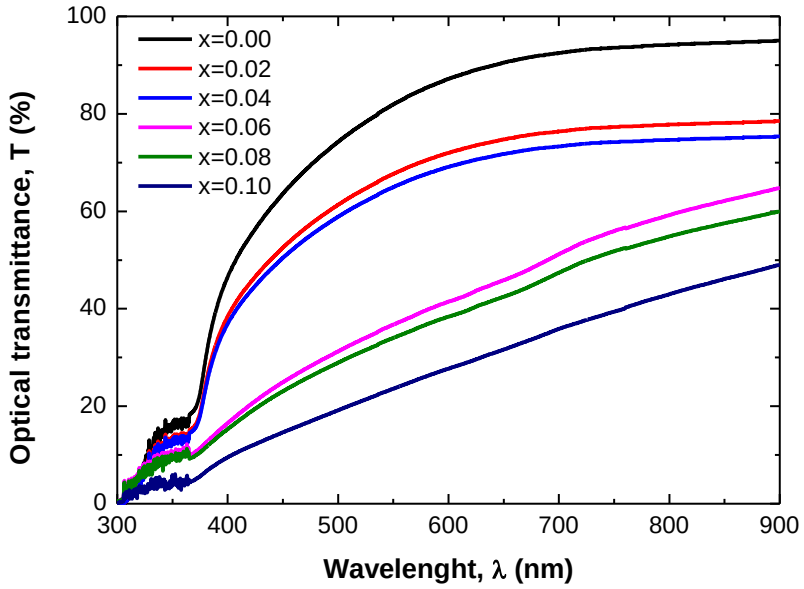

Figure III.10: UV-Visible spectra of ZnO films as a function of Co molar ratio x.

The significant decrease of the optical transmittance with the disappearance of Co corresponding absorption bands, observed for x=0.10, may be interpreted by the formation of Co_3O_4 and $Zn(OH)_2$ secondary phases. The mean transmittance T_m in the visible region between 400 and 800 nm, decreases from 70.33%, for x=0.00, to reach its lowest value of 23.25% for x=0.10 as can be seen in figure III.11. The decrease of the mean transmittance correlates with the increase of crystallite size observed in figure III.5. The inclusion of Co in ZnO increased the absorption of visible light and this may be explained by the increase of the s-d and p-d exchange interactions between electrons band in ZnO and localized d electrons in Co ions [151]. This result is in good agreement with those in [152-154].

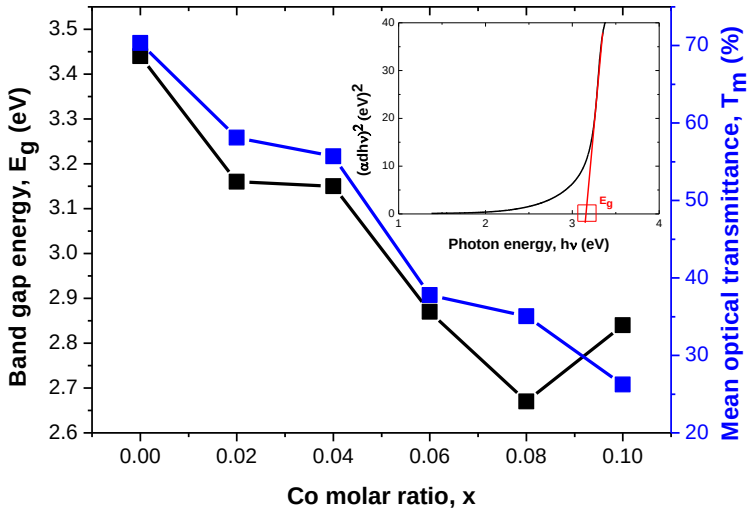

Figure III.11: Variation of the band gap energy and the mean optical transmittance as a function of Co molar ratio (**Inset:** Plot of $(\alpha dh\nu)^2$ vs. hν).

The variation of the band gap energy E_g is also presented in figure III.11 as a function of Co molar ratio. The band gap energy is determined graphically from the extrapolation of the linear part of the curve $(\alpha dh\nu)^2$, as a function of photon energy hν, up to the abscissa

corresponding to $(\alpha dh\nu)^2=0$ (Inset of figure III.11). This curve was traced using the Tauc's law (Eq. II.14). The band gap energy value E_g= 3.45 eV corresponding to x=0.00 (Figure III.11) is greater than that of the bulk ZnO (3.37 eV) however, it is comparable to those of Giri et al. [155] and Slimani et al. [156]. The decrease of the band gap energy E_g to 2.67 eV, for x=0.08, is in good agreement with the results in [152] and [153]. This decrease may be due to sp-d exchange interactions between electrons band in ZnO and localized d electrons in substituted Co ions. According to Biradjar et al. [151], the s-d and p-d exchange interactions would lead to the narrowing of the band gap and would give rise of some corrections of the conduction band and the valence band energies. The increase of the band gap energy for x=0.10 (E_g=2.84 eV) may be interpreted by the decrease of sp-d exchange interactions caused by the formation of Co_3O_4 and $Zn(OH)_2$ secondary phases which is in good agreement with results in [157] and [158].

III.1.5. Photoluminescence spectroscopy

Figure III.12 presents photoluminescence (PL) spectra of ZnO films as a function of Co molar ratio. Except for the spectrum corresponding to x=0.10, all spectra have the same shape with two dominant emission peaks, ultraviolet (UV) emission around 375 nm and near infrared (NIR) emission around 754 nm. The UV emission is generally related to the creation, by photo stimulation, of excitons of energies near the ZnO band edge. A slight red shift could be observed, in figure III.12, in good agreement with UV-visible results. The decrease of this emission peak intensity may be explained by the decrease of the probability of excitons creation due to the reduction of the crystalline quality induced by the inclusion of Co in ZnO [159].

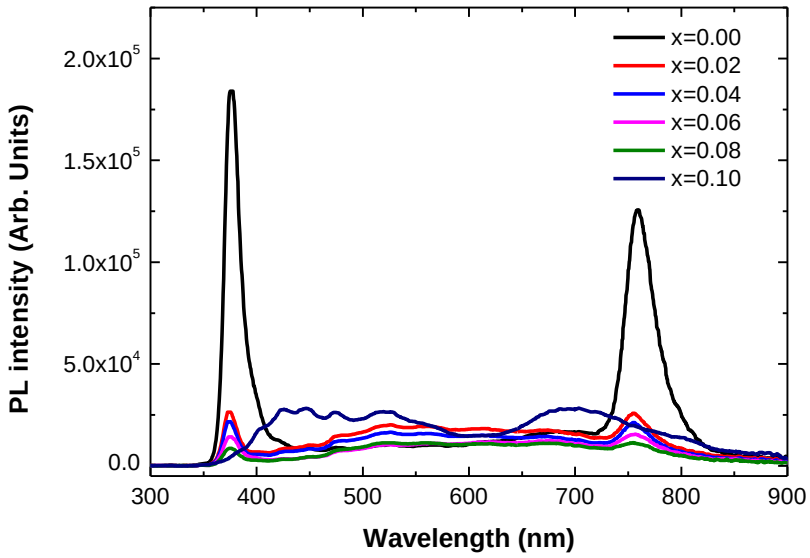

Figure III.12: PL spectra of ZnO films as a function of Co molar ratio x.

One can see, in figure III.13, a correlation between the UV emission peak intensity and Co molar ratio after a sharp decrease (for x=0.02) indicating the efficiency of included Co ions in reducing exitons creation. The NIR emission peak was also found by Wang et al. [160] around 756 nm. They attributed this emission to the donor-acceptor transition between oxygen vacancies V_O and zinc vacancies V_{Zn} and/or the radiative recombination of trapped electrons with trapped holes in oxygen interstitial O_i [160]. The variation of the NIR emission peak intensity as a function of Co molar ratio is also presented in figure III.13. As can be seen, the decrease of the NIR emission is directly related to the increase of included Co ions which decreases native defects in ZnO such as V_O, V_{Zn} and O_i responsible for the NIR emission by donor-acceptor transition and/or by radiative recombination of trapped electrons with trapped holes. For x=0.10 (Figure III.12), a red emission peak appears around 697 nm simultaneously with the disappearance of both UV and NIR emissions. According to Xiao et al. [161], this emission peak is attributed to the d-d radiative transition of Co ions in a

tetrahedral crystal field. The red emission evidences the inclusion of Co in ZnO which could involve Co-based impurities and deep level defects [162].

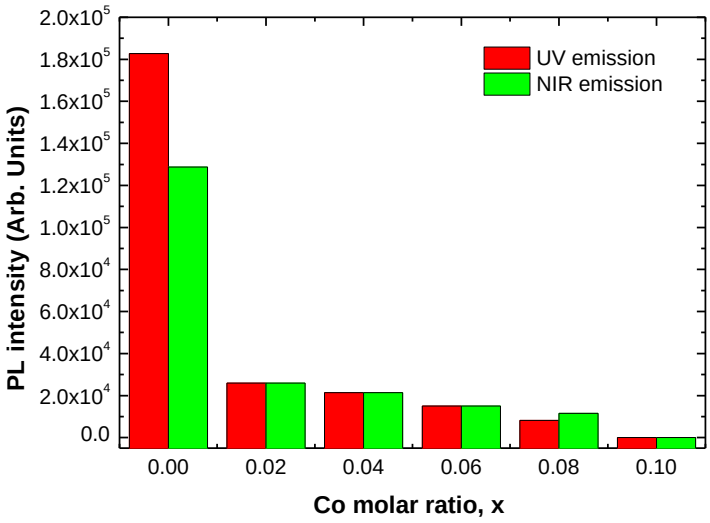

Figure III.13: Variation of UV and NIR emission intensity as a function of Co molar ratio.

The presence of the red emission peak is accompanied with the appearance of several peaks around 400 nm correspond to zinc vacancies V_{Zn} [163], 424 and 448 nm correspond to zinc interstitial Zn_i [163, 164], 478 nm correspond to oxygen vacancies with one trapped electron V_O^+ [163], 519 nm correspond to oxygen vacancies with two trapped electrons V_O [164] and 562 nm correspond to oxygen vacancies without trapped electrons V_O^{++} [164]. For x=0.10, the significant presence of Co defects related red emission compared with ZnO defects (V_O, V_O^+, V_O^{++}, V_{Zn} and Zn_i) related emission peaks indicates the formation of Co agglomerations in excellent agreement with results of XRD (see figure III.1).

III.2. Characterization results of ZnFeO thin films

In this part, ZnFeO thin films were characterized by X-rays diffraction, Raman spectroscopy, UV-visible spectroscopy, and photoluminescence spectroscopy. Experimental results will be presented and discussed as a function of Fe molar ratio x (Eq. II.1).

The whole of results was published in **Journal of Materials Science: Materials in Electronics.** This journal is listed in category "A" according to the DGRSDT journals ranking. This paper can be cited as:

R. Nettour and A. Kabir
Structural and optical changes induced by the incorporation of Fe ions in ZnO matrix.
Journal of Materials Science: Materials in Electronics
36 (2025) 1218

III.2.1. X-rays diffraction

Figure III.14-a presents the XRD patterns of the resulting films from the spray, onto heated glass substrates, of the prepared mixture with Fe molar ratio x=0.00, 0.02, 0.04, 0.06, 0.08 and 0.10. All XRD patterns exhibit five diffraction peaks located around 31.83°, 34.56°, 36.36°, 47.68° and 56.67° attributed respectively to (100), (002), (101), (102) and (110) orientation in the hexagonal wurtzite structure of ZnO, according to the JCPDS# 36-1451 data sheet, with a preferential orientation along to (002) planes. In figure III.14-a, the intensity and the position of each diffraction peak vary from one pattern to another as a function of the Fe molar ratio. A zoom of the (002) diffraction peak is presented in figure III.14-b to exhibit this variation that may be linked to the incorporation of Fe ions in ZnO matrix, influencing the lattice parameters.

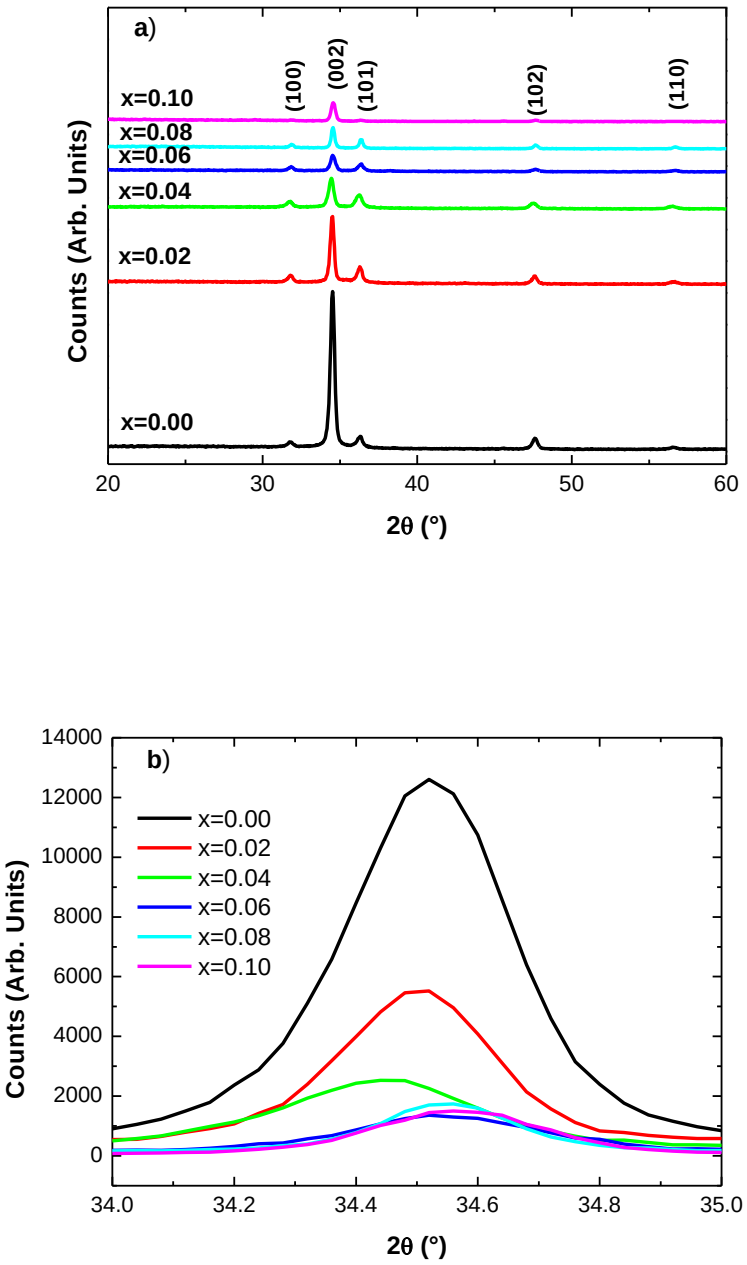

Figure III.14: a) XRD patterns of ZnO films as a function of the Fe-rich solution volume ratio x. b) Zoom of the (002) diffraction peak.

The variation of lattice parameters a and c is presented in figure III.15, as a function of the Fe molar ratio x. The lattice parameters a and c were determined using eq. II.3. The lattice parameters values, in figure III.15, are close to those in [165]. We can see that the lattice

parameters, a=3.251 Å and c=5.204 Å, of the sample without incorporation of Fe ions (i.e., x=0.00) are close to those of the bulk ZnO a_0=3.249 Å and c_0=5.206 Å. The difference between these values may be due to residual stress caused by the substrate nature and/or the substrate temperature.

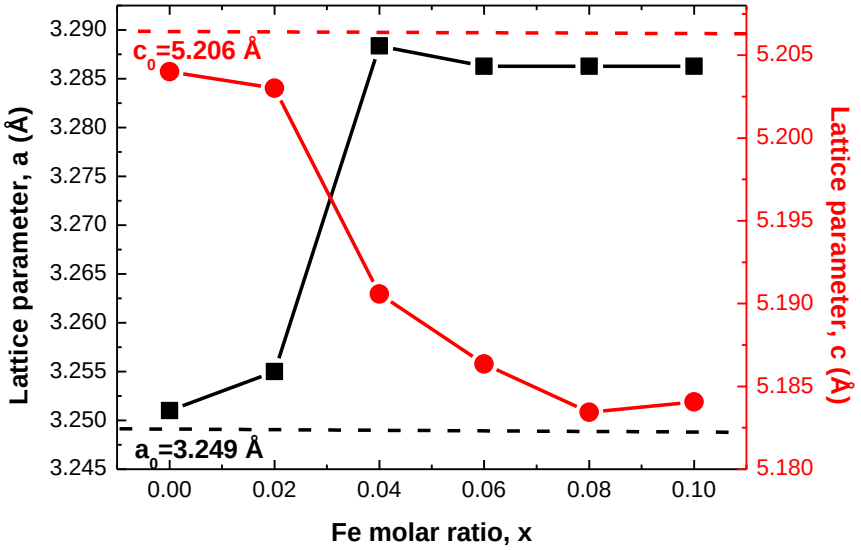

Figure III.15: Variation of lattice parameters as a function of the Fe molar ratio x.

One can see, in figure III.15, that both lattice parameters a and c vary inversely as a function of the Fe molar ratio. When the lattice parameter a increases from 3.251 to 3.288 Å corresponding to x=0.04 and stabilizes after this volume ratio around 3.285 Å, the lattice parameter c decreases from 5.204 to 5.183 Å. The variation of lattice parameters may be due to the incorporation of Fe ions in the ZnO hexagonal structure because all samples were elaborated in the same conditions. The incorporation of Fe ions in ZnO matrix plays a major role in the variation of lattice parameters. This was expected because Fe ions can incorporate the ZnO matrix in two stable forms: F^{2+} with an ionic radius of 92 pm and F^{3+} with an ionic

radius of 78 pm [166]. If we compare these two radii to the radius of Zn^{2+} (88 pm [166]), we can conclude that the substitution of Zn^{2+} by Fe^{2+} will not affect the crystalline structure since they have close radii which is not the case for Fe^{3+}. It radius is smaller than that of Zn^{2+}. This suggests that the variation of lattice parameters (Figure III.15), as a function of Fe molar ratio, is attributed to the dominance of the Fe ions present in the ZnO matrix. In figure III.15, values corresponding to the Fe molar ratio x=0.02 have no significant changes compared with those corresponding to x>0.02. This indicates that the dominant form of Fe ions in ZnO matrix, for x=0.02, is Fe^{2+}. For the other samples, it is Fe^{3+} that dominates the incorporated Fe ions, explaining the stabilization of different parameters after x=0.04. Wang et al. [167] found that incorporated Fe ions existed in ZnO in the form of Fe^{2+} while Baek et al. [168] found the existence of Fe^{3+} in ZnO. Kim and Park [169] found the coexistence of both Fe^{2+} and Fe^{3+} in ZnO matrix.

For the determination of the crystallite size and because of the difficulty of the attribution of the XRD peak broadening, like that in figure III.14-b, to the crystallite size or to the microstrain, we have used the modified Williamson-Hall approach (Eq. II.11) in which, the isotropic microstrain ε is replaced by the anisotropic microstrain $\varepsilon_{hkl} = \frac{\sigma}{Y_{hkl}}$ where σ is the crystal stress and Y_{hkl} is the Young's modulus given, as a function of lattice parameters a and c and Miller indices h, k, and l, by [170] :

$$Y_{hkl} = \frac{\left[h^2 + \frac{(h+2k)^2}{3} + \left(\frac{al}{c}\right)^2 \right]^2}{s_{11}\left(h^2 + \frac{(h+2k)^2}{3} \right)^2 + s_{33}\left(\frac{al}{c}\right)^4 + (2s_{13} + s_{44})\left(h^2 + \frac{(h+2k)^2}{3} \right)\left(\frac{al}{c}\right)^2} \qquad \text{(III.1)}$$

where s_{11}=7.858 ×10^{-12} $N^{-1}m^2$, s_{13}=-2.206 ×10^{-12} $N^{-1}m^2$, s_{33}=6.940 ×10^{-12} $N^{-1}m^2$ and s_{44}=23.570 ×10^{-12} $N^{-1}m^2$ are the elastic compliances of ZnO. An example of a linear fit of the plot of $\beta_{hkl}\cos\theta_{hkl}$ as a function of $\frac{4\sin\theta_{hkl}}{Y_{hkl}}$ is presented in figure III.16. From this fit, both crystal stress σ and grain size D are determined.

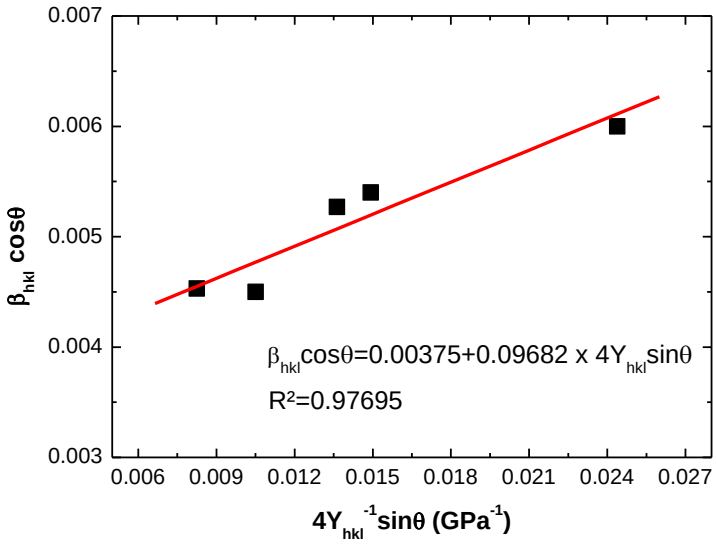

Figure III.16: Linear fit (red line) of the variation of $\beta_{hkl}\cos\theta$ as a function of $4Y_{hkl}^{-1}\sin\theta$.

Figure III.17 presents the variation of the crystal stress and the crystallite size as a function of the Fe molar ratio x. We can see that, before the incorporation of Fe ions in ZnO matrix, i.e. for x=0.00, the grain size is 72 nm, which is in good agreement with results in [171], and the stress is 272 MPa comparable to that in [172] and is linked to substrate temperature and/or nature. Since all samples were deposited onto glass substrate in the same conditions of solution molarity, number of spray and substrate temperature, the variation of both crystal stress and grain size in figure III.17 is due to the incorporation of iron in the matrix of zinc oxide.

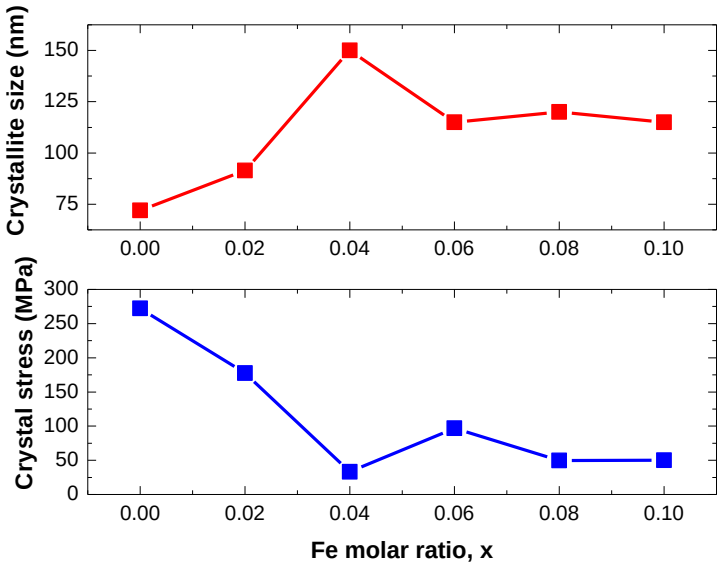

Figure III.17: Variation of the crystallite size and the crystal stress as a function of the Fe molar ratio x.

We can see that the Fe incorporation induces firstly, an increase of the crystallite size to reach a maximum of 150 nm accompanied by a decrease of the crystal stress to a minimum value of 33.12 MPa corresponding to a Fe molar ratio x=0.04 and secondly, a stabilization of both the crystallite size and the crystal stress around 115 nm and 50 MPa, respectively, after x=0.04 which indicates a no effect of Fe ions in ZnO matrix after this ratio.

III.2.2. Raman spectroscopy

Figure III.18 presents Raman spectra of films deposited with a Fe molar ratio x extending from x=0.02 to x=0.10 in the wavenumber range between 200 and 900 cm^{-1}. The spectrum of the sample deposited without Fe molar ratio x=0.00 is also presented. As can be seen in figure III.18, the Raman spectra shape varies as a function of the Fe molar ratio x. For the sample corresponding to x=0.00, we can see the presence of only E_{1L} vibration mode of ZnO located around 580 cm^{-1} [173]. The same remark could be made to the sample

corresponding to x=0.02 and this reflects that there is no effect of the corresponding amount of the incorporated iron ions on the ZnO matrix.

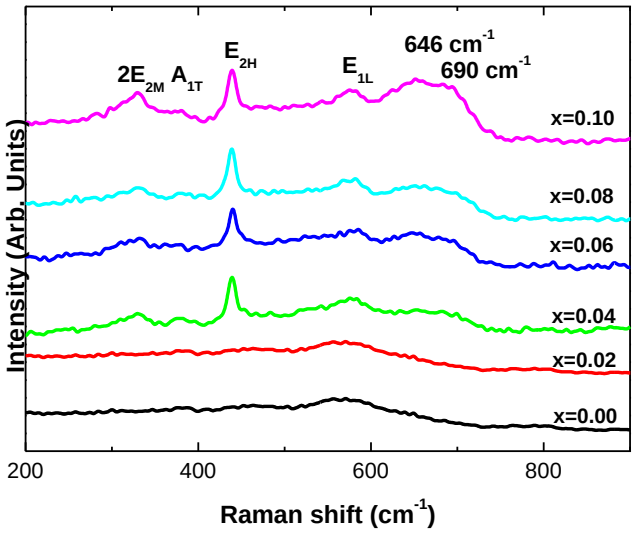

Figure III.18: Raman spectra of Fe ions incorporated ZnO.

Beyond this volume ratio, i.e. from x=0.04, we can see the appearance of additional modes of ZnO such as $2E_{2M}$ around 332 cm^{-1} (belongs to multi-phonons process [139]), A_{1T} around 380 cm^{-1} [141], E_{2H} around 435 cm^{-1} [141] and a broad peak containing two peaks around 646 and 690 cm^{-1} relatable to the vibrations of Fe-O according to [174] and we agree with this assumption since the intensity of these two peaks increase as a function of the Fe molar ratio x as can be seen in figure III.18. One can see that, from x=0.04, the peak related to the E_{2H} mode, which correspond to the vibration of zinc sub-lattice [141], dominates the other ZnO related peaks without any shift which reflects that the incorporation of iron ions into ZnO matrix contributes to the enhancement of the quality of the crystalline structure, and it is confirmed by the correlation between the crystallite size and the E_{2H} related peak area in figure III.19. Zuo et al. [140] reported that the Raman peaks broadening are mainly due to

crystallite size effect. The E_{2H} peak area was determined after a decomposition of the Raman spectrum into Gaussian peaks by taking into consideration all present modes in this frequency range (Inset of figure III.19).

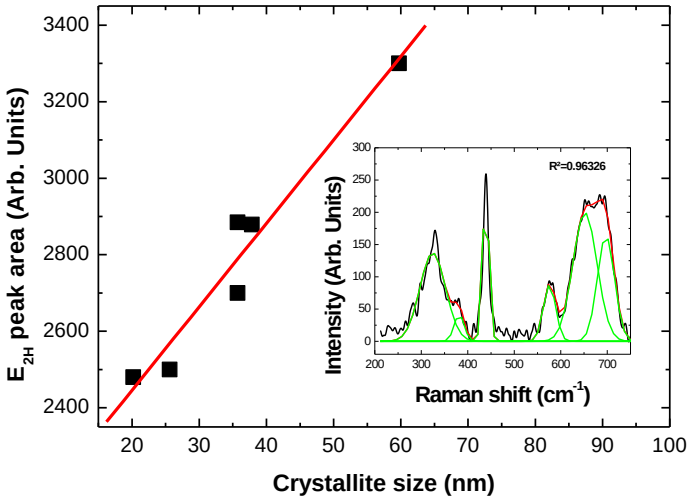

Figure III.19: Correlation between the crystallite size and the E_{2H} related peak area (Red line to guide the eyes). (**Inset:** Example of a deconvolution of a Raman spectrum)

III.2.3. UV-visible spectroscopy

Figure III.20 presents the UV-visible spectra of the elaborated films using Fe molar ratios from x=0.00 to x=0.10. We can see, in figure III.20, that the shape of spectra changes as a function of the Fe molar ratio, which indicates that the incorporation of the Fe ions influences the optical transmittance and also the band gap energy of the elaborated ZnO samples. The band gap energy is determined graphically from the extrapolation of the linear part of the curve $(\alpha\ d\ h\nu)^2$, as a function of $h\nu$, up to the abscissa corresponding to $(\alpha\ d\ h\nu)^2=0$ (Figure III.21). The variation of both the band gap energy E_g and the mean transmittance in the visible region is traced in the inset of figure III.21 as a function of the Fe molar ratio. We

cans see that the mean transmittance in the visible spectral region, i.e. between 800 and 400 nm rapidly decreases from 70.3% for x=0.00 to 39.4% for x=0.02 due to the d-d transition of Fe ions, according to Polyakov et al. [175].

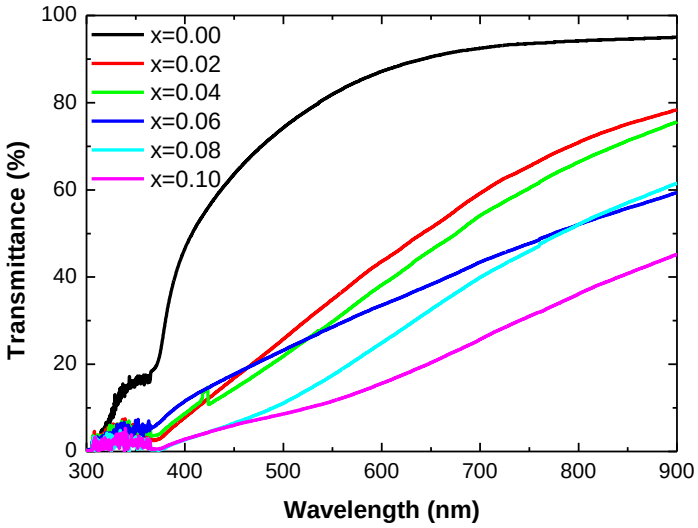

Figure III.20: UV-visible spectra of Fe ions incorporated ZnO.

Kafle et al. [176] found that the transmittance of Fe-doped ZnO decreased by 10% when Fe ion's concentration reached 4 at. %. After x=0.02, one can see the proportionality between the decrease of the mean transmittance and the increase of the incorporated Fe ions in ZnO. In the inset of figure III.21, the band gap energy E_g = 3.45 eV corresponding to x=0.00 is greater than that of the bulk ZnO (3.37 eV) however, it is comparable to those in [176]. The variation of the band gap energy E_g, as a function of the Fe molar ratio x, correlates with that of the crystallite size (Figure III.17) in good agreement with results in [171]. We can see that the incorporation of Fe ions decreases the band gap energy of the prepared samples from 3.45 eV to the lowest value of 3.21 eV, corresponding to x=0.04. After

this ratio, we can see that the band gap energy E_g slightly increases and keeps invariant around 3.27 eV.

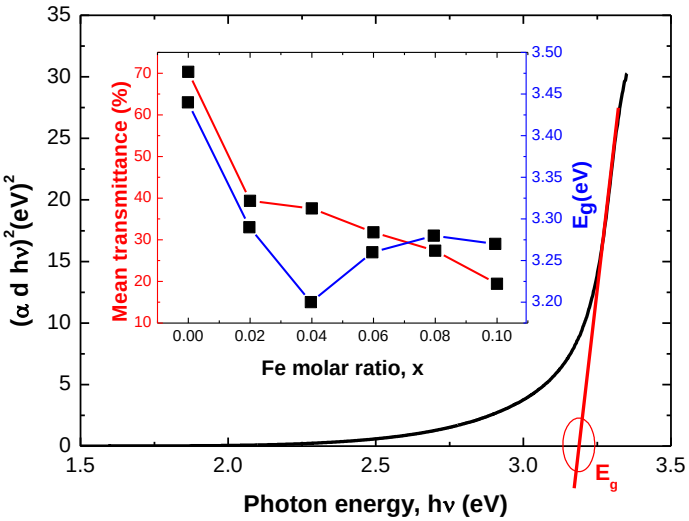

Figure III.21: Plot of $(\alpha dh\nu)^2$ vs. hν. (**Inset:** Variation of the mean transmittance and the band gap energy as a function of the Fe molar ratio x).

According to Parra-palomino et al. [177], the band gap energy decrease is attributed to a change of the Fermi energy state by lowering the minimum of the conduction band and raising the maximum of the valence band, inducing band gap reduction.

The change of the Fermi energy state is caused by the 3d transition of incorporated Fe^{2+} in ZnO [177]. If Fe^{3+} is the dominant form of incorporated Fe ions, they will provide free carriers, causing the Fermi level to bring closer to the conduction band, leading to the band gap enlargement [141]. This reinforces our suggestion concerning the dominance of Fe^{2+} in low ratios ($x \leq 0.04$) and the dominance of Fe^{3+} in high ratios ($x > 0.04$).

III.2.4. Photoluminescence spectroscopy

PL spectra of the zinc oxide film and zinc oxide films incorporated with different amounts of Fe ions are presented in figure III.22. All spectra have the same shape with two dominant emission peaks: ultraviolet (UV) emission in the wavelength range 350-420 nm and near infrared (NIR) emission in the wavelength range 720-800 nm.

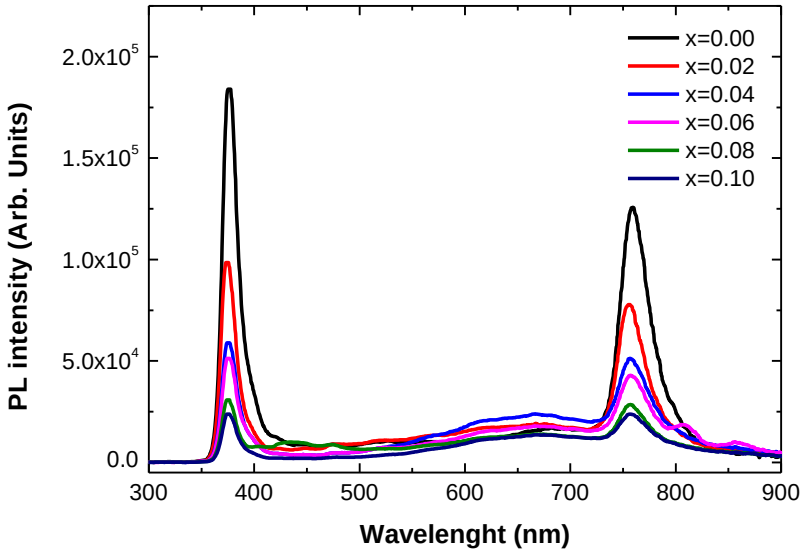

Figure III.22: PL spectra of Fe ions incorporated ZnO.

The ultraviolet (UV) emission is generally linked to the creation, by photostimulation, of excitons of energies near the ZnO band edge. The decrease of this emission peak may be explained by the decrease of the probability of excitons creation induced by the incorporation of Fe ions in ZnO matrix. The variation of the band gap energy deduced from the position of UV emission peaks PL-E_g is traced in figure III.23 as a function of the Fe molar ratio x. We can see that this variation is similar to that of the band gap energy determined from UV-visible spectra (Inset of figure III.21). The quite difference of the PL-E_g values compared with

those determined from UV-visible spectra may be due to the presence of point defects, such as oxygen vacancies (V_O) and zinc interstitials (Zn_i), detected by the PL technique [155]. The near infrared (NIR) emission peak was also found by Wang et al. [160] around 1.64 eV. They attributed this emission to the donor-acceptor transition between V_O and zinc vacancies (V_{Zn}) and/or the radiative recombination of trapped electrons with trapped holes in oxygen interstitial (O_i) [160].

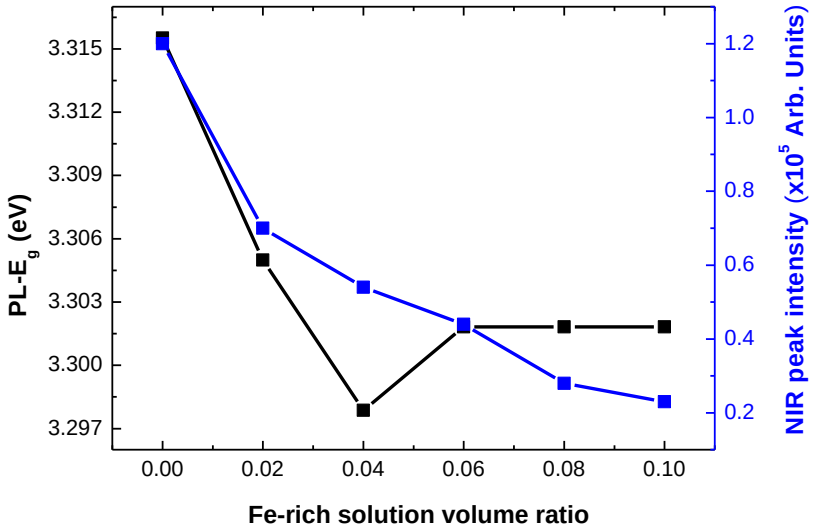

Figure III.23: Variation of PL-Eg and NIR emission peak surface as a function of the Fe molar ratio x.

The variation of the NIR emission peak intensity as a function of the Fe-rich solution volume ratio is presented in figure III.23. The decrease of the NIR emission peak is directly related to the incorporated Fe ions in the ZnO matrix. It has been reported that the incorporation of Fe ions in ZnO suppressed the green [178, 179] and the yellow-green [180] emissions.

III.3. Characterization results of ZnMnO thin films

In this part, the characterization results of ZnMnO thin films will be presented and discussed as a function of Mn molar ratio x determined using eq. II.1. It is to notice that ZnMnO thin film was characterized by X-rays diffraction, ATR-FTIR spectroscopy, UV-visible spectroscopy, and photoluminescence spectroscopy.

III.3.1. X-rays diffraction

Figure III.24 shows XRD patterns of the samples prepared with Mn molar ratio x= 0.00, 0.02, 0.04 and 0.06. For XRD pattern corresponding to x=0.00, five diffraction peaks located around 31.83°, 34.56°, 36.36°, 47.68° and 56.67° could be seen. These peaks correspond to the hexagonal wurtzite structure of ZnO, according to the JCPDS# 36-1451 data sheet, with a preferential orientation along to the (002) plane. We can see that the (002) peak is present in all patterns whatever the Mn molar ratio which is in good agreement with results in [181].

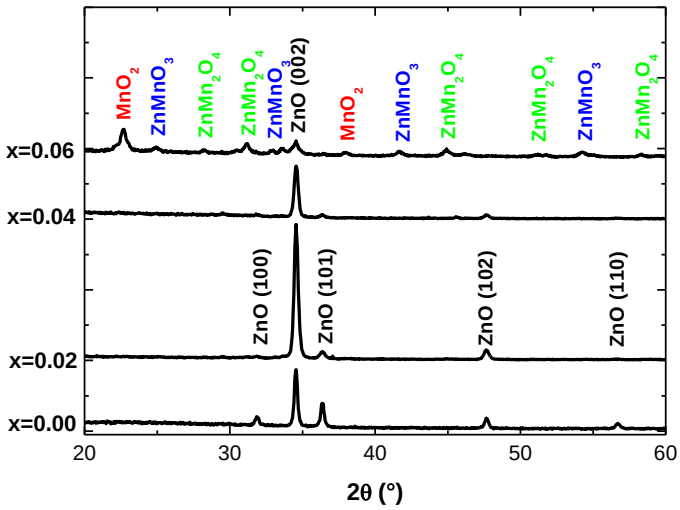

Figure III.24: XRD patterns of ZnO films as a function of Mn molar ratio.

According to figure III.24, the effect of the Mn ions incorporation into ZnO appears from the beginning i.e. from x=0.02 where some XRD peaks disappear and the other lose their intensity before the almost complete disappearing of the ZnO phase when x=0.06. For x=0.02, we can see that, the increase of the (002)-corresponding peak intensity is accompanied with a complete disappear of both (100) and (110)-corresponding peaks and a decrease of the (101)-corresponding peak intensity. This could be interpreted by crystallites rotation induced by the stress resulting from the incorporation of Mn ions in ZnO [134] knowing that the ionic radius of Mn^{2+} (0.08 nm) is greater than that of Zn^{2+} (0.06 nm). For x=0.04, the decrease of the (002)-corresponding peak intensity and the almost complete disappear of the other peaks indicates a degradation of ZnO structure induced by the incorporation of Mn ions evidenced before by Ruan et al. [182]. The (002)-corresponding peak intensity continue decreasing, for x=0.06, where we can see a decomposition of ZnO structure leading to the appearing of MnO_2 phase (JCPDS# 44-0142 data sheet), $ZnMnO_3$ phase (JCPDS# 28-1468 data sheet), and $ZnMn_2O_4$ phase (JCPDS# 24-1133 data sheet). The presence of Mn-related phases in Mn-doped ZnO was evidenced by searchers as a Mn concentration depending phenomenon. For example, the MnO_2 and $ZnMn_2O_4$ phases were obtained by Harsono et al. [183] for 0.1 Mn-doping ZnO while, for the same Mn concentration, Ramos et al. [184] found the presence of Mn_3O_4 phase. The $ZnMnO_3$ phase was obtained by Toloman et al. [185] for a Mn concentration of 0.025.

The variation of the lattice parameter c and the crystal stress σ is plotted, in figure III.25, as a function to Mn molar ratio x. The lattice parameters c was determined from eq. II.3 and the crystal stress σ was determined from the (002)-corresponding peak position using the following relation:

$$\sigma = Y_{002}\varepsilon_{002} = \frac{1}{s_{33}}\left(\frac{c-c_0}{c_0}\right) \quad \text{(III.2)}$$

where Y_{002} is the Young's modulus, ε_{002} the lattice strain, $s_{33}=6.940 \times 10^{-12}$ $N^{-1}m^2$ is the elastic compliance of ZnO and c and c_0 are respectively lattice parameters of the prepared samples and the lattice parameter of the bulk ZnO.

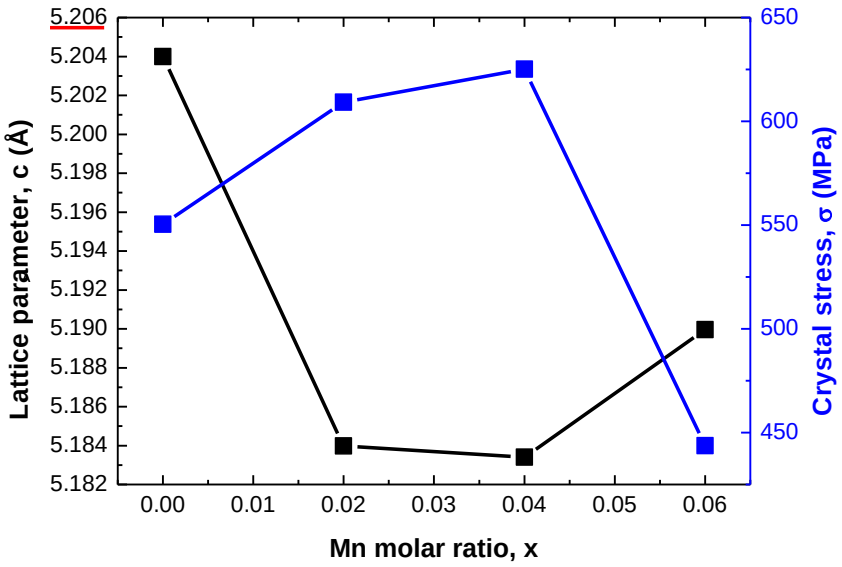

Figure III.25: Variation of lattice parameter c and crystal stress as a function Mn molar ratio.

The observed difference between the lattice parameter c of the pure ZnO (5.202 Å) and that of the bulk ZnO (5.206 Å) is due to residual stress induced by the substrate temperature and/or the substrate nature [126]. From x=0.02, the lattice parameter c decreases to reach its lowest value of 5.183 Å for x=0.04 caused by the incorporation of Mn ions in the ZnO structure. This decrease of the lattice parameter c indicates the presence of a compressive stress resulting from the fact that the ionic radius of Mn^{2+} is greater than that of Zn^{2+} [186]. The compressive stress reaches its maximum of 625 MPa for x=0.04. For x=0.06, the increase

of the lattice parameter c is accompanied with a stress relaxation may be due to the decomposition of the ZnO structure leading the appearance of other Mn-related phases.

The crystallite size D, determined using the Williamson Hall method (Eq. II.10), and the (002)-corresponding peak intensity are plotted, in figure III.26, as a function of Mn molar ratio x. For x=0.00, the crystallite size (72 nm) is in good agreement with those in literature [173, 187]. The decrease of the crystallite size from 72 to 57 nm, for x=0.02 (Figure III.26), is accompanied by the increase of the (002)-corresponding peak intensity. For x=0.04, the (002)-oriented crystallite size remains almost invariant around 57 nm while the (002)-corresponding peak intensity decreases reflecting a decrease of crystallites number which indicates a degradation of ZnO structure induced mainly by the incorporation of Mn ions.

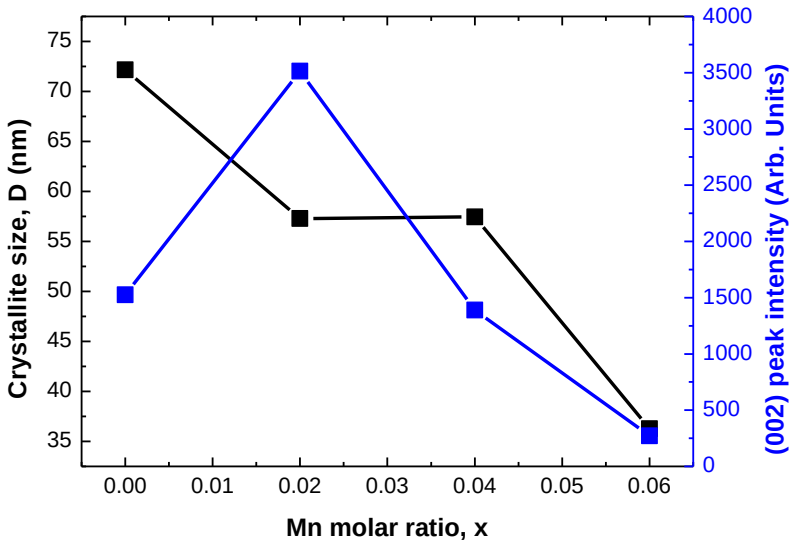

Figure III.26: Variation of the crystallite size and the (002) peak intensity as a function of Mn molar ratio x.

This structural behavior of ZnO was also observed by Yang et al. [188] and Shatnawi et al. [189]. For x=0.06, the decrease of both the (002)-oriented crystallite size and the (002)-

corresponding peak intensity coincides with the appearance of Mn-related phases which indicates the ZnO decomposition.

III.3.2. ATR-FTIR spectroscopy

Figure III.27 presents ATR-FTIR spectra of the prepared samples, with Mn molar ratio x=0.00, 0.02, 0.04 and 0.06, recorded in ambient air. We can see that, the spectrum corresponding to x=0.00 exhibits two asymmetric peaks containing a peak around 1150 cm^{-1} linked to C-O-H [145], a peak around 1060 cm^{-1} linked to Zn-O-Zn [146], a peak around 890 cm^{-1} linked to -OH [147], a peak around 875 cm^{-1} linked to O-C-O [148], a peak around 760 cm^{-1} linked to Zn-O-H [146] and a peak around 700 cm^{-1} linked to Zn-O-Zn [146].

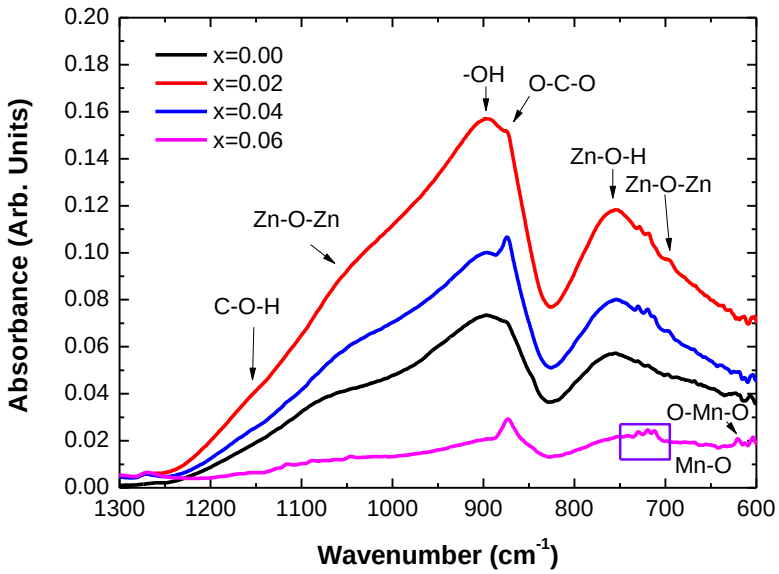

Figure III.27: ATR-FTIR spectra of ZnO films as a function of Mn molar ratio x.

For Mn molar ratios x=0.02 and x=0.04, we can see that these two spectra have the same shape as for the spectrum corresponding to x=0.00 with additional peaks between 740

and 710 cm^{-1} linked to Mn-O [190, 191] confirming the incorporation of Mn in the ZnO matrix. For x=0.06, we can see that the appearing of a peak around 620 cm^{-1} linked O-Mn-O [192] is accompanied by the disappearing of peaks related linked to Zn-O-Zn which indicates a degradation of the hexagonal ZnO structure in good agreement with results of XRD analysis.

III.3.3. UV-visible spectroscopy

Figure III.28 presents UV-Visible spectra of the prepared films, with Mn molar ratios from x=0.00 to x=0.06. We can see that the shape of spectra corresponding to x=0.02, 0.04 and 0.06 is quite different from that corresponding to x=0.00. This difference may be directly related to the incorporation Mn in ZnO matrix.

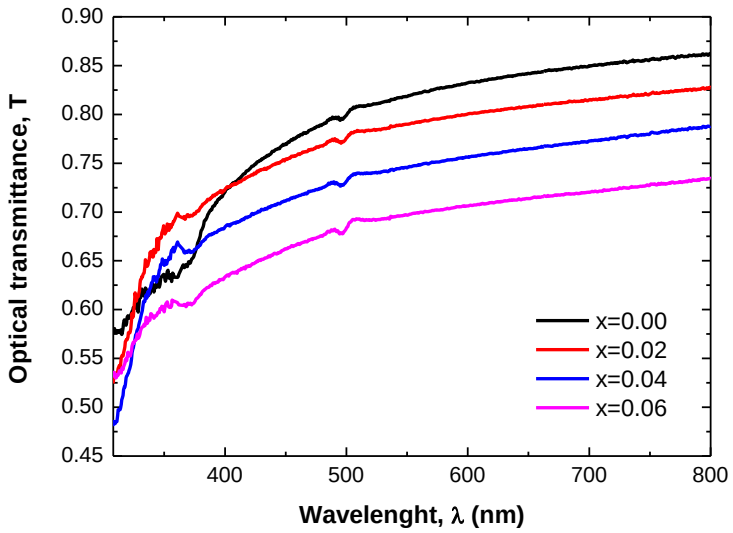

Figure III.28: UV-Visible spectra of ZnO films as a function of Mn molar ratio x.

We can see, for all spectra, that the transmittance in the visible region varies from a sample to another with the presence of an absorption band located around 490 nm may be due

to ZnO surface defects attributed to transition between oxygen vacancies V_O and oxygen interstitials O_i [193].

The variation of the mean transmittance T_m in the visible region between 400 and 800 nm, as a function of Mn molar ratio x is presented in the inset of figure III.29. We can see that the decrease of the mean transmittance decreases from 80%, for x=0.00, to 60% for x=0.06 correlates with the increase of the incorporated Mn amount. This indicates that the incorporation of Mn in ZnO increased the absorption of visible light which is in good agreement with results in [194].

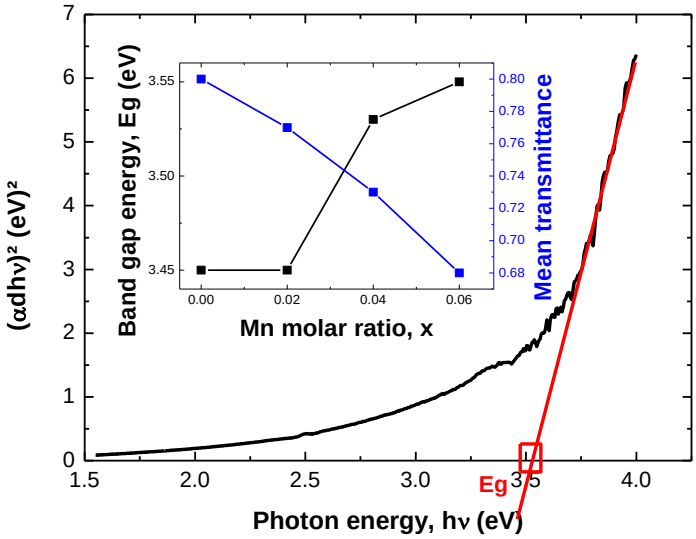

Figure III.29: Plot of $(\alpha dh\nu)^2$ vs. hν (**Inset:** Variation of the band gap energy and the mean optical transmittance as a function of Mn molar ratio x).

The variation of the band gap energy E_g is also presented, in the inset of figure III.29, as a function of Mn molar ratio. The band gap energy is determined from the extrapolation of the linear part of the curve $(\alpha dh\nu)^2$, as a function of photon energy hν, up to the abscissa

corresponding to $(\alpha dh\nu)^2=0$ (Figure III.29). The band gap energy value for x=0.00 (3.45 eV) is comparable to those in literature [195, 196]. For x=0.02 the band gap energy value keeps invariant indicating a no effect of this amount of incorporated Mn on the band gap energy of the pure ZnO. Beyond this Mn molar ratio, the band gap energy rapidly increases to reach 3.53 eV for x=0.04 and 3.55 eV for x=0.06. The increase of the band gap energy with the increasing amount of incorporated Mn ions correlates with the decrease of the crystallite size (Figure III.26) and was evidenced before by Tan et al. [197], Wu et al. [198] and Kayani et al. [199]. The increase of the band gap energy, for x=0.04, could be interpreted by the decrease of sp-d exchange interactions caused by the increase of the amount of incorporated Mn in ZnO [151] or by the Burstein–Moss effect [200, 201]. For x=0.06, the reason of the increase of the band gap energy may be attributed to the contribution of MnO_2, $ZnMnO_3$ and $ZnMn_2O_4$ phases (Figure III.24).

III.3.4. Photoluminescence spectroscopy

Figure III.30 presents photoluminescence PL spectra of elaborated samples using Mn molar ratio x=0.00, 0.02, 0.04 and 0.06. We can see that the shape of PL spectra changes as a function of Mn molar ratio. In addition to a broad red emission peak around 680 nm, two dominant emission peaks can be observed on the PL spectrum corresponding to x=0.00: an ultraviolet UV emission around 375 nm and a near infrared NIR emission around 759 nm. The UV emission is generally related to the creation, by photo stimulation, of excitons of energies near the ZnO band edge and in good agreement with the optical band gap energy values determined from UV-visible spectroscopy. The red emission peak around 680 nm is attributed to oxygen vacancies V_O defects [202]. The NIR emission peak was also found by Wang et al. [160] around 756 nm. They attributed this emission to the donor-acceptor

transition between oxygen vacancies V_O and zinc vacancies V_{Zn} and/or the radiative recombination of trapped electrons with trapped holes in oxygen interstitial O_i [160]. For x=0.02, the intensity of the UV emission peak and the NIR emission peak, without a change in the peaks position, may be due to the structural degradation induced by Mn ions incorporation. For x=0.04 and x=0.06, we can see that the shape of their corresponding spectra is similar and is different from that of x=0.00 and x=0.02 corresponding spectra.

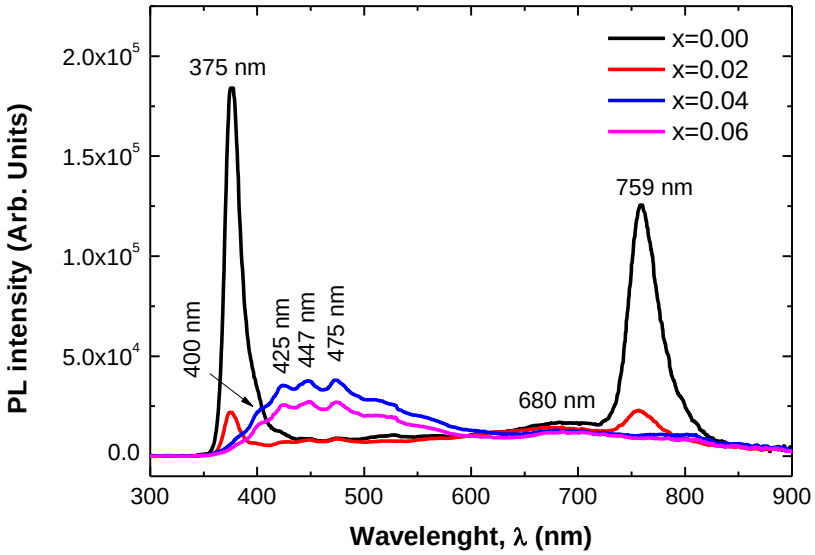

Figure III.30: PL spectra of ZnO films as a function of Mn molar ratio x.

One can see that both UV and NIR emission peaks disappear leading the place to a violet emission peak around 400 nm, two blue emission peaks, around 425 and 447 nm, and a blue-green emission peak around 475 nm. According to literature [202, 203], the violet emission around 400 nm is attributed to Mn^{2+} ions, the blue emissions around 425 and 447 nm are respectively attributed to V_{Zn} and Zn interstitial Zn_i while the blue-green emission around 475 nm is attributed to V_{Zn}. The intensity of these emission peaks decrease, for x=0.06,

caused probably by the decomposition of ZnO and the formation of other phases like MnO_2, $ZnMnO_3$ and $ZnMn_2O_4$.

Conclusion

In this work, thin films of ZnTMO (TM=Co, Fe, and Mn) were deposited using, the spray pyrolysis technique, in order to study the effect of doping element on the structural, optical and photoluminescence properties of ZnO. For this rison, the as elaborated ZnTMO thin films have been subject of series of characterization by X-rays diffraction (XRD), Raman spectroscopy, ATR-FTIR spectroscopy, UV-visible spectroscopy, and photoluminescence spectroscopy. The whole characterization results showed that changes induced in ZnO differ from a doping element to another.

For ZnCoO thin films, XRD patterns revealed a decrease of the crystalline quality of ZnO from Co molar ratio x=0.06. For x=0.10, two secondary phases Co_3O_4 and $Zn(OH)_2$ appeared suggesting that Co inclusion slowed down the formation of hexagonal ZnO phase. The presence of secondary phases was confirmed by Raman spectroscopy and ATR-FTIR spectroscopy. This last evidenced the enhancement of ZnO surface adsorption of CO_2 and H_2O induced by Co inclusion. According to UV-Visible spectroscopy, as a function of Co molar ratio, the mean transmittance in the visible region decreased from 70.33% to 23.25% and the band gap energy E_g decreased from 3.45 eV to reach its lowest value 2.67 eV for x=0.08. The increase of the band gap energy for x=0.10 (2.84 eV) may be interpreted by the decrease of sp-d exchange interactions caused by the formation of Co_3O_4 and $Zn(OH)_2$ secondary phases. All PL spectra, except for that corresponding to x=0.10, exhibited an UV emission peak around 375 nm and a NIR emission peak around 754 nm. The intensity of these two emission peaks decreased as a function of Co molar ratio. The complete disappearing of these two emissions, for x=0.10, was accompanied with the appearance of a red emission around 697 nm, attributed to Co-based impurities, and other peaks attributed to deep level defects in ZnO.

For ZnFeO thin films, the variation of the crystalline parameters as a function of the Fe molar ratio indicated an enhancement of the crystalline properties from x=0.02 to x=0.04 followed by a stabilization after 0.04. Raman spectra showed the presence of optical phonon vibration modes of ZnO in addition to two other peaks located at 646 and 690 cm^{-1} attributed to Fe-O vibration modes. The correlation between the crystallite size and the E_{2H} peak area indicated the same manner of action of incorporated Fe ions in enhancing ZnO structure. The mean transmittance in the visible region, determined from UV-visible spectra, decreased with the increasing Fe molar ratio and the band gap energy E_g decreased to reach a lowest value of 3.21 eV for x=0.04 before stabilizing around 3.27 eV after this ratio. PL spectra exhibited two intense peaks corresponding to UV and NIR emissions. The variation of the band gap energy PL-E_g as a function of the Fe molar ratio is similar to that determined using UV-visible spectroscopy. The decrease of the NIR emission peak intensity was attributed to the incorporated Fe ions. The obtained results evidenced the structural and optical properties of ZnO dependence on the form and the amount of incorporated Fe ions.

For ZnMnO thin films, the variation of the lattice parameter, for x=0.02 and x=0.04 indicated the presence of compressive stress caused by the incorporation of Mn ions in ZnO. The stress relaxation, for x=0.06, was accompanied with the appearing of other phases such as MnO_2 and $ZnMnO_3$ resulting from the decomposition of ZnO. The crystallite size decreased from 72 to 36 nm as a function of Mn molar ratio confirming the degradation of ZnO structure. This structure degradation was also confirmed from ATR-FTIR spectra in which, Zn-O-Zn related absorption band disappeared for x=0.06. The mean transmittance in the visible region determined from UV-visible spectra, decreased from 80 to 60% while the band gap increased from 3.45 to 3.55 eV as a function of Mn molar ratio x. PL spectra revealed that UV and NIR emission peaks decreased rapidly for x=0.02 indicating a degradation of the ZnO

structure. For x=0.04 and x=0.06, Both emission peaks disappeared leaving their places to violet, blue and blue-green emission peaks attributed respectively to Mn^{2+} ions, Zn_i and V_{Zn}.

Even Co, Fe, and Mn doping degraded some interesting characteristics of ZnO, it is still a serious candidate for use in multiple domains such as gas sensing, light emitting diodes (LED), and solar cells in addition to data storage.

References

[1] S. Sakthinathan, GA. Meenakshi, S. Vinothini, CL. Yu, CL. Chen, TW. Chiu, and N. Vittayakorn, Processes 13 (2025)587.

[2] S. Rubin, D. Mizrachi, N. Friedman, H. Edri and T. Golan, Fusion of Multidisciplinary Research, An International Journal 4 (2023)1.

[3] M. Ghougali, Doctorate Thesis, University of Mohamed Khider, BISKRA (2019).

[4] SN. Ogugua, OM. Ntwaeaborwa and HC. Swart, Coatings 10 (2020) 1078.

[5] R. Amari, Doctorate Thesis, University of Mohamed Boudiaf -M'sila (2020).

[6] RR. Cranston and BH. Lessard, RSC Adv. 11 (2021) 21716.

[7] C. Cao and Q. An, CrystEngComm 27 (2025) 3404.

[8] E. Acosta, Chapter Thin Films/Properties and Applications (2021) DOI: 10.5772/intechopen.95527.

[9] SA. Mahyoub, A. Farid, MZ. Azeem, D. Fadhil, FA. Qaraah and QA. Drmosh, Small Structures 6 (2025) 5.

[10] FTZ. Toma, MS. Rahman and KH. Maria, Discover Materials 5 (2025) 60.

[11] G. Wu, Y. Wang, Q. Gong, L. Li and X. Wu, IEEE Access 10 (2022) .

[12] AJ. Haider, T. Alawsi, MJ. Haider, BA. Taha and HA. Marhoon, Optical and Quantum Electronics 54 (2022) 488.

[13] T. Nimalan and MR. Begam, International Journal of Thin Films Science and Technology 1 (2024) 59.

[14] MN. Chaudhari, RB. Ahirrao and SD. Bagul, International Journal for Research in Applied Science and Engineering Technology 9 (2021) 6.

[15] OO. Abegunde, ET. Akinlabi, OP. Oladijo, S. Akinlabi and AU. Ude, AIMS Materials Science 6 (2019) 174.

[16] L. Sun, G. Yuan, L. Gao, J. Yang, M. Chhowalla, MH. Gharahcheshmeh , KK. Gleason, YS. Choi, BH. Hong and Z. Liu, Nature Reviews Methods Primers 1 (2021) 5.

[17] DM. Mattox, Handbook of physical vapor deposition (PVD) processing, (2010).

[18] RS.Pedanekar, SK.Shaikh, KY.Rajpure, Current Applied Physics 20 (2020) 917.

[19] MN. Chaudhari, RB. Ahirrao, SD. Bagul, Int. J. Res. Appl. Sci. Eng. Technol 6 (2021) 9.

[20] M. Brella, Doctorate Thesis, University of Kasdi Merbah, Ouargla (2022).

[21] M. Murthi and JF. Destino, Journal of Sol-Gel Science and Technology (2025) https://doi.org/10.1007/s10971-025-06664-1.

[22] KE. Koné, Doctorate Thesis, University Politècnica de València (2023).

[23] AG. Ricciardulli and PWM. Blom, Advanced Materials Technologies (2020) https://doi.org/10.1002/admt.201900972

[24] S. Choudhury, Private communication, Santipur college, Nadia, West Bengal (2024).

[25] RR. Chamberlin, JS. Skarman, Journal of the Electrochemical Society 113 (1966) 86.

[26] JP. Sawant ,RJ. Deokate, HM. Pathan and RB. Kale, Engineered Science 13 (2021) 51.

[27] CB. Sutar, KR. Barde, AV. Patil, JP. Nehete, PV. Dalal and AN. Sonar , International Journal of creative Research thought , 10 (2022) 11.

[28] CM Lampkin, Prog. Cryst. Growth Chara. 1 (1979) 405.

[29] VK. Singh, Emerg. Technol. Innov. Res. 4 (2017) 1.

[30] SS. Shinde, PS. Shinde, YW. Oh, D. Haranath, CH. Bhosale and KY. Rajpure, Applied Surface Science 258 (2012) 9969.

[31] M. Othmane, Doctorate Thesis, University of Mohamed Khider, Biskra (2018).

[32] C. Habis, J. Zaraket and M. Aillerie, Defect and Diffusion Forum 417 (2022) 243.

[33] M. Krajewski, M.Tokarczyk, P. Swietochowski, P. Wrobel, M. Kaminska and A. Drabinska, ACS omega 8 (2023) 33.

[34] H. Harsono, MA. Pamungkas, V. Febia and AL. Gaol, EUREKA: Physics and Engineering 3 (2024) 121.

[35] P. Sharma, MR. Hasan, NK. Mehto, A. Bishoyi and J. Narang, Sensors International, 3 (2022) 100182.

[36] A. Rosset, PhD Thesis, University Perpigan Via Domita (2017).

[37] Ü. Özgür et al., J. Appl. Phys 98 (2005)11.

[38] D. Buckley, A. Lonergan and C. O'Dwyer, ECS Journal of Solid State 14 (2025) 015001.

[39] F. Decremps, J. Zhang and RC. Liebermann, Europhysics Lett. 51 (2000) 268.

[40] FZ. Nouasria, Doctorate Thesis, University of kasdi merbak, Ouargla (2022).

[41] M. Verde, Bol. Soc. Esp. Ceram. Vid. 53 (2014) 149.

[42] A. Maache, Doctorate Thesis, University de Ferhat Abbes, Sétif 1 (2021).

[43] HA. Hamid, KA. Razak, International Journal of Electroactive Materials, 8 (2020) 37.

[44] S. Besra, Doctorate Thesis, University of Kasdi Merabah, Ouargla (2024).

[45] W. Allag, Doctorate Thesis, University of Ferhat Abbas, Sétif1 (2022).

[46] F. Oba, A. Togo, I. Tanaka, J. Paier and G. Kresse, Physical Review B 77 (2008) 245202.

[47] S. Marouf, Doctorate Thesis, University Ferhat Abbas, Sétif 1 (2017).

[48] S. Nadupalli, S. Repp, S. Weber and E. Erdem, Nanoscale 13 (2021) 9760.

[49] A.M. Alsaad, A.A. Ahmad, I.A. Qattan, Q.M. Al-Bataineh and Z. Albataineh, Crystals 10 (2020) 256.

[50] AA. Sokol, SA. French, ST. Bromley, CRA. Catlow, Huub J. J.V. Dam and P. Sherwood, Faraday Discussions 134 (2007) 267.

[51] Y. Kim, C. Jang, J. Demouth and S. Lee, ACM SIGGRAPH Asia 5 (2009) Art. ID 161.

[52] P. Erhart, A. Klein, and K. Albe, Physical Review B 73 (2006) 205203.

[53] AF. Kohan, G. Ceder, D. Morgan and CG. Van de Walle, Physical Review B 61 (2000) 15019.

[54] P. Erhart, K. Albe and A. Klein, Physical Review B 72 (2005) 0852013.

[55] K. Vanheusden, WL. Warren, CH. Seager, DR. Tallant, JA. Voigt and BE. Gnade, Journal of applied 79 (1996) 7983.

[56] FH. Leiter, HR. Alves, A. Hofstaetter, D.M. Hofmann and BK. Meyer, Basic Solid Physics, 226 (2009) 13.

[57] DM Hofmann, D Pfisterer, J Sann, BK Meyer, R Tena-Zaera, V Munoz-Sanjose, T Frank and G. Pensl, Applied Physics A 88 (2007) 2855.

[58] A Janotti, CG Van de Walle. Reports on progress in physics 72 (2009) 126501.

[59] X. Li, X. Zhu, K. Jin and D. Yang, Optical Materials 107 (2020) 225.

[60] E. Benrezgua, B. Deghfel, A. Mahroug, M.K. Yaakob, A. Boukhari, R. Amari, S. Kheawhom and A.A. Mohamad, Materials Science in Semiconductor Processing 134 (2021) 106012.

[61] G. Voicu, D. Miu, C.-D. Ghitulica, S.-I. Jinga, A.-I. Nicoara, C. Busuioc and AM. Holban, Ceram. Int. 46 (2020) 3904.

[62] A. Mahroug, R. Amari, A. Boukhari, B. Deghfel, L. Guerbous and N. Selmi, Journal of Nanoelectronics and Optoelectronics 13 (2018) 732.

[63] TK. Pathak, HC. Swart, RE. Kroon, Physica B 535 (2018) 314.

[64] MH. Rashid, SI. Sujoy, MS. Rahman, MJ. Haque, Heliyon, 10 (2024) 3.

[65] M.Yang, W.Chen, L.Wang, Z.Liang, G.Ma, K.Ogino, J.Bi, W.Yang, W.Yang and H.Hou, Colloids and Surfaces A 702 (2024).

[66] RS. Pedanekar, SK. Shaikh and KY. Rajpure, Current Applied Physics 20 (2020) 8.

[67] MN. Chaudhari, RB. Ahirrao and SD. Bagul, Int. J. Res. Appl. Sci. Eng. Technol 9 (2021) 6.

[68] M. Murthi and JF. Destino, Journal of Sol-Gel Science and Technology (2025) https://doi.org/10.1007/s10971-025-06664-1.

[69] A. Shabani, MK. Nezhad, N. Rahmani, YK. Mishra, B. Sanyal and J. Adam, Advanced Photonics Research (2021) https://doi.org/10.1002/adpr.202000086

[70] M. Singh and F. Scotognella, Micromachines 14 (2023) 536.

[71] FZ. Bedia, A. Bedia, SM. Bedia, N. Maloufi and M. Aillerie, AIP Advances 15 (2025) 2025.

[72] F. Kanwal, T. Javed, F. Hussain, M. Wasim and M. Batool, Environmental Technology Reviews 13 (2024) 1.

[73] RC. Pawar, DH. Choi, JS. Lee and CS. Lee, Materials Chemistry and Physics 151 (2015) 167.

[74] A. BM and MS. Dennison, Scientific Reports (2025).

[75] B. Abebe, NK. Gupta and D. Tsegaye, RSC advances 14 (2024) 17338.

[76] TNQ. Trang, TB. Phan, ND. Nam and VTH. Thu, ACS applied materials and interfaces 12 (2020) 10.

[77] SH. Zyoud and AF. Omar, Physica B: Condensed Matter 694 (2024) 1.

[78] SH. Zyoud, AF. Omar, Scientific Reports 11 (2025) 9.

[79] S. 79 Ahmad, M. Aadil, SR. Ejaz, MU. Akhtar, H. Noor, S. Haider, IA. Alsafari and G.Yasmin, Ceramics International, 48 (2022) 2.

[80] M. Samadi, M. Zirak, A. Naseri and E. Khorashadizade, Thin solid films 605 (2016) 2.

[81] F. Kanwal, T. Javed, F. Hussain, M. Wasim and M. Batool, Environmental Technology Reviews 13 (2024) 1.

[82] D. Mandal, LK. Sharma and S. Mukherjee, Applied Physics A, 122 (2016) 1033.

[83] AKM. Alsmadi, B. Salameh and M. Shatnawi, The Journal of Physical Chemistry C 124 (2020) 29.

[84] N. Ali, B. Singh, V. Ar, S. Lal, CS. Yadav, K. Tarafder and S. Ghosh, The Journal of Physical Chemistry C 125 (2021) 14.

[85] B. Abebe, NK. Gupta, D. Tsegaye, RSC advances, 2024.

[86] P. Sharma, A. Gupta, K. V. Rao, F. J. Owens, R. Sharma, R. Ahuja, JMO. Guillen, B. Johansson and GA. Gehring, Nature materials 15 (2003) 673.

[87] Z. Chen, Y. Fang, L. Wang, X. Chen, W. Lin and X. Wang, Applied Catalysis B: Environmental 296 (2021) 130.

[88] K. Chehhat, A. Mecif, AH. Mahdjoub, R. Nazir, MA. Pandit, F. Salhi and A. Noua, Journal of Sol-Gel Science and Technology 106 (2023) 85.

[89] A. Kaphle, E. Echeverria, DN. Mcllroy, K. Roberts and P. Hari, Journal of Nanoscience and Nanotechnology 19 (2019) 3893.

[90] A. Chanda, S. Gupta, M. Vasundhara, SR. Joshi, GR. Mutta and J. Singh, RSC advances, (2017).

[91] J. Kazmi, PC. Ooi, S. RA. Raza, BT. Goh, SSA. Karim, MH. Samat, MK. Lee, MF. Mohd Razip Wee, MFM. Taib and MA. Mohamed, Journal of Alloys and Compounds 872 (2021).

[92] B. Salameh, AM. Alsmadiand and M. Shatnawi, Journal of Alloys and Compounds 835 (2020).

[93] C. P. Rajan, N. Abharana, S. N. Jha, D. Bhattacharyya and T. T. John, J. Phys. Chem. C 22 (2021) 13523.

[94] T. Srinivasulu, K. Saritha, S. Rasool, P. Babu, KT. Reddy, A. Campa and M. Topic, Journal of Materials Science : Materials in Electronics (2024) DOI:10.1007/s10854-024-14125-8.

[95] MP. Gonullu, DD. Cakil and C. Cetinkaya, Thin Solid Films 793 (2024) 140265.

[96] TA. Taha, EM. Ahmed, AI. El-Tantawy and AA Azab, Journal of Materials Science: Materials in Electronics 33 (2022) 6368.

[97] R. Kumar, G. Kumar, O. Al-Dossary and A. Umar, Materials Express vol. 5 (2015).

[98] A. Laghouage and H. Bencheikhe , Private communication (2018).

[99] A. Wibowo, MA. Marsudi, MI. Amal and MB. Ananda, RSC Adv. 10 (2020) 42838.

[100] S. Vyas, Johnson Matthey Technology Review 64 (2020) 202.

[101] M. Hjiri, F. Bahanan, M. S. Aida, L. El Mir, and G. Neri, J Inorg. Organomet. Polym. Mater. 30 (2020) 4063.

[102] V. A. Karpina et al. Cryst. Res. Technol. 39 (2004) 980.

[103] A. Hirohata and K. Takanashi, Journal of Physics D: Applied Physics 47 (2014) 193001.

[104] A. Pandey, S. Dalal, S. Dutta and A. Dixit, Journal of Materials Science: Materials in Electronics 32 (2021) 1341.

[105] K. Bennaceur, Doctorate Thesis, University Mohamed Khider, Biskra (2020).

[106] M. Zerouali, Doctorate Thesis, University of 20 août 1955-Skikda (2024).

[107] A. Latif, Doctorate Thesis, University of Mohamed Khider, Biskra (2024).

[108] M. Kawsar, MS. Hossain, NM. Bahadur and S. Ahmed, Heliyon, Vol 10, Issue 3, (2024).

[109] G.B. Harris, « X. Quantitative measurement of preferred orientation in rolled uranium bars », The London, Edinburgh, and Dublin Philosophical Magazine and Journal of Science, Vol 43, Issue 336, (2009).

[110] Á. Fernández-Galiana, O. Bibikova, S. Vilms Pedersen and MM. Stevens, Advanced Materials, 36 (2024) 43.

[111] X. Fu, PhD Thesis, University of California, Los Angeles (2025).

[112] DR. Neuville, D. De Ligny and GS. Henderson, Reviews in mineralogy and geochemistry 78 (2014).

[113] Z. Yang, X. Wang, W. Chen, H. Tang, R. Zhang, X. Fan, G. Zhang and J. Fan, Laser & Photonics Reviews 18 (2024) 2301300.

[114] D. Yuvaraj, K. Narasimha Rao, Vacuum 82 (2008) 11.

[115] R. Azizi, Doctorate Thesis, University of Mohamed Khider, Biskra (2020).

[116] D. Rajni, K. Ashish and KG. Bhaskar, International Journal Of Novel Research And Development 9 (2024) 10.

[117] AM. Alshehawy, DEA. Mansour, M. Ghali, M. Lehtonen and MMF. Darwish, Processes 9 (2021) 5.

[118] S. Benhamida, Doctorate Thesis, University of Mohamed Khider, Biskra (2018).

[119] R. Swanepoel, Journal of Physics E: Scientific Instruments 16 (1983) 1214.

[120] S. Naceur, Doctorate Thesis, University of Mohamed Khider, Biskra (2023).

[121] H.Rai, N. Kondal, Materials Today : Proceedings 48 (2022) 1320.

[122] M. Ivill, S. J. Pearton, S. Rawal, L. Leu, P. Sadik, R. Das, A. F. Hebard, M. Chisholm, J. D. Budai, D. P. Norton, New J. Physics 10 (2008) 065002.

[123] A. Sundararaj, G. Chandrasekaran, Nano-Struct. & Nano-Objects 11 (2017) 20.

[124] R. Bagheri and H. Kafashan, Ceram. Inter. 50 (2024) 37041.

[125] P. Gu, X. Zhu and D. Yang, RSC Adv. 9 (2019) 8039.

[126] J.F. Chang, C.C. Shen, M.H. Hon, Ceramics International 29 (2003) 245.

[127] A. Yildiz, B. Yurduguzel, B. Kayhan, G. Calin, M. Dobromir, F. Iacom, J. Mater. Sci.: Mater. Electron. 23 (2012) 425.

[128] M. R. Arefi-Rad and H. Kafashan, Ceram. Internat. 50 (2024) 31826.

[129] A. Monshi, M.R. Foroughi, M.R. Monshi, World J. Nano Sci. Eng. 2 (2012) 154.

[130] G.K Williamson, W.H Hall, Acta Metallurgica1 (1953) 22.

[131] R. Bagheri and H. Kafashan, Phys. B 688 (2024) 416156.

[132] H. Kafashan, Z. Orshesh, A. Bahrami, F. Zakerian, Phys. B **675 (**2024**)** 415623.

[133] S. Mustapha, M. M. Ndamitso, A. S. Abdulkareem , J. O. Tijani, D. T. Shuaib, A. K. Mohammed and A. Sumaila, Adv. Nat. Sci.: Nanosci. Nanotechnol. 10 (2019) 045013.

[134] R.L. Schoeppner, R.S. Goeke, N.R. Moody and D.F. Bahrd, Acta Mater. 91 (2015) 1.

[135] T. Bannuru, W.L. Brown, S. Narksitipan, R.P. Vinci, J. Appl. Phys. 103 (2008) 083522.

[136] N. Fuschillo, M.L. Gimpl, J. Mater. Sci. 5 (1970) 1078.

[137] A.J. Haslam, D. Moldovan, V. Yamakov, D. Wolf, S.R. Phillpot, H. Gleiter, Acta Mater. 51 (2003) 2097.

[138] F. Sansoz, V. Dupont, Appl. Phys. Lett. 89 (2006) 111901.

[139] J.M. Calleja, M. Cardona, Phys. Rev. B 16 (1977) 3753.

[140] J. Zuo, C. Xu, Y. Liu, Y. Qian, Nanostruct. Mater. 10 (1998) 1331.

[141] R. Zhang, G.P. Yin, N. Wang, L. Guo, Solid State Sci., 11 (2009) 865.

[142] A. Barranco, A. Borras, A. Gonzalez-Elipe, A. Palmero, Progr. Mater. Sci. 76 (2016) 59.

[143] M. Wang, L. Jiang, E. J. Kim, S. H. Hahn, RSC Adv. 5 (2015) 87496.

[144] V. G. Hadjiev, M. N. Iliev, I. V. Vergilov, J. Phys. C: Solid State Phys. 21 (1988) L199.

[145]U.R. Gudla, B. Suryanarayana, V. Raghavendra, K.A. Emmanuel, N. Murali, P. Taddesse, D. Parajuli, K. C. B. Naidu, Y. Ramakrishna, K. Chandramouli, Results in Physics 19 (2020) 103508.

[146] I. Matai, A. Sachdev, P. Dubey, S.U. Kumar, B. Bhushan, P. Gopinath, J. Colloids Surf. B 115 (2014) 359.

[147] D.D. Thongam, J. Gupta, N.K. Sahu, D. Bahadur, J. Mater. Sci. 53 (2018) 1110.

[148] A. Jafari, M. Ghane, S. Arastoo, African J. Microbio. Res. 5 (2011) 5465.

[149] P. Nkeng, J.F. Koening, J.L. Gautier, P. Chartier, G.J. Poillerat, Electroanal. Chem. 402 (1996) 81.

[150] H.A. Weakliem, J. Chem. Phys. 36 (1962) 2117.

[151] S.D. Birajdar, P.P. Khirade, V.R. Bhagwat, A.V. Humbe, K.M. Jadhav, J. Alloy. Compd. 683 (2016) 513.

[152] F. Pan, C. Song, X.J. Liu, Y.C. Yang, F. Zeng, Mater. Sci. Eng. R 62 (2008) 1.

[153] T. Dietl, H. Ohno, F. Matsukura, J. Cibert, D. Ferrand, Science 287 (2000) 1019.

[154] T. M. Hammad, J. K. Salem, R. G. Harrison, Appl. Nanosci. 3 (2013) 133.

[155] P.K. Giri, S. Bhattacharyya, D.K. Singh, R. Kesavamoorthy, B.K. Panigrahi, G.M. Nair, J. Appl. Phys. 102 (2007) 093515.

[156] Y. Slimani, S. Caliskan, F. A. Khan, A. Baykal, Nano-Struct. Nano-Objects 40 (2024) 101348.

[157] H. Ji, C. Cai, S. Zhou, W. Liu, J. Mater. Sci.: Mater. Electron. 29 (2018) 12917.

[158] V. V. Petrov, V. V. Sysoev, I. O. Ignatieva , I. A. Gulyaeva, M. G. Volkova, A. P. Ivanishcheva, S. A. Khubezhov, Y. N. Varzarev, E. M. Bayan, Sensors 23 (2023) 5617.

[159] L. Xu, W. Kuang , Z. Liu, F. Xian, Physica B: Cond. Matt.583 (2020) 412010.

[160] M. Wang, Y. Zhou, Y. Zhang, E.J. Kim, S.H. Hahn, S.G. Seong, Appl. Phys. Lett. 100 (2012) 101906.

[161] Z.Y. Xiao, H. Matsui, K. Katayama, K. Miyajima, T. Itoh, and H. Tabata, J. Appl. Phys. 108 (2010) 013502.

[162] J. Xu,S. Shi, L. Li, X. Zhang, Y. Wang, Q. Shi, S. Li, H. Wang, J. Electr. Mater. 42 (2013) 12.

[163] H. Cheng, K. Lin, H. Hsu, and W. Hsieh, Appl. Phys. Lett. 88 (2006) 261909.

[164] P. A. Rodnyia, K. A. Chernenkoa, I. D. Venevtseva, Optics and Spectr. 125 (2018) 372.

[165] J.R. Wijesingha, G.K.U.P. Gajanayake, W.A.V.U. Wickramasinghe et al. J. Electron. Mater. 53 (2024) 5298.

[166] R.D. Shannon, Acta Cryst. A32 (1976) 751.

[167] C.Z. Wang, Z. Chen,Y. He, L.Y. Li, D. Zhang, Appl. Surf. Sci. 255 (2009) 6881.

[168] S. H. Baek, J.J. Song, S.W. Lim, Physica B, 399 (2007) 101.

[169] K.J. Kim, and Y.R. Park, J. Appl. Phys. 96 (2004) 4150.

[170] B.E. Warren, B.L. Averbach, J. Appl. Phys. 21 (1950) 595.

[171] T. Srinivasulu, K. Saritha, K.T. Ramakrishna Reddy, Moder. Electr. Mater. 3 (2017) 76.

[172] P. Bindu, S. Thomas, J. Theor. Appl. Phys. 8 (2014) 141.

[173] K.A. Alim, V.A. Fonoberov, A.A. Balandin, Appl. Phys. Lett. 86 (2005) 053103.

[174] Z.Ž. Lazarević, Č. Jovalekić, A. Milutinović, D. Sekulić, V.N. Ivanovski, A. Rečnik, B. Cekić, N.Ž. Romčević, J. Appl. Phys. 113 (2013) 187221.

[175] A. Polyakov, Y. Govorkov, A.V. Smirnov, N.B. Pashkova, N.V. Pearton, S.J. Frazier, R.M. Abernathy, R.C. Norton, D.P. Zavada, R.G. Wilson, Mater. Sci. Semicond. Process. 7 (2004) 77.

[176] B.P. Kafle, S. Acharya, S. Thapa , S. Poudel, Ceramics International, 42 (2016) 1133.

[177] A. Parra-Palomino, O. Perales-Perez, R. Singhal, M. Tomar, Jinwoo Hwang,

P.M. Voyles, J. Appl. Phys. 103 (208) 1.

[178] Y. Ma, H. Gao, R. Huang, R. Guo, S. Yang, Y. Han, H. Zuo, J. Luminescence, 241 (2022) 118521.

[179] M.M. Ovhal, A.S. Kumar, P. Khullar, M. Kumar, A.C. Abhyankar, Mater. Chem. Phys. 195 (2017) 58.

[180] M. Cernea, V. Mihalache, E.C. Secu, R. Trusca, V. Bercu, L. Diamandescu, Superla. Microstr. 104 (2017) 362.

[181] A.A. Othman, M.A. Osman, E.M.M. Ibrahim, M.A. Ali and A.G. Abd-elrahim, Mater. Sci. Eng. B 219 (2017) 1.

[182] H.B. Ruan, L. Fang, D.C. Li, M. Saleem, G.P. Qin and C.Y. Kong, Thin Solid Films 519 (2011) 5078.

[183] H. Harsono, I. Wardana, A.A. Sonief et al. J. Nano Res. 35 (2013) 67.

[184] J.E. Ramos, M. Montero-Munoz, J.A.H. Coaquira, J. Rodriguez-Paez, J. Low Temp. Phys. DOI: 10.1007/s10909-014-1246-x.

[185] D. Toloman, A. Mesaros, A. Popa, O. Raita, T.D. Silipas, B.S. Vasile, O. Pana, L.M. Giurgiu, J. Alloys Comp.551 (2013) 502

[186] T. Ivanova, A. Harizanova, T. Koutzarova and B. Vertruyen, Superlatt. Microstruct. 70 (2014) 1.

[187] P. Abraham, S. Shaji, D.A. Avellaneda, J.A. Aguilar-Martínez, B. Krishnan, Mater. Toda. Comm. 35 (2023) 105909.

[188] S. Yang and Y. Zhang, J. Magn. Magn. Mater. 334 (2013) 52.

[189] M. Shatnawi, A.M. Alsmadi, I. Bsoul, B. Salameh, M. Mathai and G. Alnawashi, Results in Physics. 6 (2016) 1064.

[190] M. Morsy, I. Gomaa, A. Abd Elhamid, H. Shawkey, M.A. Saad Aly and A. Elzwawy, Scientific Reports 13 (2023) 21742.

[191] L.A. Adnan, N.F. Alheety, A.H. Majeed, M.A. Alheety, H. Akbas, Materials Today: Proceedings **42** (2021) 2700.

[192] D. Jaganyi, M. Altaf, I. Wekesa, Appl. Nanosci. DOI: 10.1007/s13204-012-0135-3

[193] P. Jiang, J.J. Zhou, H.F. Fang, C.Y. Wang, Z.L. Wang and S.S. Xie, Adv. Funct. Mater. 17 (2007) 1303.

[194] B.D. Naorem, J.P. Singh, B. Sharma, S. Garg, C. Athira, H. Sherin, M.M. Muskan, S. Sahu, A. Chowdhuri, M. Verma, M. Tomar, N. Batra, Chem. Phys. impact 10 (2025) 100823.

[195] W.H. Shah, A. Alam, H. Javed et al. Scientific Reports 13 (2023) 8646.

[196] M. Junaid, S.G. Hussain, N. Abbas, W. Qamar khan, Results in Chemistry 5 (2023) 100961.

[197] T.L. Tan, C.W. Lai and S.B. Abd Hamid, J. Nanomat. Article ID 371720, 6 pages (2014).

[198] D. Wu, Z. Huang, G. Yin, Y. Yao, X. Liao, D. Han, X. Huangb and J. Gu, Cryst. Eng. Comm. 12 (2010) 192.

[199] Z.N. Kayani, M. Anjum, S. Riaz, S. Naseem, T. Zeeshan, Appl. Phys. A 126 (2020) 197.

[200] E. Burstein, Phys. Rev. 93 (1954) 632.

[201] T. Moss, Proc. Phys. Soc. B 76 (1954) 755.

[202] Y. Sun, X. Gu, Y. Zhao, L. Wang, Y. Qiang, Superlatt. Microstruct. 117 (2018) 520.

[203] Q. Yu, C. Yu, H. Yang, W. Fu, L. Chang, J. Xu, R. Wei, H. Li, H. Zhu, M. Li, G. Zou, G. Wang, C. Shao, Y. Liu, Inorg. Chem. 46 (2007) 6204.

J Mater Sci: Mater Electron (2025) 36:1218

Structural and optical changes induced by the incorporation of Fe ions in ZnO matrix

R. Nettour[1] and A. Kabir[1,*]

[1] *Laboratory of Research on the Physic-Chemistry of Surfaces and Interfaces(LRPCSI), Faculty of Science, Université 20 août 1955-Skikda, PB 26 Route d'El-Hadaiek, 21000 Skikda, Algeria*

Received: 10 January 2025
Accepted: 3 July 2025

ABSTRACT

In this work, Fe ions were incorporated in the ZnO matrix using a chemical method. This method consisted of the spray of a chemical solution onto glass substrates heated at 450 °C. The chemical solution was composed of a volume of Zn-rich solution in which Fe-rich solution was added with a volume ratio varied from x = 0.00 to x = 0.10. The resulting films were characterized for their structural and optical properties by, respectively, x-ray diffraction (XRD), Raman spectroscopy, UV–visible spectroscopy, and photoluminescence spectroscopy. XRD patterns showed that the incorporation of Fe ions in the ZnO matrix did not induce changes in the material's wurtzite phase; however, it affected the structural parameters such as lattice parameters, grain size, and crystal stress. Raman spectra confirmed the presence of the ZnO phase in addition to two peaks at 646 and 690 cm^{-1} corresponding to the Fe–O vibration modes. The correlation between the E_{2H} mode-related peak area and the grain size exhibited that the enhancement of the structural properties of ZnO depended on the incorporated Fe ions form and amount. The transmittance in the visible region decreased as a function of the Fe-rich solution volume ratio. The incorporation of Fe ions decreased the band gap energy E_g from 3.45 eV for x = 0.00 to a minimum of 3.21 eV for x = 0.04. Beyond this ratio, the band gap energy stabilized around 3.27 eV. PL spectra showed the presence of ultraviolet (UV) emission and near-infrared (NIR) emission peaks. The variation of the band gap energy corresponding to the position of the UV emission peak is similar to that determined from UV–visible spectra. The decrease of the NIR emission peak intensity is attributed to the presence of Fe ions in the ZnO matrix. The optical properties of ZnO depended, like structural properties, on the incorporated Fe ion form and amount.

Address correspondence to E-mail: a.kabir@univ-skikda.dz; a.nour_kabir@yahoo.fr

https://doi.org/10.1007/s10854-025-15309-6
Published online: 12 July 2025

1 Introduction

Zinc oxide (ZnO) is a well-known n-type semiconductor material with a wide band gap energy (3.37 eV [1]). It is known for its interesting physicochemical characteristics such as piezoelectricity [2], high transparency in the visible light region [3], and ferromagnetism at ambient temperature [4]. It is extensively studied for possible application in several domains such as electronics [5–7], optoelectronics [8–10], gas sensing [11, 12], solar cells [13, 14], photocatalysis [15–17], super capacitors [18, 19], and spintronics [20–23]. In this last, ZnO is doped with transition metals (Fe, Co, Mn,) to enhance its spintronic properties. In the literature, many techniques for the elaboration of ZnO have been described. Among them, thermal oxidation [24], pulsed laser deposition [25], sol gel [26], and spray pyrolysis [27].

Like the other transition metals, the incorporation of Fe in the ZnO matrix did not improve its spintronic properties only. It also induced changes in the behavior of ZnO. Hiremath et al. [28] evidenced the enhancement of NO_2 sensing of ZnO after the incorporation of 5 at. % Fe. Pawar et al. [29] showed that the incorporation of 5 at. % Fe in ZnO increased the photocatalytic degradation of Malashite green and antibacterial activity. The effect of Fe ions on the increase of the antibacterial activity was also observed on thermally treated TiO_2–Fe_2O_3 nanocomposites [30] elaborated by a simultaneous incorporation of Fe_2O_3 and TiO_2 [31]. The incorporation of Fe in the ZnO matrix also improved the photocatalytic degradation of phenol, methylene blue, and chlorepiryfos [32]. A decrease of the band gap energy was found, by Alharchan et al. [33] when doping ZnO with low amounts of Fe. They suggested an sp-d exchange between the s-p electrons of the valence and the conduction bands and d-electrons of Fe^{3+} [33]. Seidu et al. [34] revealed an increase in the band gap energy of transition metals doped ZnO confirmed by ab-initio simulations. A slight decrease of the band gap energy was also observed by Maibam et al. [35]. They did not observe any shift of photoluminescence emission peaks in the visible region. Ma et al. [36] found that the Fe doping suppressed the green emission peak of ZnO due to the decrease of oxygen vacancies. A drop in the intensity of the green-yellow emission peak was attributed by Cernea et al. [37] to the decrease of oxygen vacancies and interstitial oxygen. The same observation was done by Ovhal et al. [38] concerning the quenching of the green emission peak accompanied by the increase of the band gap energy for 6 wt. % Fe-doped ZnO.

In this work, the dependence of the ZnO structural and optical properties on the amount of the incorporated Fe will be investigated using x-ray diffraction, Raman spectroscopy, UV–visible spectroscopy, and photoluminescence spectroscopy. ZnO samples were elaborated using spray pyrolysis which is an inexpensive and simple method for the preparation of thin layers, nanomaterials, materials oxide, and luminescent materials [39]. The aim of this work is to exhibit the effect of the incorporation of Fe ions on the structural parameters and the optical parameters. All the results will be discussed as a function of the Fe-rich solution volume ratio.

2 Experimental procedure

In this work, 0.1 M Zn-rich solution and 0.1 M Fe-rich solution were prepared by dissolving the corresponding weights of, respectively, zinc chloride ($ZnCl_2$) and iron chloride ($FeCl_2$) in a known volume of distilled water. For the incorporation of Fe ions in ZnO matrix, several volumes of Fe-rich solution v_{Fe} were added to volumes of Zn-rich solution v_{Zn} to obtain mixtures with a Fe-rich solution volume ratio $x = \frac{v_{Fe}}{v_{Zn} + v_{Fe}} = 0.00$, 0.02, 0.04, 0.06, 0.08 and 0.10. Each mixture was then, sprayed onto a heated glass substrate to form a film of a typical ZnO white transparent color. All samples were elaborated in the same conditions of substrate temperature (450 °C), spray number (160 spray), spray rate (140 mm^3/spray), spray frequency (01 spray/30 s), nozzle-substrate distance (20 cm), and nozzle-substrate angle (90°).

The effect of the incorporation of Fe ions on the structural and optical properties of the prepared ZnO samples was investigated using x-ray diffraction, Raman spectroscopy, UV–visible spectroscopy, and photoluminescence spectroscopy. The x-ray diffractometer is a Rigaku-SmartLab equipped with a monochromatic source delivering a $CuK_{\alpha 1}$ incident beam (9 kW, 1.54056 Å) in the symmetric θ–2θ geometry ranging between 20 and 60°. Raman spectra were recorded in the wavenumber range 200–900 cm^{-1} using Horiba microRaman with 632 nm laser excitation. A Shimadzu 1700 double beam spectrophotometer was used for the recording of transmittance spectra in the wavelength range 300–900 nm. Photoluminescence

(PL) spectra were recorded in the wavelength range 300–900 nm with an integration time of 500 ms, using a 355 nm excitation line of 60 mW power, given by a frequency-tripled Nd-YAG laser.

3 Results and discussion

3.1 X-ray diffraction

Figure 1a presents the XRD patterns of the resulting films from the spray, onto heated glass substrates, of the prepared mixture with Fe-rich solution volume ratio x = 0.00, 0.02, 0.04, 0.06, 0.08 and 0.10. All XRD patterns exhibit five diffraction peaks located around 31.83°, 34.56°, 36.36°, 47.68° and 56.67° attributed respectively to (100), (002), (101), (102) and (110) orientation in the hexagonal wurtzite structure of ZnO, according to the JCPDS# 36–1451 data sheet, with a preferential orientation along to (002) planes.

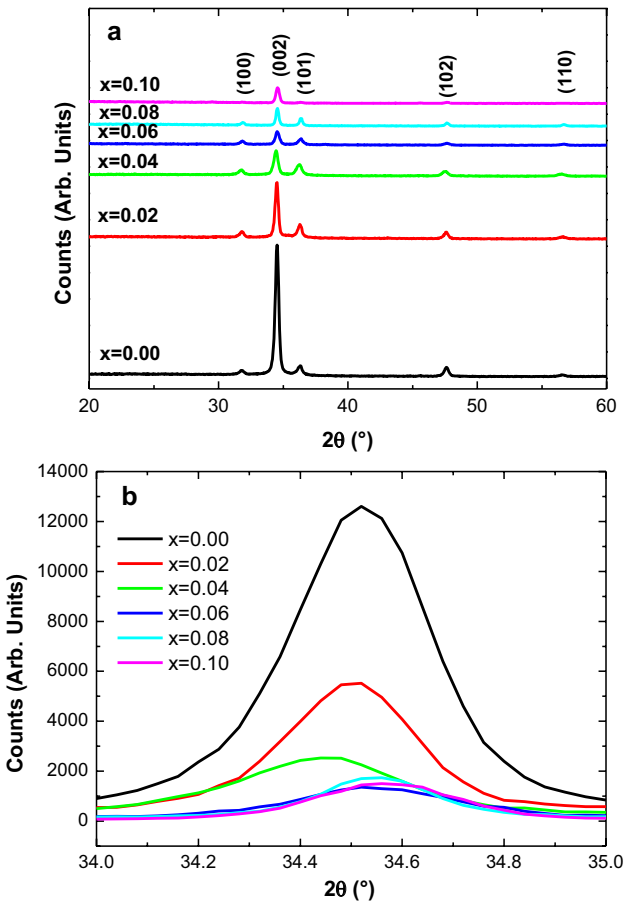

Fig. 1 **a** XRD patterns of ZnO films as a function of the Fe-rich solution volume ratio x. **b** Zoom of the (002) diffraction peak

In Fig. 1a, the intensity and the position of each diffraction peak vary from one pattern to another as a function of the Fe-rich solution volume ratio. A zoom of the (002) diffraction peak is presented in Fig. 1b to exhibit this variation that may be linked to the incorporation of Fe ions in ZnO matrix, influencing the lattice parameters. The variation of lattice parameters a and c is presented in Fig. 2, as a function of the Fe-rich solution volume ratio. The lattice parameters a and c were determined as a function of Miller indices h, k, and l, using the following relation [40]:

$$d_{hkl}^2 = \frac{3a^2c^2}{4c^2\left(h^2+hk+k^2\right)+3a^2l^2} \quad (1)$$

where d_{hkl} is the spacing between planes (hkl) and is related to the x-ray wavelength λ, the diffraction angle θ, and the diffraction order n by the Bragg's law given by [40]:

$$2d_{hkl}\sin\theta = n\lambda \quad (2)$$

The lattice parameters values, in Fig. 2, are close to those in [14]. We can see that the lattice parameters, a = 3.266 Å and c = 5.202 Å, of the sample without incorporation of Fe ions (i.e., x = 0.00) are close to those of the bulk ZnO a_0 = 3.249 Å and c_0 = 5.206 Å. The difference between these values may be due to residual stress caused by the substrate nature and/or the substrate temperature. One can see, in Fig. 2, that both lattice parameters a and c vary inversely as a function of the Fe-rich solution volume ratio. When the lattice parameter a increases from 3.266 to 3.288 Å corresponding to x = 0.04 and stabilizes after this volume

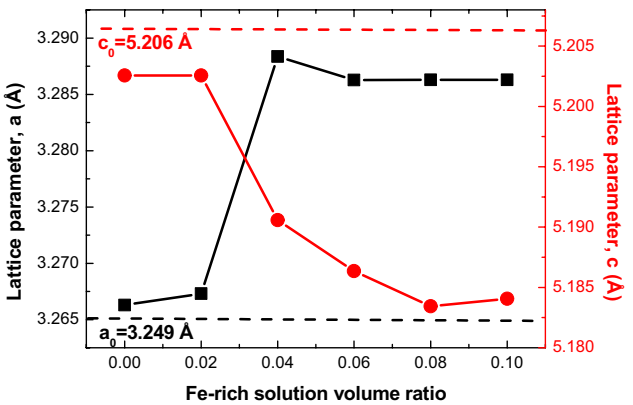

Fig. 2 Variation of lattice parameters as a function of the Fe-rich solution volume ratio

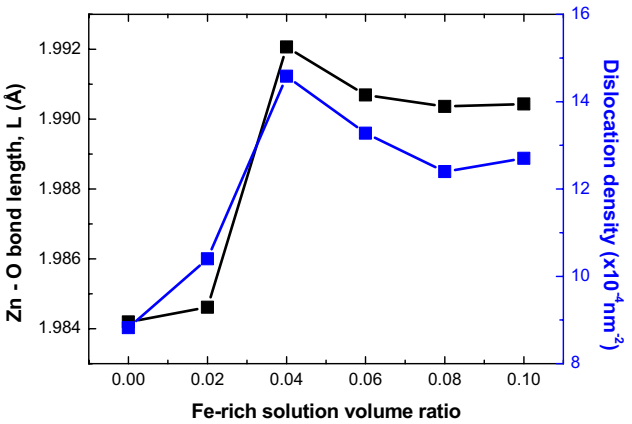

Fig. 3 Variation of Zn–O bond length and the dislocation density as a function of Fe-rich solution volume ratio

ratio around 3.285 Å, the lattice parameter c decreases from 5.202 to 5.183 Å. The variation of lattice parameters may be due to the incorporation of Fe ions in the ZnO hexagonal structure because all samples were elaborated in the same conditions. The incorporation of Fe ions induces the substitution of Zn ions by Fe ions or the positioning of Fe ions in interstitial sites in ZnO matrix, and this correlates with the variation of both Zn–O bond length and dislocation density as a function of the Fe-rich solution volume ratio (Fig. 3). The Zn–O bond length L is given by [41]:

$$L = \left[\left(\frac{a^2}{3} + \left(\frac{1}{2} - u^2\right)c^2\right)\right]^{1/2} \tag{3}$$

where $u = \frac{a^2}{3c^2} + 0.25$ the positional parameter in the wurtzite structure. The dislocation density (δ) is related to the crystallite size D by the following expression [42]:

$$\delta = \frac{1}{D^2} = \left(\frac{\beta \cos\theta}{0.9\lambda}\right)^2 \tag{4}$$

where β is the broadening of the diffraction line measured at half its maximum intensity of Gaussian fit (in radians). As can be seen in Fig. 3, both parameters, the Zn–O bond length and the dislocation density vary in the same manner as a function of the Fe-rich solution volume ratio. The Zn–O bond length values in Fig. 3 agree with those in [43]. The incorporation of Fe ions in ZnO matrix plays a major role in the variation of these two parameters. This was expected because Fe ions can incorporate the ZnO matrix in two stable forms: F^{2+} with an ionic radius of 92 pm and F^{3+} with an ionic radius of 78 pm [44]. If we compare these two radii to the radius of Zn^{2+} (88 pm [44]), we can conclude that the substitution of Zn^{2+} by Fe^{2+} will not affect the crystalline structure since they have close radii which is not the case for Fe^{3+}. It radius is smaller than that of Zn^{2+}. This suggests that the variation of lattice parameters (Fig. 2) and both Zn–O bond length and dislocation density (Fig. 3), as a function of Fe-rich solution volume ratio, is attributed to the dominance of the Fe ions present in the ZnO matrix. In Figs. 2 and 3, values corresponding to the Fe-rich solution volume ratio x = 0.02 have no significant changes compared with those corresponding to x > 0.02. This indicates that the dominant form of Fe ions in ZnO matrix, for x = 0.02, is Fe^{2+}. For the other samples, it is Fe^{3+} that dominates the incorporated Fe ions, explaining the stabilization of different parameters after x = 0.04. Wang et al. [45] found that incorporated Fe ions existed in ZnO in the form of Fe^{2+} while Baek et al. [46] found the existence of Fe^{3+} in ZnO. Kim and Park [47] found the coexistence of both Fe^{2+} and Fe^{3+} in ZnO matrix.

For the determination of the grain size and because of the difficulty of the attribution of the XRD peak broadening, like that in Fig. 1b, to the grain size or to the microstrain, we have used the modified Williamson-Hall approach given by [48]:

$$\beta_{hkl}\cos\theta_{hkl} = \frac{0.9\lambda}{D} + \frac{4\sigma \sin\theta_{hkl}}{Y_{hkl}} \tag{5}$$

The Williamson-Hall approach is modified by replacing the isotropic microstrain ε by the anisotropic microstrain $\varepsilon_{hkl} = \frac{\sigma}{Y_{hkl}}$ where σ is the crystal stress and Y_{hkl} is the Young's modulus given, as a function of lattice parameters a and c and Miller indices h, k, and l, by [49]:

$$Y_{hkl} = \frac{\left[h^2 + \frac{(h+2k)^2}{3} + \left(\frac{al}{c}\right)^2\right]^2}{s_{11}\left(h^2 + \frac{(h+2k)^2}{3}\right)^2 + s_{33}\left(\frac{al}{c}\right)^4 + (2s_{13} + s_{44})\left(h^2 + \frac{(h+2k)^2}{3}\right)\left(\frac{al}{c}\right)^2} \tag{6}$$

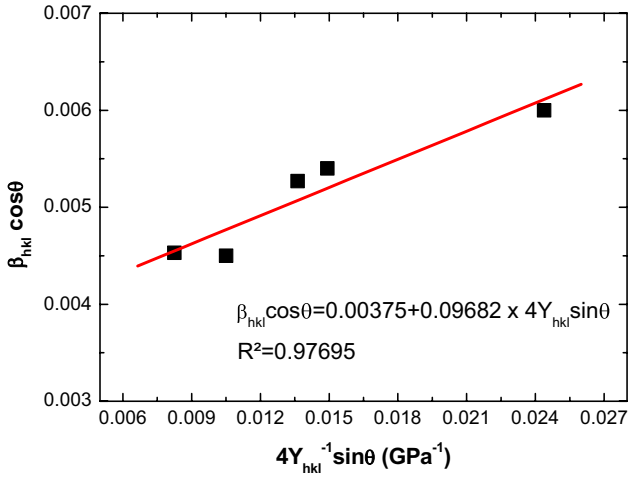

Fig. 4 Linear fit (red line) of the variation of $\beta_{hkl}\cos\theta$ as a function of $4Y_{hkl}^{-1}\sin\theta$

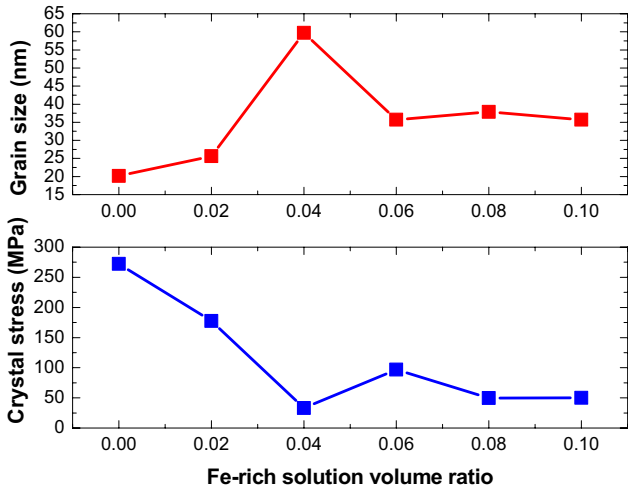

Fig. 5 Variation of the grain size and the crystal stress as a function of the Fe-rich solution volume ratio

where $s_{11} = 7.858 \times 10^{-12}$ $N^{-1}m^2$, $s_{13} = -2.206 \times 10^{-12}$ $N^{-1}m^2$, $s_{33} = 6.940 \times 10^{-12}$ $N^{-1}m^2$ and $s_{44} = 23.570 \times 10^{-12}$ $N^{-1}m^2$ are the elastic compliances of ZnO. An example of a linear fit of the plot of $\beta_{hkl}\cos\theta_{hkl}$ as a function of $\frac{4\sin\theta_{hkl}}{Y_{hkl}}$ is presented in Fig. 4. From this fit, both crystal stress σ and grain size D are determined. Figure 5 presents the variation of the crystal stress and the grain size as a function of the Fe-rich solution volume ratio. We can see that, before the incorporation of Fe ions in ZnO matrix, i.e. for x = 0.00, the grain size is 36.2 nm, which is in good agreement with results in [50], and the stress is 272 MPa comparable to that in [43] and is linked to substrate temperature and/or nature. Since

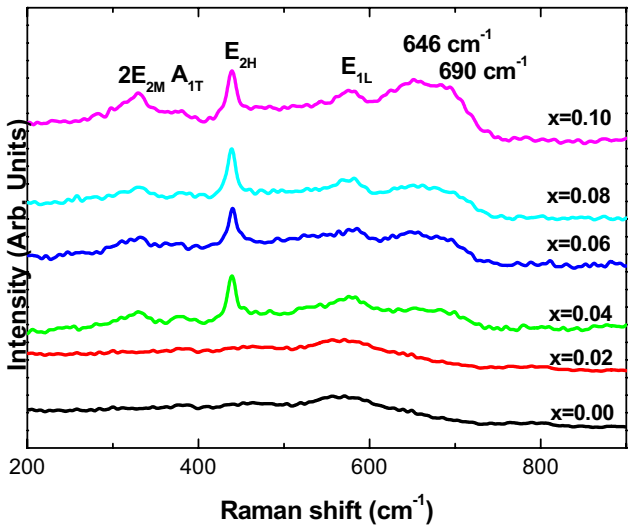

Fig. 6 Raman spectra of Fe ions incorporated ZnO

all samples were deposited onto glass substrate in the same conditions of solution molarity, number of spray and substrate temperature, the variation of both crystal stress and grain size in Fig. 5 is due to the incorporation of iron in the matrix of zinc oxide. We can see that the Fe incorporation induces firstly, an increase of the grain size to reach a maximum of 59.7 nm accompanied by a decrease of the crystal stress to a minimum value of 33.12 MPa corresponding to a Fe-rich solution volume ratio x = 0.04 and secondly, a stabilization of both the grain size and the crystal stress around 35 nm and 50 MPa, respectively, after x = 0.04 which indicates a no effect of Fe ions in ZnO matrix after this ratio.

3.2 Raman spectroscopy

Figure 6 presents Raman spectra of films deposited with a Fe-rich solution volume ratio extending from x = 0.02 to x = 0.10 in the wavelength range between 200 and 900 cm^{-1}. The spectrum of the sample deposited without Fe-rich solution (x = 0.00) is also presented. According to the group theory, the zone center of optical phonons in Wurtzite ZnO is described by the following representation [51]:

$$\Gamma = A_1 + E_1 + 2E_2 + 2B_1 \quad (7)$$

where A_1 and E_1 are polar modes which can be divided to transverse optical component (A_{1T}) and E_{1T})) and longitudinal optical component (A_{1L} and E_{1L}), E_2

consists of two modes corresponding to high (E_{2H}) and low (E_{2L}) phonons frequencies and B_1 is a silent mode.

As can be seen in Fig. 6, the Raman spectra shape varies as a function of the Fe-rich solution volume x. For the sample corresponding to x = 0.00, we can see the presence of only E_{1L} vibration mode of ZnO located around 580 cm^{-1} [52]. The same remark could be made to the sample corresponding to x = 0.02 and this reflects that there is no effect of the corresponding amount of the incorporated iron ions on the ZnO matrix. Beyond this volume ratio, i.e. from x = 0.04, we can see the appearance of additional modes of ZnO such as $2E_{2M}$ around 332 cm^{-1} (belongs to multi-phonons process [53]), A_{1T} around 380 cm^{-1} [54], E_{2H} around 435 cm^{-1} [54] and a broad peak containing two peaks around 646 and 690 cm^{-1} relatable to the vibrations of Fe–O according to [55] and we agree with this assumption since the intensity of these two peaks increase as a function of the Fe-rich solution volume ratio as cans be seen in Fig. 6. One can see that, from x = 0.04, the peak related to the E_{2H} mode, which correspond to the vibration of zinc sub-lattice [54], dominates the other ZnO related peaks without any shift which reflects that the incorporation of iron ions into ZnO matrix contributes to the enhancement of the quality of the crystalline structure, and it is confirmed by the correlation between the grain size and the E_{2H} related peak area in Fig. 7. Zuo et al. [56] reported that the Raman peaks broadening are mainly due to grain size effect. The E_{2H} peak area was determined after a decomposition of the Raman spectrum into Gaussian peaks by taking into consideration all present modes in this frequency range (Inset of Fig. 7).

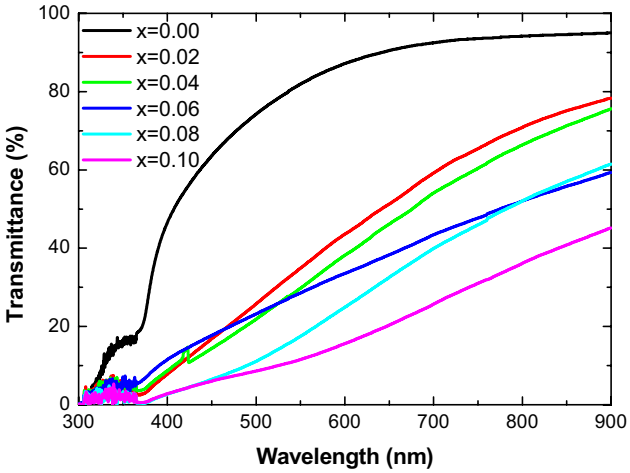

Fig. 8 UV–visible spectra of Fe ions incorporated ZnO

3.3 UV–visible spectroscopy

Figure 8 presents the UV–visible spectra of the elaborated films using Fe-rich solution volume ratios from x = 0.02 to x = 0.10. The spectrum of the sample with the ratio x = 0.00 is also presented. We can see, in Fig. 8, that the shape of spectra changes as a function of the Fe-rich solution volume ratio, which indicates that the incorporation of the Fe ions influences the optical transmittance and also the band gap energy of the elaborated ZnO

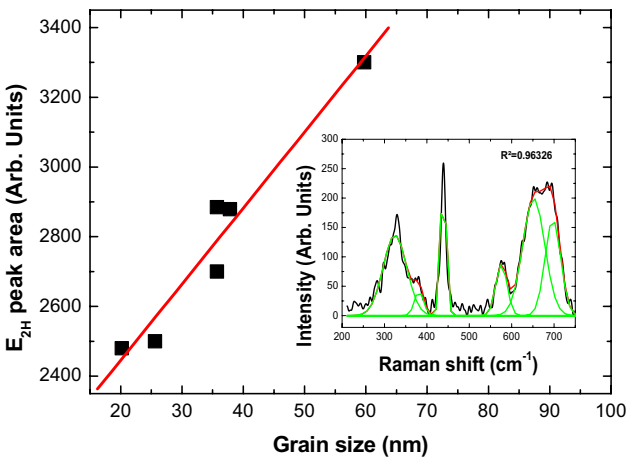

Fig. 7 Correlation between the grain size and the E_{2H} related peak area (Red line to guide the eyes). (Inset: Example of a deconvolution of a Raman spectrum)

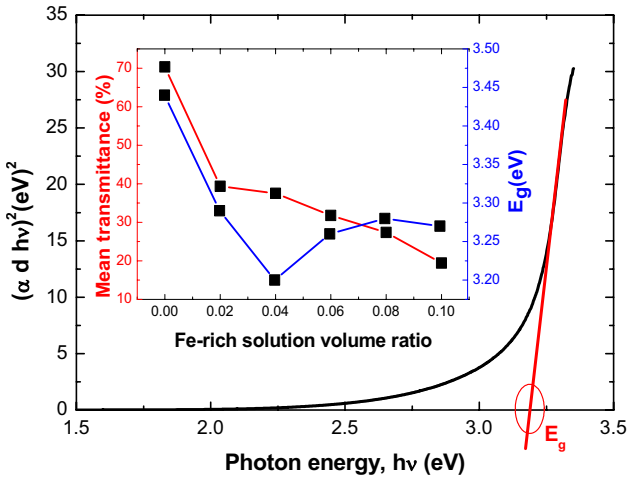

Fig. 9 Plot of $(\alpha h\nu)^2$ vs. hν. (Inset: Variation of the mean transmittance and the band gap energy as a function of the Fe-rich solution volume ratio)

samples. The band gap energy is determined graphically from the extrapolation of the linear part of the curve $(\alpha\ d\ h\nu)^2$, as a function of hν, up to the abscissa corresponding to $(\alpha\ d\ h\nu)^2 = 0$ (Fig. 9). This curve was traced using the Tauc's law, for allowed direct transitions, given by [57]:

$$\alpha h\upsilon = A(h\upsilon - E_g)^{1/2} \tag{8}$$

where $\alpha = -\frac{1}{d}\ln\frac{T}{100}$ is the absorption coefficient (in cm^{-1}) expressed as a function of the thickness d and the transmittance T (in %). The variation of both the band gap energy E_g and the mean transmittance in the visible region is traced in the inset of Fig. 9 as a function of the Fe-rich solution volume ratio. We cans see that the mean transmittance in the visible spectral region, i.e. between 800 and 400 nm rapidly decreases from 70.3% for x = 0.00 to 39.4% for x = 0.02 due to the d-d transition of Fe ions, according to Polyakov et al. [58]. Kafle et al. [59] found that the transmittance of Fe-doped ZnO decreased by 10% when Fe ion's concentration reached 4 at. %. After x = 0.02, one can see the proportionality between the decrease of the mean transmittance and the increase of the incorporated Fe ions in ZnO. In the inset of Fig. 9, the band gap energy E_g = 3.45 eV corresponding to x = 0.00 is greater than that of the bulk ZnO (3.37 eV) however, it is comparable to those in [59]. The variation of the band gap energy E_g, as a function of the Fe-rich solution volume ratio, correlates with that of the grain size (Fig. 5) in good agreement with results in [50]. We can see that the incorporation of Fe ions decreases the band gap energy of the prepared samples from 3.45 eV to the lowest value of 3.21 eV, corresponding to x = 0.04. After this ratio, we can see that the band gap energy E_g slightly increases and keeps invariant around 3.27 eV. According to Parra-palomino et al. [60], the band gap energy decrease is attributed to a change of the Fermi energy state by lowering the minimum of the conduction band and raising the maximum of the valence band, inducing band gap reduction. The change of the Fermi energy state is caused by the 3d transition of incorporated Fe^{2+} in ZnO [60]. If Fe^{3+} is the dominant form of incorporated Fe ions, they will provide free carriers, causing the Fermi level to bring closer to the conduction band, leading to the band gap enlargement [50]. This reinforces our suggestion concerning the dominance of Fe^{2+} in low ratios ($x \le 0.04$) and the dominance of Fe^{3+} in high ratios ($x > 0.04$).

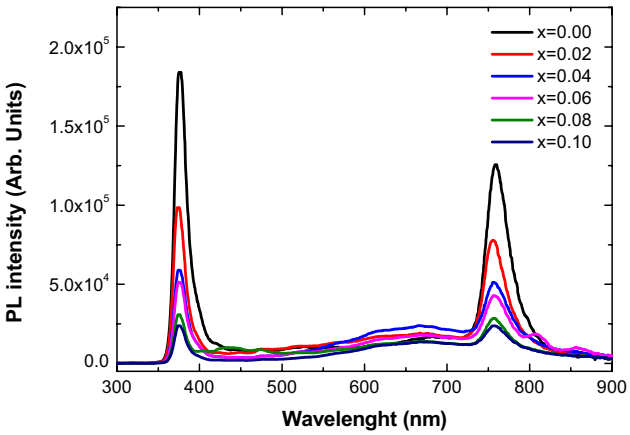

Fig. 10 PL spectra of Fe ions incorporated ZnO

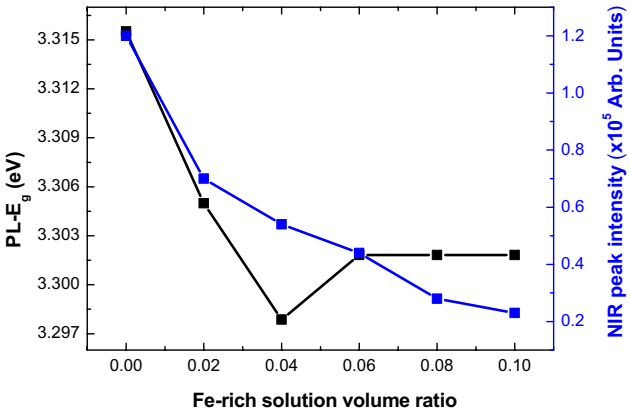

Fig. 11 Variation of PL-Eg and NIR emission peak surface as a function of the Fe-rich solution volume ratio

3.4 PL spectroscopy

PL spectra of the zinc oxide film and zinc oxide films incorporated with different amounts of Fe ions are presented in Fig. 10. All spectra have the same shape with two dominant emission peaks: Ultraviolet (UV) emission in the wavelength range 350–420 nm and near infrared (NIR) emission in the wavelength range 720–800 nm. The ultraviolet (UV) emission is generally linked to the creation, by photostimulation, of excitons of energies near the ZnO band edge. The decrease of this emission peak may be explained by the decrease of the probability of excitons creation induced by the incorporation of Fe ions in ZnO matrix. The variation of the band gap energy deduced from the position of UV emission peaks PL-E_g is traced in Fig. 11 as a function of the Fe-rich solution volume ratio. We can see that this

variation is similar to that of the band gap energy determined from UV–visible spectra (Inset of Fig. 9). The quite difference of the PL-E_g values compared with those determined from UV–visible spectra may be due to the presence of point defects, such as oxygen vacancies (V_O) and zinc interstitials (Zn_i), detected by the PL technique [61]. The near infrared (NIR) emission peak was also found by Wang et al. [62] around 1.64 eV. They attributed this emission to the donor–acceptor transition between V_O and zinc vacancies (V_{Zn}) and/or the radiative recombination of trapped electrons with trapped holes in oxygen interstitial (O_i) [62]. The variation of the NIR emission peak intensity as a function of the Fe-rich solution volume ratio is presented in Fig. 11. The decrease of the NIR emission peak is directly related to the incorporated Fe ions in the ZnO matrix. It has been reported that the incorporation of Fe ions in ZnO suppressed the green [36, 38] and the yellow-green [37] emissions.

4 Conclusion

The effect of the incorporation of Fe ions in the structural and optical properties of ZnO was investigated using XRD, Raman spectroscopy, UV–visible spectroscopy, and PL spectroscopy. The incorporation of Fe ions in ZnO matrix was done by spraying onto heated glass substrates a Zn-rich solution in which is added a Fe-rich solution with volume ratios from x = 0.00 to x = 0.10. XRD revealed the presence of the wurtsite hexagonal structure of ZnO. The variation of the crystalline parameters as a function of the Fe-rich solution volume ratio indicated an enhancement of the crystalline properties from x = 0.02 to x = 0.04 followed by a stabilization after 0.04. Raman spectra showed the presence of optical phonon vibration modes of ZnO in addition to two other peaks located at 646 and 690 cm^{-1} attributed to Fe–O vibration modes. The correlation between the grain size and the E_{2H} peak area indicated the same manner of action of incorporated Fe ions in enhancing ZnO structure. The mean transmittance in the visible region, determined from UV–visible spectra, decreased with the increasing Fe-rich solution volume ratio and the band gap energy E_g decreased to reach a lowest value of 3.21 eV for x = 0.04 before stabilizing around 3.27 eV after this ratio. PL spectra exhibited two intense peaks corresponding to UV and NIR emissions. The variation of the band gap energy PL-E_g as a function of the Fe-rich solution volume ratio is similar to that determined using UV–visible spectroscopy. The decrease of the NIR emission peak intensity was attributed to the incorporated Fe ions. The obtained results evidenced the structural and optical properties of ZnO dependence on the form and the amount of incorporated Fe ions.

Acknowledgements

Authors thank Miss Nora Abdennouri from the department of chemistry (Faculty of Sciences, University of Skikda) for her help during the solutions preparation. Special thanks to Dr. G. Schmerber, from IPCMS, for the structural and optical measurements.

Author contribution

All authors read and approved the final manuscript.

Funding

No funding was received to assist with the preparation of this manuscript.

Data availability

Data supporting this study are included within the manuscript.

Declarations

Competing interests The authors have no relevant financial interests to disclose.

Ethical approval No funding was received to assist with the preparation of this manuscript.

References

1. E.F. Keskenler, G. Turgut, S. Doğan, Superl. Microstr. **52**, 107 (2012)
2. B. Kumar, S.-W. Kim, Nano Energy **1**, 342 (2012)

3. M. Baneto, A. Enesca, Y. Lare, K. Jondo, K. Napo, A. Duta, Ceram. Int. **40**, 8397 (2014)
4. D. Gao, Z. Zhang, J. Fu, Y. Xu, J. Qi, D. Xue, J. Appl. Phys. **105**, 113928 (2009)
5. D. Li, W. Liu, J. Zong, J. Wei, G. Tan, Q. Yuan, A. Xia, D. Liu, Ceram. Int. **50**, 39391 (2024)
6. P. Supraja, R.R. Kumar, S. Mishra, D. Haranath, P.R. Sankar, K. Prakash, N. Jayarambabu, T.V. Rao, K.U. Kumar, Sens. Actuators, A **335**, 113368 (2022)
7. T. Yang, H. Pan, G. Tian, B. Zhang, D. Xiong, Y. Gao, C. Yan, X. Chu, N. Chen, S. Zhong, L. Zhan, W. Deng, W. Yang, Nano Energy **72**, 104706 (2020)
8. D. Domyati, Mater Sci: Mater Electron **35**, 406 (2024)
9. N. Dinujaya, D.L. Isuri Yasara, A.R. Kumarasinghe, T.N.B. Etampawala, MRS Adv. **9**, 1383 (2024)
10. L.H. Kathwate, V.D. Mote, J. Electron. Mater. **51**, 6894 (2022)
11. F.M. Davoodi, S.M. Rozati, S. Soltani, Appl. Phys. A **130**, 866 (2024)
12. Y. Zhang, Z. Dong, H. Jia, Bull. Mater. Sci. **46**, 180 (2023)
13. H. Abdullah, K.J. Xian, K.C. Ying et al., Appl. Sol. Energy **60**, 461 (2024)
14. J.R. Wijesingha, G.K.U.P. Gajanayake, W.A.V.U. Wickramasinghe et al., J. Electron. Mater. **53**, 5298 (2024)
15. N.S. Choudhari, R.U. Mene, P.P. Bardapurkar et al., Appl. Phys. A **130**, 874 (2024)
16. T.H. Nguyen, T.T. Mai, T.P. Tran et al., J. Sol-Gel Sci. Technol. **110**, 319 (2024)
17. A. Abutaleb, S. Ahmed, M. Imran, Eur. Phys. J. Plus **138**, 1046 (2023)
18. D. Anbuselvan, G. Anitha, S. Nilavazhagan et al., Eur. Phys. J. Plus **139**, 1054 (2024)
19. M. Kumar, J.C. Dhar, J. Mater. Sci. Mater. Electron. **35**, 1362 (2024)
20. I. Naeem, F. Baig, H.M. Fahad, S. Raza, Ionics **30**(5), 2989–3002 (2024)
21. M.A. Mahmood, K. Althubeiti, S.S. Abdullaev et al., J. Mater. Sci. Mater. Electron. **34**, 1784 (2023)
22. I. Bouanane, A. Kabir, D. Boulainine et al., J. Electron. Mater. **45**, 3307 (2016)
23. S.N. Anitha, I. Jayakumari, J. Nanosci. Nanotechno. **1**, 26 (2015)
24. V. Yepuri, S. Sigamani, V. Swaminadham, J. Sol-Gel Sci. Technol. **113**(3), 708–716 (2025)
25. S.S. Yadav, N. Pothukanuri, S. Begum et al., J. Mater. Sci. Mater. Electron. **35**, 1959 (2024)
26. M.V. Hiremath, N. Momin, M.V. Kangralkar et al., J. Korean Phys. Soc. **85**, 772 (2024)
27. A.R. Pawar, K.R. Shaikh, A.D. Salmote et al., J. Mater. Sci. Mater. Electron. **34**, 2271 (2023)
28. A.P. Amosov, V.A. Novikov, E.M. Kachkin et al., Int. J Self-Propag. High-Temp. Synth. **32**, 288 (2023)
29. O. Baytar, A. Ekinci, S. Kutluay et al., J. Aust. Ceram. Soc. **60**, 1697 (2024)
30. T. Ahmed, T. Farooq, K. Ahmed, M.A. Rehman, M. Yasir, S. Butt, M.A. Basit, Coll. Surf. A: Physico. Eng. Asp. **691**, 133850 (2024)
31. U. Qamar Satti et al., Coll. Surf. A: Physico. Eng. Asp. **671**, 131662 (2023)
32. S.L. Ezung, M. Baruah, S. Sharma, R.S. Umdor, I.T. Longchar, B. Giridharan, U.B. Sinha, D. Sinha, J. Molec. Struc. **1319**, 139434 (2025)
33. G.A. Alharshan, S. Hassaballa, M.A.M. Uosif et al., J. Supercond. Nov. Magn. **37**, 1871 (2024)
34. A. Seidu, M. Egblewogbe, G. Gebreyesus et al., MRS Adv. **3**, 2643 (2018)
35. B. Maibam, S. Baruah, S. Kumar, SN Appl. Sci. **2**, 1712 (2020)
36. Y. Ma, H. Gao, R. Huang, R. Guo, S. Yang, Y. Han, H. Zuo, J. Luminescence **241**, 118521 (2022)
37. M. Cernea, V. Mihalache, E.C. Secu, R. Trusca, V. Bercu, L. Diamandescu, Superla. Microstr. **104**, 362 (2017)
38. M.M. Ovhal, A.S. Kumar, P. Khullar, M. Kumar, A.C. Abhyankar, Mater. Chem. Phys. **195**, 58 (2017)
39. M. Inada, J. Hojo, Adv. Powder Technol. **33**, 103647 (2022)
40. B. Dennis, Elements of X-ray Diffraction, (third ed. Prentice-Hall International, Upper Saddle River, N.J, London, 2000)
41. C.S. Barret, T.B. Massalski, *Structure of metals* (Pergamon Press, Oxford, 1980)
42. M. Saleem, L. Fang, H.B. Ruan, F. Wu, Q.L. Huang, C.L. Xu, C.Y. Kong, Intl. J. Phy. Sci. **7**(23), 2971 (2012)
43. P. Bindu, S. Thomas, J. Theor. Appl. Phys. **8**, 141 (2014)
44. R.D. Shannon, Acta Cryst. **A32**, 751 (1976)
45. C.Z. Wang, Z. Chen, Y. He, L.Y. Li, D. Zhang, Appl. Surf. Sci. **255**, 6881 (2009)
46. S.H. Baek, J.J. Song, S.W. Lim, Phys. B **399**, 101 (2007)
47. K.J. Kim, Y.R. Park, J. Appl. Phys. **96**, 4150 (2004)
48. T. Pandiyarajan, B. Karthikeyan, J. Nanopart. Res. **14**, 647 (2012)
49. B.E. Warren, B.L. Averbach, J. Appl. Phys. **21**, 595 (1950)
50. T. Srinivasulu, K. Saritha, K.T. Ramakrishna Reddy, Moder. Electr. Mater. **3**, 76 (2017)
51. S. Ben Yahiaa, L. Znaidia, A. Kanaeva, J.P. Petitet, Spectrochim. Acta Part A **71**, 1234 (2008)
52. K.A. Alim, V.A. Fonoberov, A.A. Balandin, Appl. Phys. Lett. **86**, 053103 (2005)
53. J.M. Calleja, M. Cardona, Phys. Rev. B **16**, 3753 (1977)
54. R. Zhang, G.P. Yin, N. Wang, L. Guo, Solid State Sci. **11**, 865 (2009)

55. Z.Ž Lazarević, Č Jovalekić, A. Milutinović, D. Sekulić, V.N. Ivanovski, A. Rečnik, B. Cekić, N.Ž Romčević, J. Appl. Phys. **113**, 187221 (2013)
56. J. Zuo, C. Xu, Y. Liu, Y. Qian, Nanostruct. Mater. **10**, 1331 (1998)
57. J.I. Pankove, *Optical processing in semiconductors* (Dover, New York, 1971)
58. A. Polyakov, Y. Govorkov, A.V. Smirnov, N.B. Pashkova, N.V. Pearton, S.J. Frazier, R.M. Abernathy, R.C. Norton, D.P. Zavada, R.G. Wilson, Mater. Sci. Semicond. Process. **7**, 77 (2004)
59. B.P. Kafle, S. Acharya, S. Thapa, S. Poudel, Ceram. Int. **42**, 1133 (2016)
60. A. Parra-Palomino et al., J. Appl. Phys. **103**, 1 (2008)
61. P.K. Giri, S. Bhattacharyya, D.K. Singh, R. Kesavamoorthy, B.K. Panigrahi, G.M. Nair, J. Appl. Phys. **102**, 093515 (2007)
62. M. Wang, Y. Zhou, Y. Zhang, E.J. Kim, S.H. Hahn, S.G. Seong, Appl. Phys. Lett. **100**, 101906 (2012)

Micro and Nanostr ct res 207 (2025) 208271

Contents lists available at ScienceDirect

Micro and Nanostructures

journal homepage: www.journals.elsevier.com/micro-and-nanostructures

Structural, optical and luminescence characterization of Co-doped ZnO thin films

R. Nettour [a], A. Kabir [a,*], A. Erdoğmuş [b], Ö.D. Kutlu [b], G. Schmerber [c]

[a] LRPCSI, Faculty of Science, Université 20 août 1955-Skikda, PB 26 Route d'El-Hadaiek, Skikda, 21000, Algeria
[b] Department of Chemistry, Yildiz Technical University, Esenler, 34210, Istanbul, Turkey
[c] IPCMS, UMR 7504 CNRS-UdS, 23 rue du Loess, B.P. 43, Cedex 2, 67034, Strasbourg, France

ARTICLE INFO

Keywords:
Co-doped ZnO
Co molar ratio
Surface adsorption
Band gap energy
Deep level defects

ABSTRACT

Co inclusion in ZnO induced changes of structural and optical properties was studied using X-ray diffraction (XRD), Raman spectroscopy, ATR-FTIR spectroscopy, UV–Visible spectroscopy and photoluminescence spectroscopy (PL) respectively. As a function of Co molar ratio x in the precursor solution, XRD patterns of corresponding samples revealed a change of crystalline parameters of ZnO from x = 0.06. The appearance of Co_3O_4 and $Zn(OH)_2$ secondary phases, for x = 0.10, suggested a slowdown of the reaction of the formation of ZnO induced by Co inclusion. These results were evidenced by Raman spectroscopy and ATR-FTIR spectroscopy. This last also revealed the enhancement of ZnO surface adsorption of CO_2 and H_2O after Co inclusion. As a function of Co molar ratio, the mean transmittance in the visible light region decreased from 70.33 % to 23.25 % and the band gap energy E_g decreased from 3.45 to 2.67 eV for x = 0.08. The increase of the band gap energy for x = 0.10 may be caused by the decrease of sp-d exchange interactions induced by the formation of Co_3O_4 and $Zn(OH)_2$ phases. Except for x = 0.10, all PL spectra, presented an ultraviolet emission peak around 375 nm and a near infrared emission peak around 754 nm. The intensity of these two emission peaks decreased, as a function of Co molar ratio, to completely disappear, for x = 0.10, leading the place to a red emission peak around 697 nm, attributed to Co-based impurities, and other peaks, between 400 and 562 nm, attributed to deep level defects in ZnO. These results make this material suitable for use in the spintronics domain, in gas sensing devices, light emitting diodes (LED) and solar cells.

1. Introduction

Zinc oxide (ZnO) has attracted many researchers for its remarkable characteristics such as big binding excitation energy (60 meV [1]), n-type conduction, wide band gap energy at room temperature (3.37 eV [1]), piezoelectricity [2], high transparency in the visible light region [3], and ferromagnetism [4]. It is intensively studied for applications in several domains such as electronics [5], opto-electronics [6], gas sensing [7], solar cells [8], photocatalysis [9], and supercapacitors [10]. Many techniques, for the elaboration of different forms of ZnO, have been described in literature such as sol gel [11], thermal evaporation [12], RF sputtering [13], spray pyrolysis [14], organometallic precursor method [15], microemulsion process [16], and co-precipitation method [17]. It is to be

* Corresponding author. Laboratory of Research on the Physic-Chemistry of Surfaces and Interfaces (LRPCSI), Faculty of Science, Université 20 août 1955-Skikda, Algeria.
E-mail addresses: a.kabir@univ-skikda.dz, a.nour_kabir@yahoo.fr (A. Kabir).

https://doi.org/10.1016/j.micrna.2025.208271
Received 12 May 2025; Received in revised form 12 July 2025; Accepted 13 July 2025
Available online 14 J ly 2025

noticed that the interesting characteristics of ZnO are strongly influenced by the elaboration method. For example, a broad emission peak in the visible region was observed in ZnO deposited by thermal evaporation [12] while red emission was observed in sol gel-deposited ZnO [11] and green emission in RF sputtering-deposited ZnO [13]. Even for the same elaboration technique; experimental conditions play an important role in controlling the physic-chemical properties of ZnO. For example, the spray pyrolysis technique, used in this work for samples elaboration, is an inexpensive and a simple method for the preparation of thin films, nanomaterials, oxide materials and luminescent materials [18]. The preferential orientation of ZnO thin films deposited using this method was found by Suarez et al. [19] along (002) plane while (100) was found by Dimitrov et al. [20] and (101) was evidenced by Pawar et al. [14]. The (101) orientation was also found, by Saadi et al. [21], in Co-doped ZnO nanoparticules elaborated using co-precipitation method.

In order to improve its interesting properties, ZnO has been successfully doped with metals such as Al [22] for use as a transparent electrode in solar cells, with rare earth such as Er [23] for use in light emitting diodes, and with transition metals such as Co [24] for a use as a diluted magnetic semiconductor (DMS) also termed diluted magnetic oxide (DMO) [25]. A theoretical study predicted that ferromagnetism was stable for wide band gap semiconductors such as ZnO and the Curie temperature can be increased for p-type DMS [26]. Another theoretical study demonstrated that doping ZnO with Ni, Fe, Co, Cr, and V exhibited ferromagnetism ordering while doping it with Ti and Cu exhibited paramagnetic state [27]. These studies opened a way for successful experimental research on transition metals-doped ZnO resulted in Co-doped ZnO with ferromagnetic ordering at room temperature [28]. However, improving magnetic properties of ZnO by transition metals doping influences its other interesting characteristics especially the optical one. Co was a candidate element for improving ZnO optical properties in addition to magnetic properties due to its solubility and its abundant electron-states. Ji et al. [29] found that the inclusion Co in ZnO decreased the band gap energy. According to Mahroug et al. [30], the decrease of the band gap energy was accompanied with the appearance of $Zn_xCo_{3-x}O_4$ secondary phase and a decrease of the visible emission. Co inclusion reduced defects concentration was also evidenced by Akcan [31]. According to literature, desirable and undesirable effects of Co inclusion in ZnO depend directly on the Co concentration [29–31].

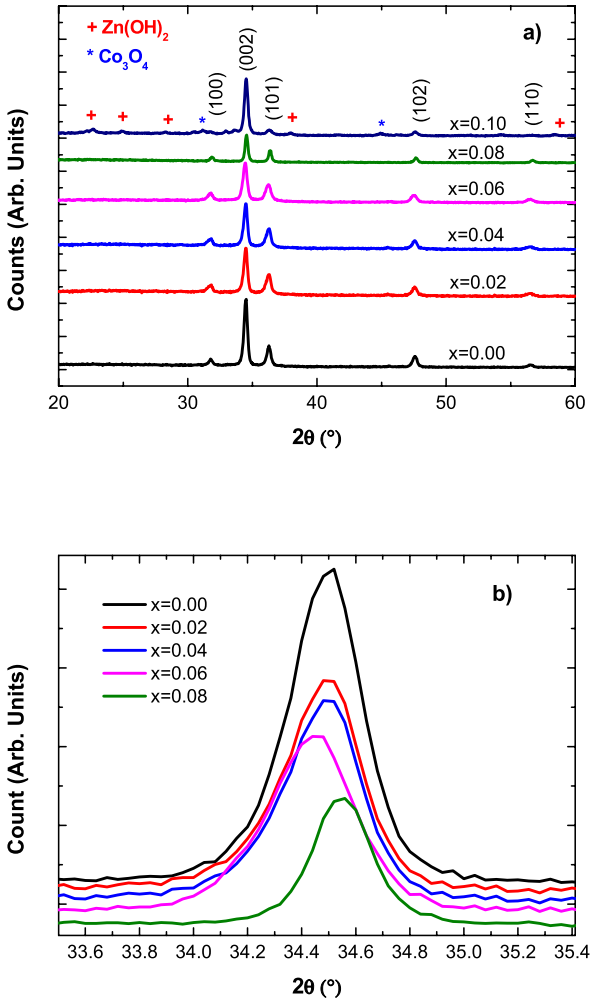

Fig. 1. a) XRD patterns of ZnO films as a function of Co molar ratio. b) Zoom of the (002) diffraction peak.

In this work, and in order to exhibit additional effects of Co inclusion on the structural and the optical parameters, Co-doped ZnO films were deposited onto glass substrates using the spray pyrolysis method. Effects of Co inclusion in ZnO will be investigated using X-ray diffraction, Raman spectroscopy, ATR-FTIR spectroscopy, UV–Visible spectroscopy, and photoluminescence spectroscopy. All characterization results will be presented and discussed as a function of Co molar ratio.

2. Experimental details

In this work, 0.1 M Zn-based solution and 0.1 M Co-based solution were prepared by dissolving the corresponding weight of, respectively, zinc(II) chloride ($ZnCl_2$) and cobalt(II) chloride ($CoCl_2$) in distilled water. For the preparation of the precursor solution, several volumes of Co-based solution v_{Co} were added to other volumes of Zn-based solution v_{Zn} to obtain mixtures with a Co molar ratio $x = \frac{n_{Co}}{n_{Zn}+n_{Co}} = \frac{v_{Co}}{v_{Zn}+v_{Co}} = 0.00$, 0.02, 0.04, 0.06, 0.08 and 0.10 where n_{Zn} and n_{Co} are the number of moles of Zn and Co respectively. For each molar ratio, the corresponding mixture was sprayed onto a glass substrate heated at 450 °C. The spray number was 160 sprays with a rate of 140 mm^3 per spray and the spray frequency was 01 spray per 30 s. The distance between the nozzle and the substrate distance was 20 cm and the nozzle-substrate angle was 90°.

The structural and optical characterization of the prepared samples was done using X-ray diffraction, Raman spectroscopy, UV–Visible spectroscopy, FTIR-ATR spectroscopy, and photoluminescence spectroscopy. The X-ray diffractmeter is a Rigaku-SmartLab equipped with a monochromatic source delivering a $CuK_{\alpha 1}$ incident beam (9 kW, 1.54056 Å) in the symmetric θ-2θ geometry ranging between 20° and 60°. Raman spectra were recorded, in the wavenumber range 200–900 cm^{-1}, using Horiba microRaman with 632 nm laser excitation. A Shimadzu 1700 double beam spectrophotometer was used for the recording of transmittance spectra in the wavelength range 300–900 nm. ATR-FTIR spectra were recorded using a PerkinElmer Spectrum One Spectrometer in the wavenumber range 1300-560 cm^{-1} with a resolution of 2 cm^{-1}. Photoluminescence (PL) spectra were recorded in the wavelength range 300–900 nm with an integration time of 500 ms, using 355 nm excitation line of 60 mW power, given by a frequency-tripled Nd-YAG laser.

3. Results and discussion

3.1. -ray diffraction

XRD patterns of films deposited by spraying mixtures, corresponding to Co molar ratios varied from x = 0.00 to x = 0.10, onto heated glass substrates are presented in Fig. 1-a. Except for the pattern corresponding to x = 0.10, we can see the presence of five diffraction peaks in the remaining patterns. According to the JCPDS# 36–1451 data sheet [32], these peaks, located around 31.83°, 34.56°, 36.36°, 47.68° and 56.67° are attributed respectively to (100), (002), (101), (102), and (110) orientations of the hexagonal wurtzite structure of ZnO. We can see that all samples have the same preferential orientation along to (002) planes. The preferential orientation can be defined by means of the texture coefficient TC for each orientation (hkl) which is calculated using a relation given by Ref. [33]:

$$TC_{(hkl)} = \frac{I_{(hkl)} \times I_{ref(hkl)}^{-1}}{\left[(1/n)\Sigma\left(I_{(hkl)} \times I_{ref(hkl)}^{-1}\right)\right]} \quad (1)$$

where $I_{(hkl)}$ is the (hkl) corresponding peak intensity, $I_{ref\ (hkl)}$ is the (hkl) corresponding peak intensity in the reference pattern (Took from the JCPDS# 36–1451 data sheet [32]), and n is the number of diffraction peaks in the samples pattern. The calculated texture coefficient for all orientations present in XRD patterns is regrouped in Table 1. We can see, in Table 1, that the higher values of the texture coefficient correspond to the (002) orientation which indicates that it is the preferential orientation according to Rao and Santhoshkumar [33]. For Co molar ratio x = 0.10, we can see the disappearance of (100) and (110) corresponding peaks and the appearance of weak peaks corresponding to $Zn(OH)_2$ and Co_3O_4 phases according to the data sheets JCPDS#41–1359 [32] and JCPDS#43–1003 [32] respectively. The Co_3O_4 secondary phase was also obtained by other researchers like Ivill et al. [34] and Sundararaj et al. [35]. They found that the increase of the Co ratio reduced gradually the crystalline quality of ZnO before the appearance of the Co_3O_4 secondary phase. The decrease of the (002) peak intensity, with the increase of Co molar ratio from x = 0.00 to x = 0.08, observed in Fig. 1-b is in good agreement with their results. The decrease of XRD peaks, for Co molar ratios from x = 0.02 to x = 0.08, and the simultaneous appearance of Co_3O_4 and $Zn(OH)_2$ secondary phases, for Co molar ratio x = 0.10, indicates that the progressive inclusion of Co also slowed down the reaction of the formation of ZnO phase.

Table 1
Texture coefficient of ZnO films as a function of Co molar ratio.

Co molar ratio	(100)	(002)	(101)	(102)	(110)
0.00	0.23	3.24	0.34	1.09	0.09
0.02	0.43	2.93	0.53	1.02	0.09
0.04	0.35	2.82	0.51	1.10	0.22
0.06	0.35	2.70	0.54	1.09	0.32
0.08	0.32	2.68	0.54	1.08	0.38
0.10	–	4.25	0.10	0.65	–

The shift of the (002) diffraction peak (Fig. 1-b) confirms the substitution of Co ions into the ZnO host lattice. The substitution of Co ions into ZnO host may induce lattice distortion regarding the difference between the ionic radius of Zn^{2+} (0.06 nm) and Co^{2+} (0.058 nm) [36,37]. Values of the lattice parameters a and c and the directional strain ε_a and ε_c determined from XRD patterns are regrouped, in Table 2, for all samples. The lattice parameters a and c were determined using the following relation [38]:

$$d_{hkl}^2 = \left(\frac{n\lambda}{2\sin\theta}\right)^2 = \frac{3a^2c^2}{4c^2\left(h^2+hk+k^2\right)+3a^2l^2} \tag{2}$$

where h, k, and l are Miller indices, d_{hkl} is the inter-reticular distance, λ is the X-ray wavelength, θ is the diffraction angle and n the diffraction order. The directional strain ε_a and ε_c (in %) are given, as a function of the film lattice parameters a and c and the bulk lattice parameters a_0 and c_0, by the following relation [38]:

$$\varepsilon_a = \frac{a-a_0}{a_0}\times 100 \tag{3}$$

$$\varepsilon_c = \frac{c-c_0}{c_0}\times 100 \tag{4}$$

In Fig. 2, is traced the variation of the lattice parameters a and c as a function of Co molar ratio x. We can see that the lattice parameters values a = 3.251 Å and c = 5.204 Å of the sample elaborated without Co inclusion (i.e. x = 0.00) are quite different from those of the bulk ZnO a_0 = 3.249 Å and c_0 = 5.206 Å. This difference may be due to residual stress induced by the substrate temperature and/or the substrate nature [39]. It is about compressive stress along the c direction referring to the minus sign of the strain ε_c in Table 2. One can see, in Fig. 2, that Co inclusion in ZnO films with Co molar ratios x = 0.02 and x = 0.04 has no effect on lattice parameters and consequently, no effect on the directional strain. The Co inclusion takes effect from x = 0.06 where both parameters a and c vary alternatively, as a function of Co molar ratio, between 3.273 and 3.232 Å for a parameter and between 5.192 and 5.209 Å for c parameter. This significant difference between these values and those of the sample corresponding to x = 0.00 suggests, according to Yildiz et al. [40], that substitution is not the only mechanism for Co inclusion in ZnO despite the convergence between ionic radii of Zn^{2+} and Co^{2+}. Co ions may also occupy interstitial sites in hexagonal ZnO. According to Arefi-Rad and Kafachan [41], the change of the sign of the directional strain observed for x = 0.06 and x = 0.08 (Table 2) may be due to asymmetric distortions along particular crystallographic directions caused by the inclusion of the Co ions in the ZnO host lattice. For x = 0.10, both parameters a and c reach values of the sample deposited without Co inclusion (i.e. x = 0.00) indicating stress relaxation. The stress relaxation phenomenon arose simultaneously with the appearance of $Zn(OH)_2$ and Co_3O_4 secondary phases.

Table 3 regroups some crystallographic parameters determined from the preferential orientation corresponding peak such as the (002)-oriented crystallite size $D_{(002)}$, the texture coefficient $TC_{(002)}$, and the stacking fault energy SFE. $D_{(002)}$ and SFE are estimated from the (002) peak position $\theta_{(002)}$ and the broadening of the (002) diffraction line measured at half of its maximum intensity $\beta_{(002)}$ using the following relations [38,42]:

$$D_{(002)} = \frac{0.9\lambda}{\beta_{(002)}\cos\theta_{(002)}} \tag{5}$$

$$SFE = \left(\frac{2\pi^2}{45\sqrt{3\tan\theta_{(002)}}}\right)\beta_{(002)} \tag{6}$$

where λ is the wavelength of the applied X-rays. A lower value of SFE suggests that the material exhibits a higher crystalline quality of the material [41]. In good agreement with $D_{(002)}$ results in Table 3.

For more accuracy in measuring the crystallite size regarding the faced difficulty of the attribution of the XRD peak broadening to the crystallite size or to the microstrain, we have used two other methods for crystallite size calculation: the Monshi-Scherrer (M-S) method and the Williamson-Hall (W–H) method. These two methods are based on determining the crystallite size D from the diffraction angle $\theta_{(hkl)}$ and the FWHM $\beta_{(hkl)}$ of all XDR peaks. The Monshi-Scherrer method, proposed by Monshi et al. [43] in order to minimize errors in the calculation of the crystallite size, is based on the introduction of the logarithmic function in the Debye-Scherrer D-S relation [38]. The equation representing this method is given by Ref. [43]:

Table 2
Lattice parameters and directional strain determined from XRD patterns of elaborated samples.

Co molar ratio	a(Å)	c(Å)	ε_a (%)	ε_c (%)
0.00	3.251	5.204	0.06	−0.04
0.02	3.251	5.204	0.06	−0.04
0.04	3.251	5.204	0.06	−0.04
0.06	3.272	5.192	0.71	−0.27
0.08	3.232	5.209	−0.52	0.06
0.10	3.251	5.204	0.06	−0.04

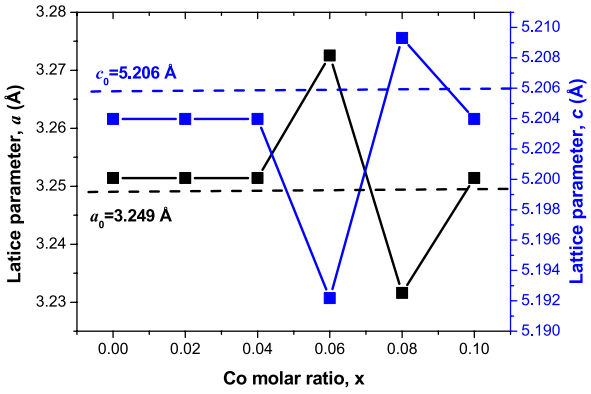

Fig. 2. Variation of lattice parameters as a function Co molar ratio.

Table 3
Crystallographic parameters determined from the (002) diffraction peak.

Co molar ratio	$2\theta_{(002)}$ [°]	$I_{(002)}$	$\beta_{(002)}$ [°]	$TC_{(002)}$	$D_{(002)}$ [nm]	SFE
0.00	34.49	3767.54	0.275	3.24	30.2	0.125
0.02	34.48	2505.85	0.290	2.93	28.7	0.132
0.04	34.48	2386.52	0.290	2.82	28.7	0.132
0.06	34.52	2100.94	0.268	2.70	31.0	0.122
0.08	34.55	1550.85	0.252	2.68	33.0	0.114
0.10	34.49	3085.42	0.223	4.25	37.2	0.101

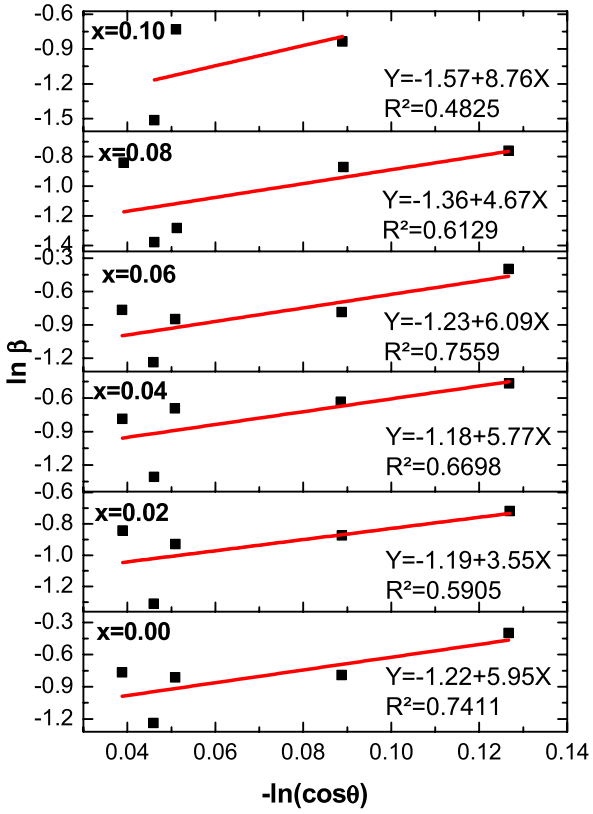

Fig. 3. Monshi-Scherrer plots for all samples (Red lines are the linear fit). (For interpretation of the references to colour in this figure legend, the reader is referred to the Web version of this article.)

$$\ln \beta_{(hkl)} = \ln \frac{0.9\lambda}{D_{M-S} \cos \theta_{(hkl)}} = \ln \frac{0.9\lambda}{D_{M-S}} - \ln\cos\theta_{(hkl)} \quad (7)$$

where λ is the wavelength of the applied X-rays and $D_{M\text{-}S}$ is the crystallite size which is determined from a linear fit of the variation of $\ln\beta_{(hkl)}$ as a function of $-\ln\cos\theta_{(hkl)}$ (Fig. 3). Resulting crystallite sizes $D_{M\text{-}S}$ calculated using the Monshi-Scherrer method for all Co molar ratios are grouped in Table 4. The Williamson-Hall method represents a simple approach that takes into consideration the contribution of the crystallite size D and the microstrain ε in the broadening of XRD peaks. The Williamson-Hall approach is given by Ref. [44]:

$$\beta_{hkl} \cos \theta_{hkl} = \frac{0.9\lambda}{D_{W-H}} + 4\varepsilon \sin \theta_{hkl} \quad (8)$$

where λ is the wavelength of the applied X-rays, ε is the microstrain, and $D_{W\text{-}H}$ is the crystallite size which is determined from a linear fit of the variation of $\beta_{(hkl)}\cos\theta_{(hkl)}$ as a function of $4\sin\theta_{(hkl)}$ (Fig. 4). Resulting crystallite sizes $D_{W\text{-}H}$ calculated for all Co molar ratios are regrouped in Table 4. We can see, in Table 4, that the obtained crystallite sizes using D-S, M-S, and W–H methods show the same trend. They decreased, for x = 0.02 and x = 0.04 and start increasing from x = 0.06 to reach their highest values for x = 0.10. We can see also that values of $D_{D\text{-}S}$ and $D_{M\text{-}S}$ are close and less than that of $D_{W\text{-}H}$ which is in good agreement with results in Refs. [41,42,45]. According to Ref. [41], $D_{W\text{-}H}$ values of Mn-doped SnS nanoparticules are comparable to the crystallite size measured using TEM and this indicates that the W–H method is more accurate compared with the other two methods due to the fact that it does not neglect the effect of microstarin.

In Fig. 5, the variation of the crystallite size $D_{W\text{-}H}$ is traced with the (002) peak intensity $I_{(002)}$ as a function of Co molar ratio. For x = 0.00, the $D_{W\text{-}H}$ value (72.2 nm) is in good agreement with those in Ref. [46]. One can see, in Fig. 5, a rapid decrease of $D_{W\text{-}H}$ for x = 0.02 (33.1 nm) accompanied by a rapid decrease of $I_{(002)}$. If we consider a correlation between an XRD peak intensity and the crystallite number, the rapid decrease of $I_{(002)}$, for x = 0.02, indicates that Co inclusion in ZnO influences the crystallites number and the crystallite size differently and this is confirmed by the other experimental points. We can also see in Fig. 5 that, from x = 0.04, $I_{(002)}$ continue decreasing while $D_{W\text{-}H}$ starts growing from 39.7 nm to reach 88.3 nm for x = 0.08. For x = 0.10, the increase of $D_{W\text{-}H}$ (158.9 nm) is accompanied by an increase of $I_{(002)}$ which reached a value less than that for x = 0.00 (Fig. 5). This increase coincides with the formation of $Zn(OH)_2$ and Co_3O_4 secondary phases. The increase of $I_{(002)}$ and $D_{(002)}$, even for x = 0.10, is accompanied with a pronounced decrease of (101) and (102) peaks intensity and a complete disappearance of (100) and (110) peaks (Fig. 1). This may be related to stress induced by the inclusion of Co ions in ZnO. This grain growth phenomenon was also found by Schoeppner et al. [47] in Au-doped ZnO. They attribute the grain growth induced by stress to grain rotation, grain boundary sliding, and diffusion according to previous studies on other materials [48–51].

3.2. Raman spectroscopy

Raman spectra of the elaborated samples, recorded in the wavenumber range 200–900 cm^{-1}, are presented in Fig. 6. According to the group theory, the zone center of optical phonons, in Wurtzite ZnO, is described by $\Gamma = A_1 + E_1 + 2E_2 + 2B_1$ where A_1 and E_1 are polar modes which can be divided to transverse optical component (A_{1T} and E_{1T}) and longitudinal optical component (A_{1L} and E_{1L}), E_2 consists of two modes corresponding to high (E_{2H}) and low (E_{2L}) phonons frequencies and B_1 is a silent mode [52]. We can see that Raman spectra shape varies as a function of Co molar ratio. For x = 0.00, the presence of four broad peaks can be seen. The first peak, located around 380 cm^{-1}, corresponds to A_{1T} vibration mode of ZnO [53], the second peak, around 450 cm^{-1} corresponds to E_{2H} vibration mode of ZnO [53] and the third peak, located around 580 cm^{-1}, corresponds E_{1L} vibration mode of ZnO [54]. The third peak, located around 780 cm^{-1}, may be related to low packing morphology as observed in porous ZnO films [55]. When x = 0.06, the peak around 780 cm^{-1} disappears simultaneously with the narrowing of the E_{2H} corresponding peak indicating an enhancement of the crystalline structure regarding the increase of the crystallites size (Fig. 5). The invariance of Raman spectra, for x < 0.06, compared with that of x = 0.00 indicates that there is no effect of Co inclusion on the ZnO crystalline structure in good agreement with results in Figs. 2 and 3. For x = 0.10, we can see the appearance of two peaks around 228 and 278 cm^{-1}. These peaks are attributed to $Zn(OH)_2$ phase [56] in excellent agreement with results in Fig. 1-a. The asymmetric of the peak around 580 cm^{-1} may be due to the presence of E_g (488 cm^{-1}) and F_{2g} (522 and 618 cm^{-1}) of Co_3O_4 [57] in addition of the E_{1L} vibration mode of ZnO.

Table 4
Crystallite size of the elaborated samples calculated using the Debye-Scherrer method $D_{D\text{-}S}$, the Monshi-Scherrer method $D_{M\text{-}S}$, and the Williamson-Hall method $D_{W\text{-}H}$.

Co molar ratio	$D_{D\text{-}S}$ [nm]	$D_{M\text{-}S}$ [nm]	$D_{W\text{-}H}$ [nm]
0.00	30.2	26.9	72.2
0.02	28.7	26	33.1
0.04	28.7	25.9	39.7
0.06	31.0	27.3	56.7
0.08	33.0	30.9	88.3
0.10	37.2	38.2	158.9

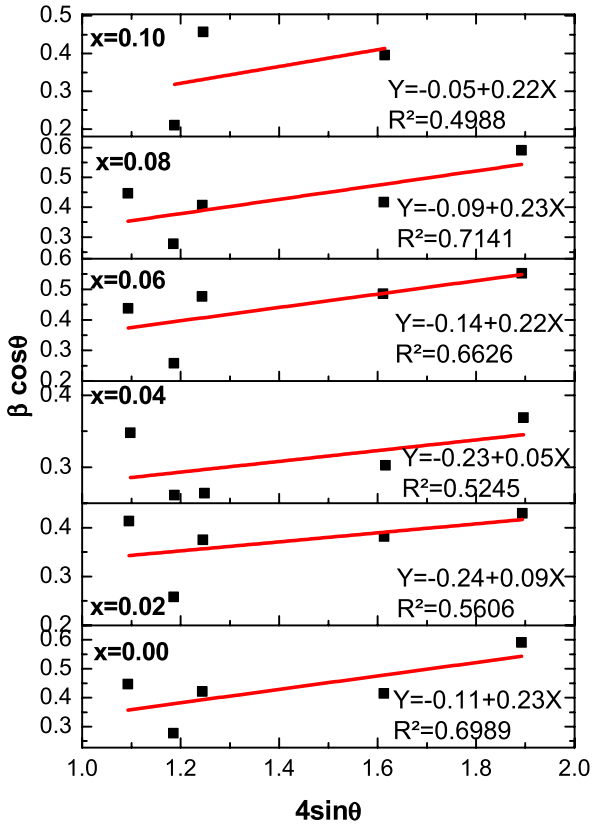

Fig. 4. Williamson-Hall plots for all samples (Red lines are the linear fit). (For interpretation of the references to colour in this figure legend, the reader is referred to the Web version of this article.)

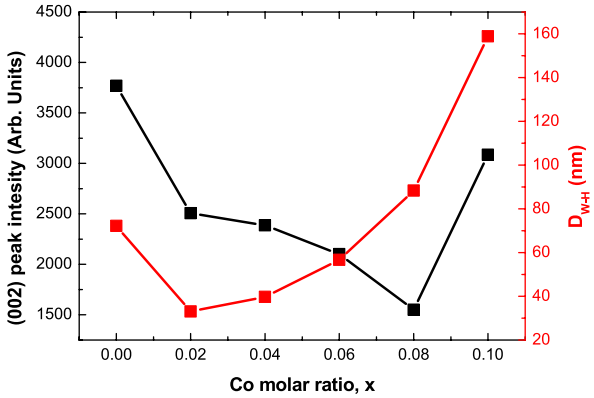

Fig. 5. Variation of the W–H crystallite size and the (002) peak intensity as a function of Co molar ratio.

3.3. ATR-FTIR spectroscopy

Fig. 7 shows ATR-FTIR spectra of the elaborated samples with different Co molar ratios. These absorption spectra were recorded in ambient air in the wavenumber range between 1300 and 550 cm^{-1}. All spectra have the same shape with quite difference in some regions. They exhibit two asymmetric peaks that may contain, according to literature, a peak around 1150 cm^{-1} attributed to C– –H [58], a peak around 1060 cm^{-1} attributed to Zn– –Zn [59], a peak around 890 cm^{-1} attributed to –OH [60], a peak around 875 cm^{-1} attributed to O–C–O [61], a peak around 760 cm^{-1} attributed to Zn– –H [54], a peak around 700 cm^{-1} attributed to Zn– –Zn [54] and a peak around 680 cm^{-1} attributed Co–O [62]. As can be seen, in Fig. 7, the intensity of these two asymmetric absorption peaks increases as a function of Co molar ratio. To study the effect of Co inclusion on these bonds, we have made a deconvolution of each spectrum into 7 Gaussians basing on the above cited bonds positions. An example of a deconvolution of an ATR-FTIR spectrum into 7

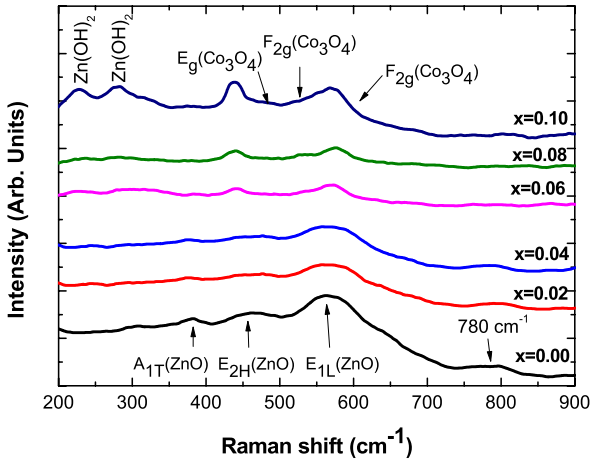

Fig. 6. Raman spectra of ZnO films as a function of Co molar ratio.

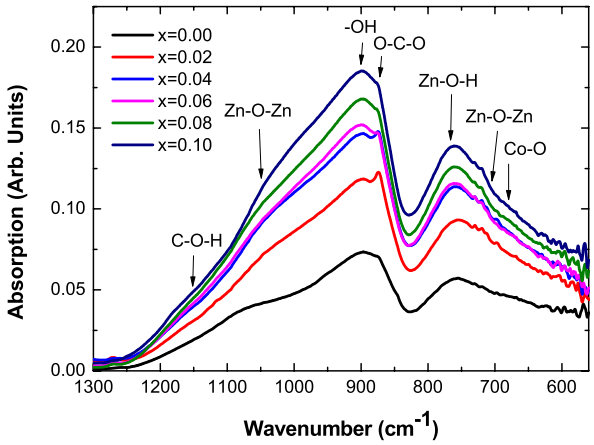

Fig. 7. ATR-FTIR spectra of ZnO films as a function of Co molar ratio.

Gaussians is shown, in Fig. 8, with a correlation coefficient $R^2 = 0.99918$.

In Fig. 9-a, is presented Gaussian peaks areas of Zn–*O*–Zn (1060 cm^{-1}), Zn–*O*–Zn (700 cm^{-1}), Zn–*O*–H and Co–O bonds as a function of Co molar ratio. Basing on the fact of the correlation between the absorption peak area and the corresponding bond density, one can

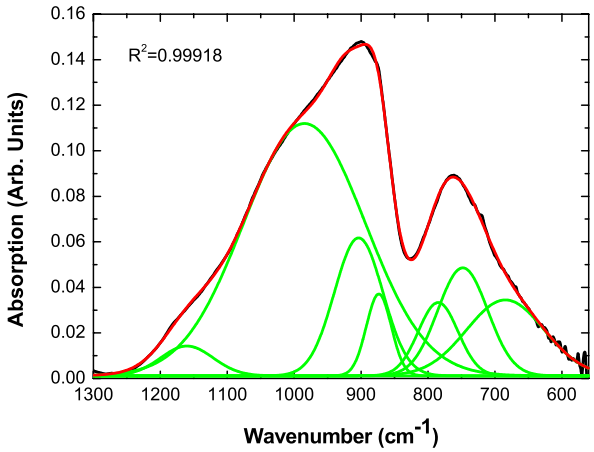

Fig. 8. Example of a deconvolution of a ATR-FTIR spectrum.

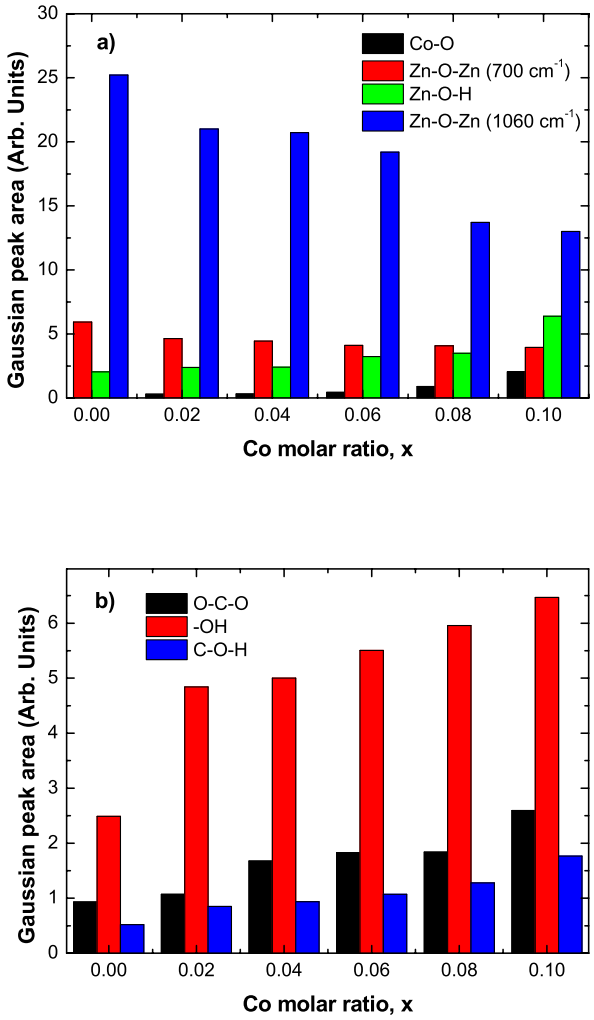

Fig. 9. Variation, as a function of Co molar ratio, of ATR-FTIR Gaussian area corresponding to a) Co–O, Zn–*O*–Zn (700 cm^{-1}), Zn–*O*–H and Zn–*O*–Zn (1060 cm^{-1}) and b) O–C–O, –OH and C–*O*–H.

evidence the degradation of deposited ZnO after Co inclusion from the decrease of both Zn–*O*–Zn bonds density as a function of Co molar ratio which is in good agreement with XRD results. This decrease is accompanied by an increase of both Zn–*O*–H and Co–O bonds density. The increase of Zn–*O*–H bond density as a function of Co molar ratio $x < 0.10$ may be due to the adsorption of water molecules on ZnO surface. For $x = 0.10$, the significant increase of Zn–*O*–H bond density may be explained by the formation of $Zn(OH)_2$ secondary phase revealed by Raman spectroscopy and XRD. We can see also the correlation between Co–O bond density and Co molar ratios $x < 0.10$ indicating a good insertion of Co in ZnO matrix. For $x = 0.10$, the rapid increase of Co–O bond density could be related to the formation of Co_3O_4 secondary phase which correlates with results of XRD. In Fig. 9-b, is presented the variation of Gaussian peak area of O–C–O, –OH and C–*O*–H bonds as a function of Co molar ratio. We can see that all bonds density increases as a function of Co molar ratio reflecting the increase of CO_2 and H_2O adsorption on ZnO surface. This indicates that Co inclusion influences also the surface adsorption of ZnO.

3.4. U –visible spectroscopy

Fig. 10 presents UV–Visible spectra, recorded in the wavelength range 300–900 nm, of the deposited films with Co molar ratios from $x = 0.00$ to $x = 0.10$,. One can see that the shape of these spectra varies with the variation of Co molar ratio. For $x = 0.02$ and $x = 0.04$, the shape of UV–Visible spectra looks the same as that for $x = 0.00$. The only difference is the decrease of the transmittance. For $x = 0.06$ and $x = 0.08$, in addition to the decrease of the optical transmittance, one can see weak absorption bands between 550 and 700 nm corresponding to the substitution of Zn ions by Co ions in hexagonal ZnO [63]. The significant decrease of the optical transmittance with the disappearance of Co corresponding absorption bands, observed for $x = 0.10$, may be interpreted by the formation of Co_3O_4 and $Zn(OH)_2$ secondary phases. The mean transmittance T_m in the visible region between 400 and 800 nm, decreases from 70.33 %, for

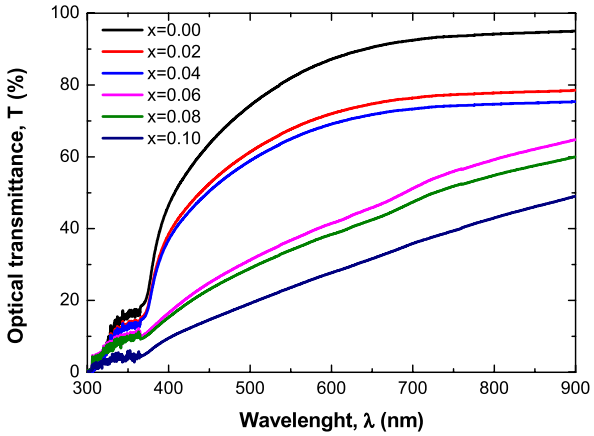

Fig. 10. UV–Visible spectra of ZnO films as a function of Co molar ratio.

x = 0.00, to reach its lowest value of 23.25 % for x = 0.10 as can be seen in Fig. 11. The decrease of the mean transmittance correlates with the increase of crystallite size observed in Fig. 5. The inclusion of Co in ZnO increased the absorption of visible light and this may be explained by the increase of the s-d and p-d exchange interactions between electrons band in ZnO and localized d electrons in Co ions [64]. This result is in good agreement with those in Refs. [25,26,65].

The variation of the band gap energy E_g is also presented in Fig. 11 as a function of Co molar ratio. The band gap energy is determined graphically from the extrapolation of the linear part of the curve $(\alpha d h\nu)^2$, as a function of photon energy $h\nu$, up to the abscissa corresponding to $(\alpha d h\nu)^2 = 0$ (Inset of Fig. 11). This curve was traced using the Tauc's law, for allowed direct transitions, given by Ref. [66] $\alpha h\upsilon = A\left(h\upsilon - E_g\right)^{1/2}$ where $\alpha = -\frac{1}{d}\ln\frac{T}{100}$ is the absorption coefficient (in cm^{-1}) expressed as a function of the thickness d and the transmittance T (in %). The band gap energy value $E_g = 3.45$ eV corresponding to x = 0.00 (Fig. 11) is greater than that of the bulk ZnO (3.37 eV) however, it is comparable to those of Giri et al. [67] and Slimani et al. [68]. The decrease of the band gap energy E_g to 2.67 eV, for x = 0.08, is in good agreement with the results in Refs. [25,26]. This decrease may be due to sp-d exchange interactions between electrons band in ZnO and localized d electrons in substituted Co ions. According to Biradjar et al. [64], the s-d and p-d exchange interactions would lead to the narrowing of the band gap and would give rise of some corrections of the conduction band and the valence band energies. The increase of the band gap energy for x = 0.10 (E_g = 2.84 eV) may be interpreted by the decrease of sp-d exchange interactions caused by the formation of Co_3O_4 and $Zn(OH)_2$ secondary phases which is in good agreement with results in Refs. [29,69].

3.5. PL spectroscopy

Fig. 12 presents PL spectra of ZnO films as a function of Co molar ratio. Except for the spectrum corresponding to x = 0.10, all spectra have the same shape with two dominant emission peaks, ultraviolet (UV) emission around 375 nm and near infrared (NIR) emission around 754 nm. The UV emission is generally related to the creation, by photo stimulation, of excitons of energies near the ZnO band edge. A slight red shift could be observed, in Fig. 12, in good agreement with UV–visible results. The decrease of this emission peak intensity may be explained by the decrease of the probability of excitons creation due to the reduce of the crystalline quality induced by the inclusion of Co in ZnO [70]. One can see, in Fig. 13, a correlation between the UV emission peak intensity and

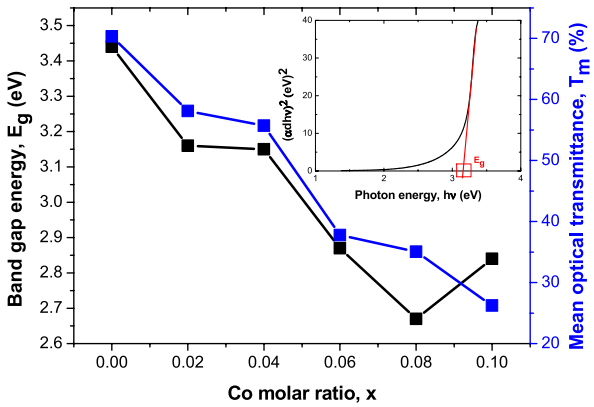

Fig. 11. Variation of the band gap energy and the mean optical transmittance as a function of Co molar ratio (**Inset:** Plot of $(\alpha d h\nu)^2$ vs. $h\nu$).

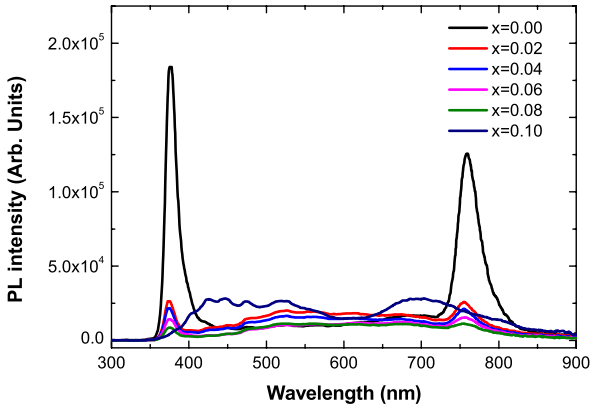

Fig. 12. PL spectra of ZnO films as a function of Co molar ratio.

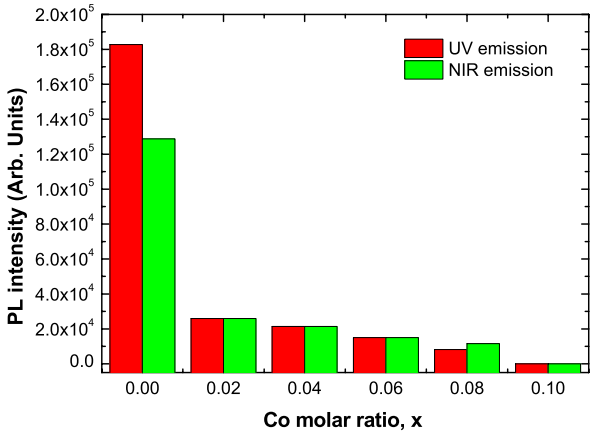

Fig. 13. Variation of UV and NIR emission intensity as a function of Co molar ratio.

Co molar ratio after a sharp decrease (for x = 0.02) indicating the efficiency of included Co ions in reducing exitons creation. The NIR emission peak was also found by Wang et al. [71] around 756 nm. They attributed this emission to the donor-acceptor transition between oxygen vacancies V_O and zinc vacancies V_{Zn} and/or the radiative recombination of trapped electrons with trapped holes in oxygen interstitial O_i [71]. The variation of the NIR emission peak intensity as a function of Co molar ratio is also presented in Fig. 13. As can be seen, the decrease of the NIR emission is directly related to the increase of included Co ions which decreases native defects in ZnO such as V_O, V_{Zn} and O_i responsible for the NIR emission by donor-acceptor transition and/or by radiative recombination of trapped electrons with trapped holes. For x = 0.10 (Fig. 12), a red emission peak appears around 697 nm simultaneously with the disappearance of both UV and NIR emissions. According to Xiao et al. [72], this emission peak is attributed to the d-d radiative transition of Co ions in a tetrahedral crystal field. The red emission evidences the inclusion of Co in ZnO which could involve Co-based impurities and deep level defects [73]. The presence of the red emission peak is accompanied with the appearance of several peaks around 400 nm correspond to zinc vacancies V_{Zn} [74], 424 and 448 nm correspond to zinc interstitial Zn_i [74,75], 478 nm correspond to oxygen vacancies with one trapped electron V_O^+ [74], 519 nm correspond to oxygen vacancies with two trapped electrons V_O [75] and 562 nm correspond to oxygen vacancies without trapped electrons V_O^{++} [75]. For x = 0.10, the significant presence of Co defects related red emission compared with ZnO defects (V_O, V_O^+, V_O^{++}, V_{Zn} and Zn_i) related emission peaks indicates the formation of Co agglomerations in excellent agreement with results of XRD (see Fig. 1).

4. Conclusion

In this work, the effect of Co inclusion on the structural and optical behavior of ZnO was studied. ZnO thin films were sprayed onto heated glass substrates by varying Co molar ratio from x = 0.00 to x = 0.10 in the precursor solution. The deposited films were characterized for their structural and optical properties by X-ray diffraction (XRD), Raman spectroscopy, ATR-FTIR spectroscopy, UV–Visible spectroscopy, and photoluminescence spectroscopy (PL). XRD patterns revealed a decrease of the crystalline quality of ZnO from Co molar ratio x = 0.06. For x = 0.10, two secondary phases Co_3O_4 and $Zn(OH)_2$ appeared suggesting that Co inclusion slowed down the formation of hexagonal ZnO phase. The presence of secondary phases was confirmed by Raman spectroscopy and ATR-FTIR

spectroscopy. This last evidenced the enhancement of ZnO surface adsorption of CO_2 and H_2O induced by Co inclusion. According to UV–Visible spectroscopy, as a function of Co molar ratio, the mean transmittance in the visible region decreased from 70.33 % to 23.25 % and the band gap energy E_g decreased from 3.45 eV to reach its lowest value 2.67 eV for x = 0.08. The increase of the band gap energy for x = 0.10 (2.84 eV) may be interpreted by the decrease of sp-d exchange interactions caused by the formation of Co_3O_4 and $Zn(OH)_2$ secondary phases. All PL spectra, except for that corresponding to x = 0.10, exhibited an UV emission peak around 375 nm and a NIR emission peak around 754 nm. The intensity of these two emission peaks decreased as a function of Co molar ratio. The complete disappearing of these two emissions, for x = 0.10, was accompanied with the appearance of a red emission around 697 nm, attributed to Co-based impurities, and other peaks attributed to deep level defects in ZnO. All these effects make the elaborated Co-doped ZnO candidate for use in other domains, in addition to the spintronics one, such as gas sensing, light emitting diodes (LED), and solar cells.

CRediT authorship contribution statement

R. Nettour: Writing – review & editing, Writing – original draft, Methodology, Investigation. **A. Kabir:** Writing – original draft, Methodology, Investigation. **A. Erdoğmuş:** Investigation. **Ö.D. Kutlu:** Writing – review & editing, Investigation, Conceptualization. **G. Schmerber:** Investigation.

Declaration of competing interest

The authors declare that they have no known competing financial interests or personal relationships that could have appeared to influence the work reported in this paper.

Acknowledgment

Authors thank Miss Nora Abdennouri from the department of chemistry (Faculty of Science-University of Skikda-Algeria) for her help during the solutions preparation. Special thanks, from authors to one of them, Dr. G. Schmerber from IPCMS in Strasbourg-France, for Raman and PL measurements and results analysis.

Data availability

Data will be made available on request.

References

[1] E.F. Keskenler, G. Turgut, S. Doğan, Superlattice. Microst. 52 (2012) 107.
[2] B. Kumar, S.-W. Kim, Nano Energy 1 (2012) 342.
[3] M. Baneto, A. Enesca, Y. Lare, K. Jondo, K. Napo, A. Duta, Ceram. Int. 40 (2014) 8397.
[4] D. Gao, Z. Zhang, J. Fu, Y. Xu, J. Qi, D. Xue, J. Appl. Phys. 105 (2009) 113928.
[5] D. Li, W. Liu, J. Zong, J. Wei, G. Tan, Q. Yuan, A. Xia, D. Liu, Ceram. Int. 50 (2024) 39391.
[6] D. Domyati, Mater. Sci.: Mater. Electron. 35 (2024) 406. https://www.sciencedirect.com/journal/sensors-and-actuators-a-physical/vol/335/suppl/C.
[7] F.M. Davoodi, S.M. Rozati, S. Soltani, Appl. Phys. A 130 (2024) 866.
[8] H. Abdullah, K.J. Xian, K.C. Ying, et al., Sol. Energy 60 (2024) 461.
[9] A. Abutaleb, S. Ahmed, M. Imran, Eur. Phys. J. Plus 138 (2023) 1046.
[10] I. Naeem, F. Baig, M.H. Fahad, et al., Ionics 30 (2024) 2989.
[11] H. Musleh, H. Zayed, S. Shaat, H.M. Tamous, J. Asad, A. Al-Kahlout, A. Issa, N. Shurrab, N. AlDahoudi, J. Phys.: Conf. Ser. 1294 (2019) 022022.
[12] R. Hong, L. Xu, H. Wen, J. Chen, J. Liao, W. You, Opt. Mater. 34 (2012) 786.
[13] Q.P. Wang, D.H. Zhang, Z.Y. Xue, X.J. Zhang, Opt. Mater. 26 (2004) 23.
[14] A.R. Pawar, K.R. Shaikh, A.D. Salmote, et al., J. Mater. Sci. Mater. Electron. 34 (2023) 2271.
[15] W. Chen, Y.H. Lu, M. Wang, L. Kroner, H.J. Fecht, J. Phys. Chem. C 113 (2009) 1320.
[16] P.Y. Wang, Q.H. Gao, J.Q. Xu, Fine Chem. 24 (2007) 436.
[17] H. Saadi, O. Khaldi, A. Dahri, N. Abdelmoula, I. Hammami, M.P. Fernandes Graça, Z. Benzarti, Ceram. Int. 50 (2024) 44151.
[18] C.S. Barret, T.B. Massalski, Structure of Metals, Pergamon Press, Oxford, 1980.
[19] E. Rincon-Suarez, J.M. Mozo, A. Romero-López, S. Alcántara-Iniesta, Francisco J. Flores-Ruiz, L.E. Serrano, Mater. Sci. Eng. B 320 (2025) 118430.
[20] O. Dimitrov, D. Nesheva, V. Blaskov, I. Stambolova, S. Vassilev, Z. Levi, V. Tonchev, Mater. Chem. Phys. 148 (2014) 712.
[21] H. Saadi, O. Khaldi, J. Pina, T. Costa, J.S.S. de Melo, P. Vilarinho, Z. Benzarti, Nanomaterials 14 (2024) 122.
[22] M. Raja, N. Muthukumarasamy, D. Velauthapillai, R. Balasundrapraphu, T.S. Senthil, S. Agila, Superlattice. Microst. 80 (2015) 53.
[23] X. Mo, Z. Li, C. Liu, X. Tao, Y. Zhou, H. Long, H. Wang, Y. Ouyang, J. Lumin. 213 (2019) 127.
[24] M.A. Mahmood, K. Althubeiti, S.S. Abdullaev, et al., J. Mater. Sci. Mater. Electron. 34 (2023) 1784.
[25] F. Pan, C. Song, X.J. Liu, Y.C. Yang, F. Zeng, Mater. Sci. Eng. R 62 (2008) 1.
[26] T. Dietl, H. Ohno, F. Matsukura, J. Cibert, D. Ferrand, Science 287 (2000) 1019.
[27] K. Sato, H. Katayama-Yoshida, Jpn. J. Appl. Phys. 39 (2000) L555.
[28] C. Rath, P. Mallick, D. Pandey, D. Sa, A. Banerjee, N.C. Mishra, J. Phys. Condens. Matter 21 (2009) 075801.
[29] H. Ji, C. Cai, S. Zhou, W. Liu, J. Mater. Sci. Mater. Electron. 29 (2018) 12917.
[30] A. Mahroug, S. Boudjadar, S. Hamrit, L. Guerbous, J. Mater. Sci. Mater. Electron. DOI 10.1007/s10854-014-2259-6.
[31] D. Akcan, Mater. Res. Bull. 139 (2021) 111254.
[32] American Society for Testing and Material, Powder Diffraction Files; Joint Committee on Powder Diffraction Standards, 1999, pp. 3–888. Swarthmore, PA.
[33] T.P. Rao, M.C. Santhoshkumar, Appl. Surf. Sci. 255 (2009) 7212.
[34] M. Ivill, S.J. Pearton, S. Rawal, L. Leu, P. Sadik, R. Das, A.F. Hebard, M. Chisholm, J.D. Budai, D.P. Norton, J. New, Physics 10 (2008) 065002.
[35] A. Sundararaj, G. Chandrasekaran, Nano-Struct. Nano-Objects 11 (2017) 20.

[36] R. Bagheri, H. Kafashan, Ceram. Int. 50 (2024) 37041.
[37] P. Gu, X. Zhu, D. Yang, RSC Adv. 9 (2019) 8039.
[38] M. Saleem, L. Fang, H.B. Ruan, F. Wu, Q.L. Huang, C.L. Xu, C.Y. Kong, Int. J. Phys. Sci. 7 (23) (2012) 2971.
[39] J.F. Chang, C.C. Shen, M.H. Hon, Ceram. Int. 29 (2003) 245.
[40] A. Yildiz, B. Yurduguzel, B. Kayhan, G. Calin, M. Dobromir, F. Iacom, J. Mater. Sci. Mater. Electron. 23 (2012) 425.
[41] M.R. Arefi-Rad, H. Kafashan, Ceram. Internat. 50 (2024) 31826.
[42] R. Bagheri, H. Kafashan, Phys. B 688 (2024) 416156.
[43] A. Monshi, M.R. Foroughi, M.R. Monshi, J. World, Nano Sci. Eng. 2 (2012) 154.
[44] G.K. Williamson, W.H. Hall, Acta Metall. (1953) 22.
[45] H. Kafashan, Z. Orshesh, A. Bahrami, F. Zakerian, Phys. B 675 (2024) 415623.
[46] S. Mustapha, M.M. Ndamitso, A.S. Abdulkareem, J.O. Tijani, D.T. Shuaib, A.K. Mohammed, A. Sumaila, Adv. Nat. Sci. Nanosci. Nanotechnol. 10 (2019) 045013.
[47] R.L. Schoeppner, R.S. Goeke, N.R. Moody, D.F. Bahrd, Acta Mater. 91 (2015) 1.
[48] T. Bannuru, W.L. Brown, S. Narksitipan, R.P. Vinci, J. Appl. Phys. 103 (2008) 083522.
[49] N. Fuschillo, M.L. Gimpl, J. Mater. Sci. 5 (1970) 1078.
[50] A.J. Haslam, D. Moldovan, V. Yamakov, D. Wolf, S.R. Phillpot, H. Gleiter, Acta Mater. 51 (2003) 2097.
[51] F. Sansoz, V. Dupont, Appl. Phys. Lett. 89 (2006) 111901.
[52] J.M. Calleja, M. Cardona, Phys. Rev. B 16 (1977) 3753.
[53] J. Zuo, C. Xu, Y. Liu, Y. Qian, Nanostruct. Mater. 10 (1998) 1331.
[54] R. Zhang, G.P. Yin, N. Wang, L. Guo, Solid State Sci. 11 (2009) 865.
[55] A. Barranco, A. Borras, A. Gonzalez-Elipe, A. Palmero, Prog. Mater. Sci. 76 (2016) 59.
[56] M. Wang, L. Jiang, E.J. Kim, S.H. Hahn, RSC Adv. 5 (2015) 87496.
[57] V.G. Hadjiev, M.N. Iliev, I.V. Vergilov, J. Phys. C Solid State Phys. 21 (1988) L199.
[58] U.R. Gudla, B. Suryanarayana, V. Raghavendra, K.A. Emmanuel, N. Murali, P. Taddesse, D. Parajuli, K.C.B. Naidu, Y. Ramakrishna, K. Chandramouli, Results Phys. 19 (2020) 103508.
[59] I. Matai, A. Sachdev, P. Dubey, S.U. Kumar, B. Bhushan, P. Gopinath, J. Colloids Surf. B 115 (2014) 359.
[60] D.D. Thongam, J. Gupta, N.K. Sahu, D. Bahadur, J. Mater. Sci. 53 (2018) 1110.
[61] A. Jafari, M. Ghane, S. Arastoo, African J. Microbio, Res. 5 (2011) 5465.
[62] P. Nkeng, J.F. Koening, J.L. Gautier, P. Chartier, G.J. Poillerat, Electroanal. Chem. 402 (1996) 81.
[63] H.A. Weakliem, J. Chem. Phys. 36 (1962) 2117.
[64] S.D. Birajdar, P.P. Khirade, V.R. Bhagwat, A.V. Humbe, K.M. Jadhav, J. Alloys Compd. 683 (2016) 513.
[65] T.M. Hammad, J.K. Salem, R.G. Harrison, Appl. Nanosci. 3 (2013) 133.
[66] B.P. Kafle, S. Acharya, S. Thapa, S. Poudel, Ceram. Int. 42 (2016) 1133.
[67] P.K. Giri, S. Bhattacharyya, D.K. Singh, R. Kesavamoorthy, B.K. Panigrahi, G.M. Nair, J. Appl. Phys. 102 (2007) 093515.
[68] Y. Slimani, S. Caliskan, F.A. Khan, A. Baykal, Nano-struct, Nano-Objects 40 (2024) 101348.
[69] V.V. Petrov, V.V. Sysoev, I.O. Ignatieva, I.A. Gulyaeva, M.G. Volkova, A.P. Ivanishcheva, S.A. Khubezhov, Y.N. Varzarev, E.M. Bayan, Sensors 23 (2023) 5617.
[70] L. Xu, W. Kuang, Z. Liu, F. Xian, Physica B: Cond. Matt. 583 (2020) 412010.
[71] M. Wang, Y. Zhou, Y. Zhang, E.J. Kim, S.H. Hahn, S.G. Seong, Appl. Phys. Lett. 100 (2012) 101906.
[72] Z.Y. Xiao, H. Matsui, K. Katayama, K. Miyajima, T. Itoh, H. Tabata, J. Appl. Phys. 108 (2010) 013502.
[73] J. Xu, S. Shi, L. Li, X. Zhang, Y. Wang, Q. Shi, S. Li, H. Wang, J. Electr. Mater. 42 (2013) 12.
[74] H. Cheng, K. Lin, H. Hsu, W. Hsieh, Appl. Phys. Lett. 88 (2006) 261909.
[75] P.A. Rodnyia, K.A. Chernenkoa, I.D. Venevtseva, Optics and Spectr, vol 125, 2018, p. 372.